VIBRATIONAL ENERGY FLOW IN SUBSTITUTED BENZENES

BY

BRANDT C. PEIN

DISSERTATION

Submitted in partial fulfillment of the requirements
for the degree of Doctor of Philosophy in Chemistry
in the Graduate College of the
University of Illinois at Urbana-Champaign, 2014

Urbana, Illinois

Doctoral Committee:

Professor Dana Dlott, Chair
Professor Martin Gruebele
Professor Benjamin McCall
Professor Kenneth Suslick

Abstract

Using ultrafast infrared (IR) Raman spectroscopy, vibrational energy flow was monitored in several liquid-state substituted benzenes at ambient temperature. In a series of mono-halogenated benzenes, X-C_6H_5 (X = F, Cl, Br, I), a similar CH-stretch at 3068 cm^{-1} was excited using picosecond IR pulses and the resulting vibrational relaxation and overall vibrational cooling processes were monitored with anti-Stokes spectroscopy. In the molecules with a heavier halide substituent the CH-stretch decayed slower while midrange vibrations decayed faster. This result was logical if the density of states (DOS) in the first few tiers, which is the DOS composed of vibrations with smaller quantum number, is what primarily determines energy flow. For tiers 1-4, the DOS was nearly identical in the CH-stretch region while it increased in the midrange region for heavier halide mass.

Excitation spectroscopy, an extension of 3D IR-Raman spectroscopy, was developed and used to selectively pump vibrations localized to the substituent or the phenyl group in nitrobenzene (NB), o-fluoronitrobenzene (OFNB) and o-nitrotoluene (ONT) and in the alkylbenzene series toluene, isopropylbenzene (IPB), and *t*-butylbenzene (TBB). Using quantum chemical calculations, each Raman active vibration was sorted, according to their atomic displacements, into three classifications: substituent, phenyl, or global. Using IR pump wavenumbers that initially excited substituent or phenyl vibrations, IR-Raman spectroscopy was used to monitor energy flowing from the substituent to phenyl vibrations and vice versa.

In NB nitro-to-phenyl and nitro-to-global energy flow was almost nonexistent while phenyl-to-nitro and phenyl-to-global was weak. When ortho substituents (-CH_3, -F) were introduced, energy flow from nitro-to-phenyl and nitro-to-global was activated. In ONT, phenyl-to-nitro energy flow ceased possibly due to the added methyl group diverting energy from entering the nitro vibrations. Energy flow is therefore unidirectional in the phenyl-to-nitro direction in NB while in ONT it is unidirectional in the nitro-to-phenyl direction.

In the alkylbenzenes phenyl-to-substituent energy flow was about the same in each while substituent-to-phenyl energy was accelerated for larger alkyl substituents. If the DOS controls energy flow this is opposite of what would be expected and gives a possible route to control energy flow from an attached alkyl substituent to a phenyl group.

Acknowledgments

To my advisor Dana Dlott: I would like thank you for asking me to join your research group. Your guidance and confidence in me as a scientist were more than I could have asked for. To my fellow Dlott group members: Thank you so much for all the great memories. Working alongside each of you was a pleasure and privilege. Wherever our careers and aspirations may take us, I hope to see all of you again one day. I will always remember the Friday-Night Magic drafts with Bruno, the scientific musings with Will, the constant, yet enjoyable, debating with Yuxiao and the hilarious news article discussions with James. To my fellow spectroscopist Chris Berg: Our conversations about lasers and thought experiments were always a highlight of my day. Hopefully we will get to play another round of pool together. To the rest of the 2nd floor: Whether it was to borrow a tool, discuss some ideas or have idle conversation, thank you. The fellowship and community we had is something I will never forget. To my brother Rian: Thank you for all the late night gaming sessions that kept me sane over the years. You have always come through for me in more ways than anyone will ever know. More than anybody, I would like to thank my parents Chris and Deborah. Without your love, sacrifice and encouragement I would certainly not have the opportunities that I have today.

For My Mother, Father and Brother

Table of Contents

List of Figures

List of Tables

Chapter 1: Introduction

1.1 Substituted Benzenes

In this work, infrared (IR) Raman spectroscopy is used to measure vibrational energy flow in liquid-phase substituted benzenes at ambient temperature. First a series of mono-halogenated benzenes will be compared to demonstrate how the size, electronegativity and mass of a halogen substituent can tune energy flow in a phenyl ring. A collection of nitro-substituted benzenes which will include: nitrobenzene, o-fluoronitrobenzene and o-nitrotoluene, will also be investigated. Experiments will monitor energy flow between the nitro substituent and phenyl group and show how an additional ortho-substituent can dramatically alter this process. Finally, a collection of alkylbenzenes with increasingly larger alkyl substituents will be investigated which will include: toluene, isopropylbenzene and tert-butylbenzene. Similar to the nitro-substituted benzene experiments, energy will be monitored traversing between the alkyl substituent and phenyl group. These experiments will show how alkyl-phenyl interactions and interactions within an alkyl substituent can affect this process.

The dynamics of vibrational energy flow have relevant consequences to a variety of research topics such as reaction rate theories,[1] phononics,[2-4] shock initiation of energetic materials[5-7] and molecular electronics.[8-10] To engineer molecular-scale devices like current-carrying molecular wires[8-10] or thermal diodes,[2] understanding vibrational energy flow to the level of being able to control its characteristics,[11] similar to the way heat flow is managed in macro-scale machinery, is a desirable capability. It is envisioned that a “molecular toolbox” for building such devices could be developed where energy flow in the separate building blocks and in combinations of the pieces would be well characterized. This work represents the initial steps towards making such a “toolbox”.

Throughout this work, energy flow will often be discussed in the context of vibrational relaxation (VR). Here VR describes specific processes where energy in an initially excited, or nonthermal, vibration of a molecule flows to other vibrations within the molecule, or the surrounding bath. Intramolecular VR (IVR) processes dissipate little to no energy to the bath. Eventually several VR steps bring the molecule to a thermalized, or thermally equilibrated, state with the bath at an elevated temperature, a process known as vibrational cooling (VC).

Substituted benzenes are an excellent artifice for such studies because the phenyl vibrational spectra and dynamics aren't strongly affected by substitution. Additionally, the VR and VC processes of benzene have been studied in great detail by the Dlott laboratory[12,13] and others.[14-16] By comparing energy flow in benzene with substituted benzenes, the effects of structural perturbations, particularly substitution, to phenyl groups can be explored.[11,17-19] Phenyl groups can be considered a fundamental building block in molecular-scale devices, especially in molecular electronics. In current-carrying molecular wires, which often contain phenyl groups, nonthermal vibrational excitations can occur and poor energy dissipation can be a detriment to the functioning of the wire.[8,20] The understanding of energetic materials can also benefit from such an artifice. Useful examples like trinitrotoluene (TNT) or dinitroanisole (DNAN) are composed of a phenyl ring with attached peripheral nitro groups. How energy flows in molecules with a nitro-phenyl structure has important implications to the behavior of energetic materials where, upon shock initiation, highly nonthermal energy distributions in the nitro-group vibrations can occur.[21,22]

1.2 Experimental Technique

All of the experiments in this work will utilize the IR-Raman technique, as well as novel extensions of it, to study energy flow. A complete overview will be discussed in Chapter 3.

Briefly, the IR-Raman technique uses 1ps IR pulses to pump a vibration and delayed 1ps 532 nm pulses to probe the time evolution of all the Raman active vibrations. An example IR-Raman spectrum of toluene is found in Figure 1.1 which shows a waterfall of anti-Stokes intensity changes (relative to the ambient temperature values) at each pump-probe delay when pumping the methyl CH-stretch at 2940 cm^{-1}.

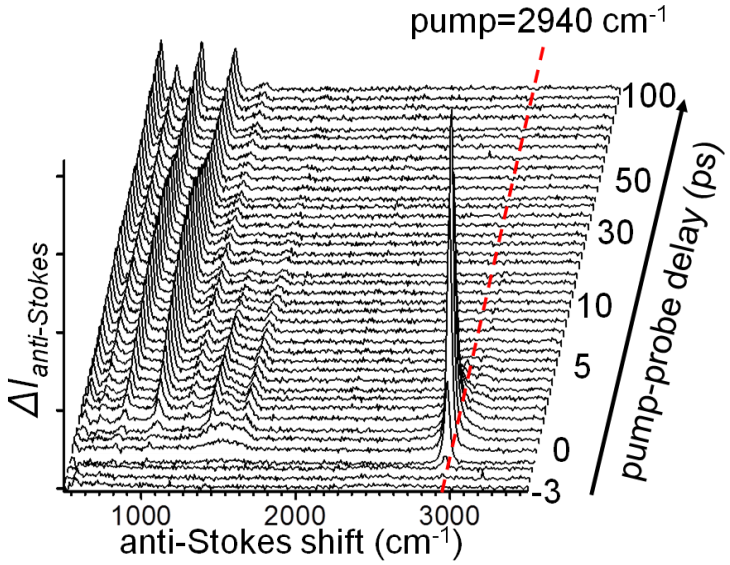

Figure 1.1. Example IR-Raman spectrum of toluene. The IR pump, indicated by the dashed line, is tuned to 2940 cm^{-1} to excite a methyl CH-stretch parent. As the parent methyl CH-stretch decays the daughter vibrations excited by the parent rise as shown on the left (<2000 cm^{-1}). The anti-Stokes signals of each vibration are proportional to their excited state populations. Note the delay axis (right).

The signal of the pumped vibration, the parent, is shown rising and decaying on the right side of the waterfall. As the parent decays, vibrations excited by the parent, the daughters, through individual VR processes are shown rising on the left side of the waterfall. The intensities of the anti-Stokes signals are proportional to the population, or occupation number, of each vibration which are used to track their time-dependent energy content.

The power of the IR-Raman technique is its capability to simultaneously monitor multiple Raman-active vibrations as energy flows from a parent vibration to the daughters and the bath.[23] Unfortunately, the small cross-sections associated with Raman scattering is a primary

weakness of these experiments. Because of this, intensity changes in weak scattering signals must be distinguished from a variety of background signals that can interfere with the Raman spectrum.[24-26]

The IR-Raman technique is by no means new. From 1974-1978 Laubereau and coworkers[27,28] developed a way to generate intense picosecond IR laser pulses that could excite CH- and OH-stretches in molecules. Using this new laser technology they were able to monitor the time-dependent VR and VC processes in ethanol and chloroform which represented the first IR-Raman experiments. In the present day the IR-Raman technique has vastly improved with the development chirped-pulse amplified Ti:sapphire lasers. This amplification technique generates millijoule sub-picosecond laser pulses that, when combined with optical parametric amplification, can be used to generate frequency tunable IR and visible pulses. This is particularly useful for newer techniques that will be used in this work such as 3D IR-Raman and excitation spectroscopy which require a wide and continuous range of IR frequencies to pump several different types of vibrations.[11,17,19,29]

It should be mentioned that there is a wealth of different techniques for measuring energy flow that have developed over the past few decades. Presently, owing to the inherently larger IR cross-sections in condensed phase molecules, the most common methods are IR-IR pump-probe techniques. A few of these include one-[30,31] and two-[32,33] color transient absorption and coherent multidimensional techniques such as two-dimensional IR (2DIR)[34] and relaxation assisted 2DIR (RA-2DIR)[35] spectroscopy.

1.3 Conceptualizing Energy Flow

The effects of substitution on energy flow in phenyl groups will be conceptualized using two approaches that are associated with either chemical physics or materials chemistry. The

chemical physics approach focuses on energy flow between specific vibrational states which, for polyatomic molecules, can become complex[36] due to the sensitivity to the details of the vibrational potential energy surface (PES).[37,38] Structural effects on energy flow are elucidated by comparing how several vibrational states in different molecules exchange energy. For example, in previous IR-Raman studies on benzene and perdeuterobenzene, the individual vibrational states were monitored after a CH- or CD-stretch was pumped.[12,13] Using a three-stage model that describes energy flow in condensed phase molecules, the Dlott laboratory compared the VR processes of corresponding phenyl vibrations in both molecules. In this way the consequences of deuteration to the details of energy flow, such as which vibrations were involved and the rates and efficiencies of energy transfer, were clearly defined. In Chapter 4, energy flow in a series of mono-halogenated benzenes, or aryl-halides, (C_6H_5-X where X=F, Cl, Br, I) will be studied using the chemical physics approach. In these experiments a CH-stretch that is similar in each of the molecules will be pumped and the resulting VR and VC processes will be compared.

For benzenes with simple monoatomic substituents the vibrational spectra are not changed to any large extent so the dynamics of multiple corresponding vibrations are easily compared. However, when polyatomic substituents are introduced, the spectrum can become cluttered. For example, a methyl (X = CH_3) subsituent in toluene introduces a new set of CH-stretches and bends that are mixed amongst the phenyl vibrations making comparisons of the individual phenyl vibrations more difficult. Additionally, it is hard to think of how to directly compare vibrations, such as nitro NO- and methyl CH-stretches, in molecules like nitrobenzene (X = NO_2) and toluene. For these situations, a spatial description rather than a state-to-state description of energy flow proves far more tractable.

One weakness of the chemical physics approach is that it does a rather clumsy job describing the spatial nature of energy flow in molecules. Here spatial refers to specific locations in the molecules such as the phenyl or substituent. From the perspective of a "molecular toolbox" this description would be more intuitive, especially for engineering devices that can control where energy goes. Treating energy flow as moving from location to location naturally falls out of the materials chemistry approach which views it as a nanoscale thermal conduction process.[39] In this approach, energy is pumped initially into vibrations localized to the substituent or phenyl group then tracked as it conducts to the phenyl or substituent respectively. Chapters 7-9 will apply this to the nitro-substituted benzenes: nitrobenzene, o-fluoronitrobenzene and o-nitrotoluene and the alkylbenzenes: toluene, isopropylbenzene and tert-butylbenzene. To do this, the molecular vibrations will be classified according to the atomic displacement of their computed normal mode vectors.[11,17,19] As shown in Figure 1.2 for the case of nitrobenzene, modes with displacement primarily on the substituent or the phenyl ring are classified as (a) substituent or (b) phenyl respectively while modes with appreciable displacement on both are classified as (c) global.

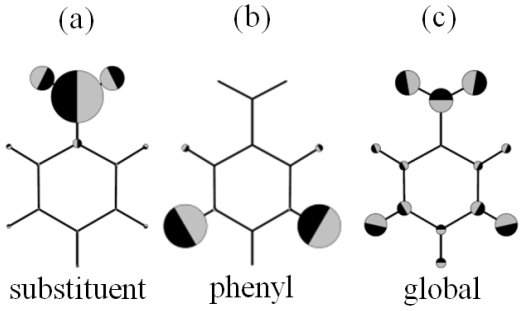

Figure 1.2. Illustrated examples of mode classes. (a) substituent (b) phenyl and (c) global modes of nitrobenzene. The spheres indicate the magnitude of the individual atomic displacements. The colors indicate the direction of the displacement.

The materials science approach monitors the time-dependent aggregate energy content in these classes of modes which reduces the analysis of energy flow to a point to point spatial dimension.

An initial drawback is that this requires a method to initially localize energy. IR spectra of substituted benzenes can be rather complicated where several vibrations overlap so attempting to pump a specific vibration is impractical if not impossible. Rather, a novel technique based off of 3D IR-Raman spectroscopy[29] was developed for this work, known as excitation spectroscopy.[17]

In 3D IR-Raman spectroscopy the dimensions are pump-probe delay, pump wavenumber and probe wavenumber. A 3D IR-Raman spectrum is composed of several normal IR-Raman spectra, like Figure 1.1, each using a different pump wavenumber. In this way they form a time-series of 2D surfaces where the two dimensions are pump wavenumber and probe wavenumber. The individual 2D IR-Raman surfaces show which vibrations are excited using a specific pump wavenumber, amongst a continuous range of pump wavenumbers, at a given pump-probe delay time. Up till recently, the technology had not been developed to the point of making the laborious measurements that the 3D IR-Raman technique required. Chapter 5 will discuss the development of a new computer-controlled apparatus that acquires 3D IR-Raman spectra and provide a detailed overview of this technique as well as excitation spectroscopy. In Chapter 6, the 3D IR-Raman technique will be used to monitor energy flow in nitromethane and acetonitrile, two liquids previously studied by the Dlott laboratory,[40,41] to demonstrate the capabilities of this new apparatus.

To selectively excite the phenyl or substituent vibrations, excitation spectroscopy monitors the distribution of vibrational energy at earlier pump-probe delay times using a continuous range of IR-pump wavenumbers. An example spectrum is shown below in Figure 1.3. This excitation spectrum is the 2D surface at the 1 ps delay of the total 3D IR-Raman spectrum of nitrobenzene. It shows the anti-Stokes intensity changes (top) 1 ps after the pump pulses arrive. The anti-Stokes signals indicate which vibrations are in the excited state. The Stokes

spectrum (bottom) is shown as a reference for the vibrational assignments. The shaded region (right) indicates the range the pump pulses where tuned and shows a diagonal of signals. The diagonal is composed of contributions from both pumped parent populations and a nonlinear scattering artifact.[42] The daughters excited by the parent are indicated by the signals on the left. Classifying the daughters and computing their energy content shows which pump-frequencies initially generate primarily phenyl or substituent excitations. By acquiring IR-Raman spectra using the pump wavenumbers found with an excitation spectrum such as this, energy can then be monitored flowing from the subsituent to the phenyl ends of the molecule, or vice versa.

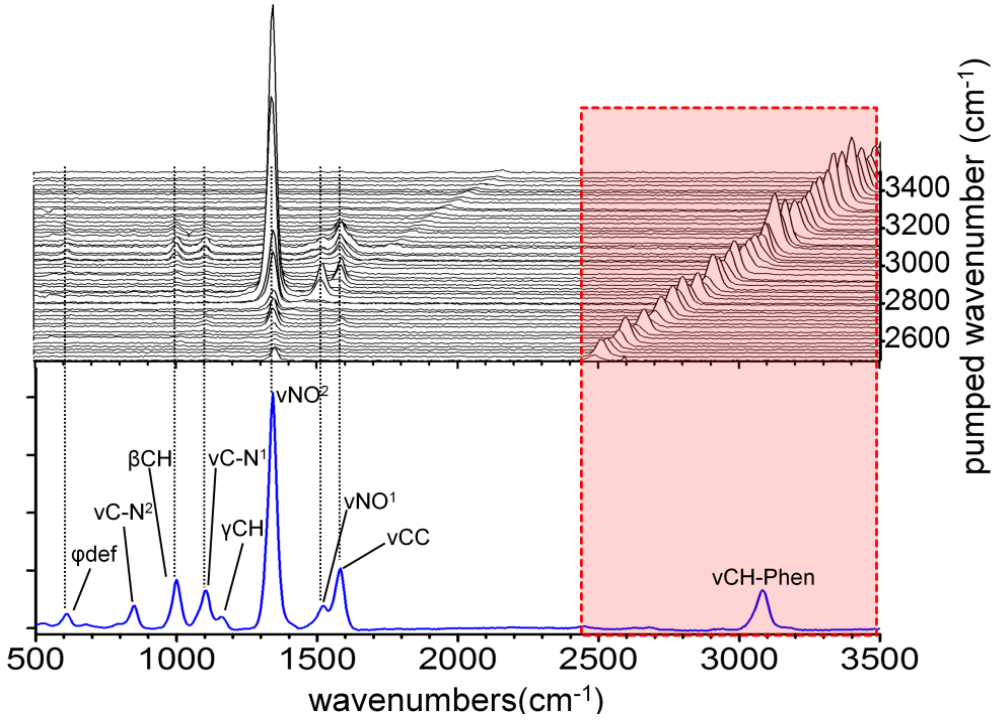

Figure 1.3. Example excitation spectrum of nitrobenzene. The IR pump pulses were scanned from 2500 to 3500 cm^{-1} while the anti-Stokes Raman spectrum (top) was monitored at 1 ps delay. The anti-Stokes intensities are proportional to the instantaneous vibrational population change $\Delta n(t)$, except on the diagonal (shaded region) where there are artifacts from nonlinear light scattering (NLS).

1.4 Substituents and Their Predicted Effects on Energy Flow

A few general types of substituents investigated in these experiments and some predictions of their effects on energy flow should be discussed. Typically VR processes have been analyzed in the context of Fermi's golden rule[36,37,43] which expresses the rate of energy transfer, k_{GR}, from an initially excited state, or bright state, as the following relation.

$$k_{GR} = \frac{2\pi}{\hbar}\rho(E)|V_{rms}|^2 \qquad (1.1)$$

Here, along with a mean anharmonic coupling matrix element V_{rms} which is roughly distilled from the vibrational PES, the total vibrational density of states (DOS) $\rho(E)$ drives the relaxation rate. In this picture, energy flows from a bright state to states that are isoenergetic with it. A weakness of the golden rule is its assumption that $\rho(E)$ is a continuous function that doesn't vary much near the bright state. Additionally it assumes that the matrix elements coupling the bright state to the states nearby in energy are small and invariant. In other words it does not take into account the possibility that a subset of states in $\rho(E)$ can be coupled to the bright state far stronger or weaker than V_{rms} indicates. If these assumptions are indeed valid, however, for the molecules studied here, some predictions can still be made.

There are several structures one could imagine attaching to a phenyl group. The simplest type would be the replacement of a hydrogen with a heavier substituent. Presumably any substituted benzene would capture this effect. However, benzenes with mono-atomic substituents would be preferential to investigate since these would make discerning solely mass-correlated effects on energy flow easier. The series of aryl-halides, discussed earlier, are perfect for this. Besides effects caused by the different size and electronegativity of the added halogen atom as well as the molecular symmetry lowering which can relax anharmonic coupling selection rules,[44] red-shifting of benzene vibrations that now involve the displacement of the heavier substituent

would occur.[18] One could imagine that an increase in the number of lower frequency modes would correspondingly increase the DOS. From the standpoint of the golden rule, this means that attaching a larger mass to a phenyl group should generally accelerate VR of excited vibrations. Being able to expedite the VR and VC dynamics in phenyl groups in this way would be a useful facet of a "molecular toolbox".

Another type of substitution would be the replacement of a hydrogen atom with a polyatomic substituent. The collection of nitrobenzenes and alkylbenzenes discussed earlier are suitable candidates for this type. The moieties in these molecules will inherently increase the DOS by virtue of their larger mass compared to hydrogen. Additionally, the increased number of atoms, correlating to more vibrations, should also augment the DOS. In the case of the alkylbenzenes, this means that increasingly larger polyatomic substituents should force energy to flow faster from initially excited subsituent or phenyl vibrations, another useful ability from the perspective of a "molecular toolbox". A well-known example of such an effect was shown in classic work by Smalley and coworkers who studied vibronic emission from jet-cooled n-alkybenzenes.[45,46] They demonstrated that increasing the attached alkyl chain length accelerated energy flow. For example, VR from the phenyl vibrations accelerated in C_6H_5-X when the substituent lengths were increased as X = CH_3, CH_2CH_3, $CH_2CH_2CH_3$,… and so on. The nitro- and ortho-substituents in the nitrobenzenes would presumably also generally accelerate energy flow considering the increased DOS relative to benzene. Additionally, the ortho-substituents would be expected to lower the symmetry further which may accelerate energy flow relative to nitrobenzene.[44]

However, it should be kept in mind that such predictions may not be valid as will become obvious later in this work. The golden rule doesn't take into account how the substituent

structure changes substituent-phenyl interactions and interactions within substituents and between them (in the case of ortho-substituents). If the golden rule was generally applicable, energy flow from a phenyl group to a distant substituent, such as in n-octylbenzene (X = $(CH_2)_7CH_3$) for the sake of argument, would be more preferential by virtue of the larger DOS than to one nearby, such as in toluene, which is counterintuitive. Since the 1970s, there were experiments showing clear deviations from golden rule predictions. A classic example was shown in chemical timing experiments by Parmenter and coworkers.[47] They found that energy in an excited vibrational state preferred to transfer to other states whose quantum number difference was smaller. Experiments like these made it apparent that the statistical description given by the golden rule is not generally valid and that there is a hierarchical structure to energy flow.

Rather than the total vibrational DOS applying the pressure, newer models suggest that the local density of states (LDOS) drives energy flow.[48-51] The LDOS describes the states, in the total DOS, that are effectively coupled to the initially excited state. With this in mind, vibrational energy has become more aptly described as transferring from an initially excited state to tiers of well coupled states.[52] Considering the tiered picture, it is difficult to predict how energy flow in a given substituted benzene will behave without fleshing out the intramolecular interactions found in the vibrational PES. This involves computation of individual anharmonic coupling matrix elements amongst the dense manifold of states in the total DOS which, for the molecules studied here, can become large and unwieldy. Additionally, predictions from such calculations are quite sensitive to the details of the vibrational PES. This leaves empirical approaches, like those discussed in this work, as important routes to predicting the behavior of energy flow for other substituted benzenes.

1.5 References

1. Voth, G. A.; Hochstrasser, R. M., Transition State Dynamics and Relaxation Processes in Solutions: A Frontier of Physical Chemistry. *Journal of Physical Chemistry* **1996,** *100* (31), 13034-13049.

2. Segal, D.; Nitzan, A., Heat Rectification in Molecular Junctions. *Journal of Chemical Physics* **2005,** *122* (19), 194704.

3. Segal, D.; Nitzan, A., Molecular Heat Pump. *Physical Review E* **2006,** *73* (2), 026109.

4. Li, N. B.; Ren, J.; Wang, L.; Zhang, G.; Hanggi, P.; Li, B. W., Colloquium: Phononics: Manipulating Heat Flow with Electronic Analogs and Beyond. *Reviews of Modern Physics* **2012,** *84* (3), 1045-1066.

5. Dlott, D. D.; Fayer, M. D., Shocked Molecular-Solids - Vibrational up Pumping, Defect Hot Spot Formation, and the Onset of Chemistry. *Journal of Chemical Physics* **1990,** *92* (6), 3798-3812.

6. Tokmakoff, A.; Fayer, M. D.; Dlott, D. D., Chemical-Reaction Initiation and Hot-Spot Formation in Shocked Energetic Molecular Materials. *Journal of Physical Chemistry* **1993,** *97* (9), 1901-1913.

7. Tarver, C. M., Multiple Roles of Highly Vibrationally Excited Molecules in the Reaction Zones of Detonation Waves. *Journal of Physical Chemistry A* **1997,** *101* (27), 4845-4851.

8. Segal, D.; Nitzan, A., Heating in Current Carrying Molecular Junctions. *Journal of Chemical Physics* **2002,** *117* (8), 3915-3927.

9. Segal, D.; Nitzan, A.; Hanggi, P., Thermal Conductance through Molecular Wires. *Journal of Chemical Physics* **2003,** *119* (13), 6840-6855.

10. Galperin, M.; Ratner, M. A.; Nitzan, A., Molecular Transport Junctions: Vibrational Effects. *Journal of Physics-Condensed Matter* **2007,** *19* (10).

11. Pein, B. C.; Sun, Y.; Dlott, D. D., Controlling Vibrational Energy Flow in Liquid Alkylbenzenes. *The Journal of Physical Chemistry B* **2013,** *117* (37), 10898-10904.

12. Seong, N. H.; Fang, Y.; Dlott, D. D., Vibrational Energy Dynamics of Normal and Deuterated Liquid Benzene. *Journal of Physical Chemistry A* **2009,** *113* (8), 1445-1452.

13. Iwaki, L. K.; Deak, J. C.; Rhea, S. T.; Dlott, D. D., Vibrational Energy Redistribution in Liquid Benzene. *Chemical Physics Letters* **1999,** *303* (1-2), 176-182.

14. Riedle, E.; Neusser, H. J.; Schlag, E. W.; Lin, S. H., Intramolecular Vibrational-Relaxation of Benzene. *Journal of Physical Chemistry* **1984,** *88* (2), 198-202.

15. Sibert, E. L.; Reinhardt, W. P.; Hynes, J. T., Intramolecular Vibrational-Relaxation and Spectra of Ch and Cd Overtones in Benzene and Perdeuterobenzene. *Journal of Chemical Physics* **1984,** *81* (3), 1115-1134.

16. Callegari, A.; Merker, U.; Engels, P.; Srivastava, H. K.; Lehmann, K. K.; Scoles, G., Intramolecular Vibrational Redistribution in Aromatic Molecules. I. Eigenstate Resolved Ch Stretch First Overtone Spectra of Benzene (Vol 113, Pg 10583, 2000). *Journal of Chemical Physics* **2001,** *114* (7), 3344-3344.

17. Pein, B. C.; Sun, Y. X.; Dlott, D. D., Unidirectional Vibrational Energy Flow in Nitrobenzene. *Journal of Physical Chemistry A* **2013,** *117* (29), 6066-6072.

18. Pein, B. C.; Seong, N. H.; Dlott, D. D., Vibrational Energy Relaxation of Liquid Aryl-Halides X-C6h5 (X = F, Cl, Br, I). *Journal of Physical Chemistry A* **2010,** *114* (39), 10500-10507.

19. Pein, B. C.; Dlott, D. D., Modifying Vibrational Energy Flow in Aromatic Molecules: Effects of Ortho Substitution. *Journal of Physical Chemistry A* **2014**.

20. Ioffe, Z.; Shamai, T.; Ophir, A.; Noy, G.; Yutsis, I.; Kfir, K.; Cheshnovsky, O.; Selzer, Y., Detection of Heating in Current-Carrying Molecular Junctions by Raman Scattering. *Nature Nanotechnology* **2008,** *3* (12), 727-32.

21. Dlott, D. D., Multiphon up-Pumping in Energetic Materials In *Overviews of Recent Research on Energetic Materials*, Thompson, D.; Brill, T.; Shaw, R., Eds. World Scientific: Hackensack, New Jersey, 2005; pp 303-333.

22. Dlott, D. D., Fast Molecular Processes in Energetic Materials. In *Energetic Materials: Initiation, Decomposition and Combustion, Part 2*, Politzer, P.; Murray, J. S., Eds. Elsevier: New York, 2003; pp 125-192.

23. Laubereau, A.; Kaiser, W., Vibrational Dynamics of Liquids and Solids Investigated by Picosecond Light-Pulses. *Reviews of Modern Physics* **1978,** *50* (3), 607-665.

24. Chen, S.; Lee, I. Y. S.; Tolbert, W. A.; Wen, X. N.; Dlott, D. D., Applications of Ultrafast Temperature Jump Spectroscopy to Condensed Phase Molecular-Dynamics. *Journal of Physical Chemistry* **1992,** *96* (18), 7178-7186.

25. Chen, S.; Hong, X. Y.; Hill, J. R.; Dlott, D. D., Ultrafast Energy-Transfer in High Explosives - Vibrational Cooling. *Journal of Physical Chemistry* **1995,** *99* (13), 4525-4530.

26. Hong, X. Y.; Chen, S.; Dlott, D. D., Ultrafast Mode-Specific Intermolecular Vibrational-Energy Transfer to Liquid Nitromethane. *Journal of Physical Chemistry* **1995,** *99* (22), 9102-9109.

27. Lauberea.A; Greiter, L.; Kaiser, W., Intense Tunable Picosecond Pulses in Infrared. *Applied Physics Letters* **1974,** *25* (1), 87-89.

28. Spanner, K.; Laubereau, A.; Kaiser, W., Vibrational Energy Redistribution of Polyatomic-Molecules in Liquids after Ultrashort Infrared Excitation. *Chemical Physics Letters* **1976,** *44* (1), 87-92.

29. Sun, Y. X.; Pein, B. C.; Dlott, D. D., Three-Dimensional Spectroscopy of Vibrational Energy in Liquids: Nitromethane and Acetonitrile. *Journal of Physical Chemistry B* **2013,** *117* (49), 15444-15451.

30. Bakker, H. J., Effect of Intermolecular Interactions on Vibrational-Energy Transfer in the Liquid-Phase. *Journal of Chemical Physics* **1993,** *98* (11), 8496-8506.

31. Chesnoy, J.; Ricard, D., Experimental-Study of Vibrational-Relaxation in Liquid-Hydrogen Chloride. *Chemical Physics Letters* **1980,** *73* (3), 433-437.

32. Huse, N.; Ashihara, S.; Nibbering, E. T. J.; Elsaesser, T., Ultrafast Vibrational Relaxation of O-H Bending and Librational Excitations in Liquid H2o. *Chemical Physics Letters* **2005,** *404* (4-6), 389-393.

33. Ashihara, S.; Huse, N.; Espagne, A.; Nibbering, E. T. J.; Elsaesser, T., Vibrational Couplings and Ultrafast Relaxation of the O-H Bending Mode in Liquid H_2o. *Chemical Physics Letters* **2006,** *424* (1-3), 66-70.

34. Hamm, P.; Zanni, M., *Concepts and Methods of 2d Infrared Spectroscopy*. Cambridge University Press: 2011.

35. Rubtsov, I. V., Relaxation-Assisted Two-Dimensional Infrared (Ra 2dir) Method: Accessing Distances over 10 Angstrom and Measuring Bond Connectivity Patterns. *Accounts of Chemical Research* **2009,** *42* (9), 1385-1394.

36. Nitzan, A.; Jortner, J., Vibrational Relaxation of a Molecule in a Dense Medium. *Molecular Physics* **1973,** *25* (3), 713-734.

37. Kenkre, V. M.; Tokmakoff, A.; Fayer, M. D., Theory of Vibrational-Relaxation of Polyatomic-Molecules in Liquids. *Journal of Chemical Physics* **1994,** *101* (12), 10618-10629.

38. Gulmen, T. S.; Sibert, E. L., Vibrational Energy Relaxation of the Oh Stretch in Liquid Methanol. *Journal of Physical Chemistry A* **2004,** *108* (13), 2389-2401.

39. Cahill, D. G.; Ford, W. K.; Goodson, K. E.; Mahan, G. D.; Majumdar, A.; Maris, H. J.; Merlin, R.; Sr, P., Nanoscale Thermal Transport. *Journal of Applied Physics* **2003,** *93* (2), 793-818.

40. Shigeto, S.; Pang, Y.; Fang, Y.; Dlott, D. D., Vibrational Relaxation of Normal and Deuterated Liquid Nitromethane. *Journal of Physical Chemistry B* **2008,** *112* (2), 232-241.

41. Deak, J. C.; Iwaki, L. K.; Dlott, D. D., Vibrational Energy Redistribution in Polyatomic Liquids: Ultrafast Ir-Raman Spectroscopy of Acetonitrile. *Journal of Physical Chemistry A* **1998,** *102* (42), 8193-8201.

42. Deak, J. C.; Rhea, S. T.; Iwaki, L. K.; Dlott, D. D., Vibrational Energy Relaxation and Spectral Diffusion in Water and Deuterated Water. *Journal of Physical Chemistry A* **2000,** *104* (21), 4866-4875.

43. Bixon, M.; Jortner, J., Intramolecular Radiationless Transitions. *Journal of Chemical Physics* **1968,** *48* (2), 715-&.

44. von Benten, R. S.; Liu, Y. X.; Abel, B., Dynamical Consequences of Symmetry Breaking in Benzene and Difluorobenzene. *Journal of Chemical Physics* **2010,** *133* (13).

45. Hopkins, J. B.; Powers, D. E.; Mukamel, S.; Smalley, R. E., Vibrational-Relaxation in Jet-Cooled Alkylbenzenes .2. Fluorescence-Spectra. *Journal of Chemical Physics* **1980,** *72* (9), 5049-5061.

46. Hopkins, J. B.; Powers, D. E.; Smalley, R. E., Vibrational-Relaxation in Jet-Cooled Alkyl Benzenes .3. Nanosecond Time Evolution. *Journal of Chemical Physics* **1980,** *73* (2), 683-687.

47. Parmenter, C. S., Vibrational Redistribution within Excited Electronic States of Polyatomic-Molecules - the Spiers Memorial Lecture. *Faraday Discussions* **1983,** *75*, 7-22.

48. Callegari, A.; Pearman, R.; Choi, S.; Engels, P.; Srivastava, H.; Gruebele, M.; Lehmann, K. K.; Scoles, G., Intramolecular Vibrational Relaxation in Aromatic Molecules. 2: An Experimental and Computational Study of Pyrrole and Triazine near the Ivr Threshold. *Molecular Physics* **2003,** *101* (4-5), 551-568.

49. Logan, D. E.; Wolynes, P. G., Quantum Localization and Energy-Flow in Many-Dimensional Fermi Resonant Systems. *Journal of Chemical Physics* **1990,** *93* (7), 4994-5012.

50. Perry, D. S., Random Matrix Treatment of Intramolecular Vibrational Redistribution .1. Methodology and Anharmonic Interactions in 1-Butyne. *Journal of Chemical Physics* **1993,** *98* (9), 6665-6677.

51. Gruebele, M., Bose Statistics Triangle Rule Model for Intramolecular Vibrational Energy Redistribution. *Journal of Physical Chemistry* **1996,** *100* (30), 12183-12192.

52. Gruebele, M., Vibrational Energy Flow: A State Space Approach. *Advances in Chemical Physics* **2000,** *114*, 193-261.

Chapter 2: Experimental

2.1 Introduction

Here the details of the laser system used in each of the IR-Raman experiments are described alongside the liquid-sample delivery system, the liquids themselves and the spectrograph. Modifications required for 3D IR-Raman spectroscopy and excitation spectroscopy will be discussed in Chapter 5.

2.2 Laser System

The layout of the laser and the experimental apparatus is shown in Figure 2.1. In this laser system, amplified picosecond laser pulses from a chirped pulse amplifier (CPA) are coupled to two optical parametric amplifiers (OPAs). One OPA generates 532 nm Raman probe pulses and the other generates tunable infrared (IR) pulses that, upon difference frequency mixing in a potassium titanyl arsenate (KTA) crystal with part of the CPA output, are used to pump vibrational transitions in the 2.4-5 μm (4000-2000 cm^{-1}) range of liquids flowed from the micro-capillary jet. At the sample, the probe and pump pulses are ~1 ps and have a ~25 cm^{-1} FWHM.

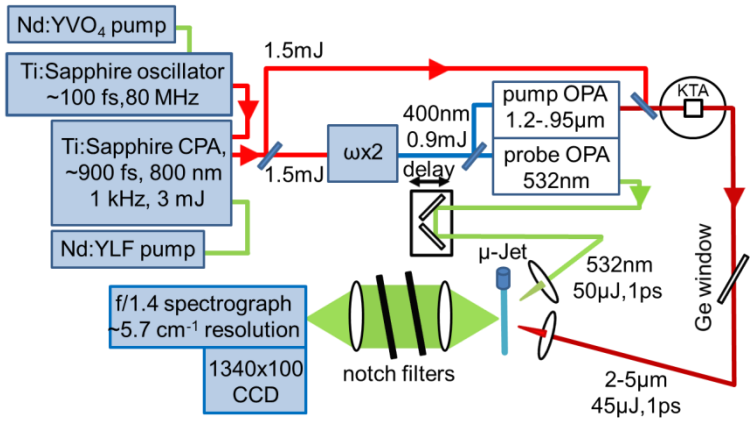

Figure 2.1. Diagram of laser and experimental apparatus. Overall layout of laser and experimental apparatus. The colored lines show the beam paths and the arrows their directions.

Laser Oscillator

The oscillator is the starting point. It produces low energy ultrashort pulses that are amplified by the CPA. For these experiments a Kapteyn-Murnane Laboratories L.L.C Ti:Sapphire passively mode-locked oscillator is used. A schematic of the cavity is shown in Figure 2.2. The Ti:Sapphire rod is pumped by a Millenia Vs continuous wave Nd:YVO_4 laser generating 4.5 watts at 532 nm. The oscillator produces ~100 fs pulses, each 5 nJ, at a repetition rate of 80 MHz bringing the total output to 400 mW. The pulses have a slightly asymmetric gaussian-like spectrum centered at 800 nm with 40 nm FWHM. A photodiode is placed behind the high reflector mirror to capture an 80 MHz signal used to trigger the CPA's Pockels cell and Q-switched pump laser.

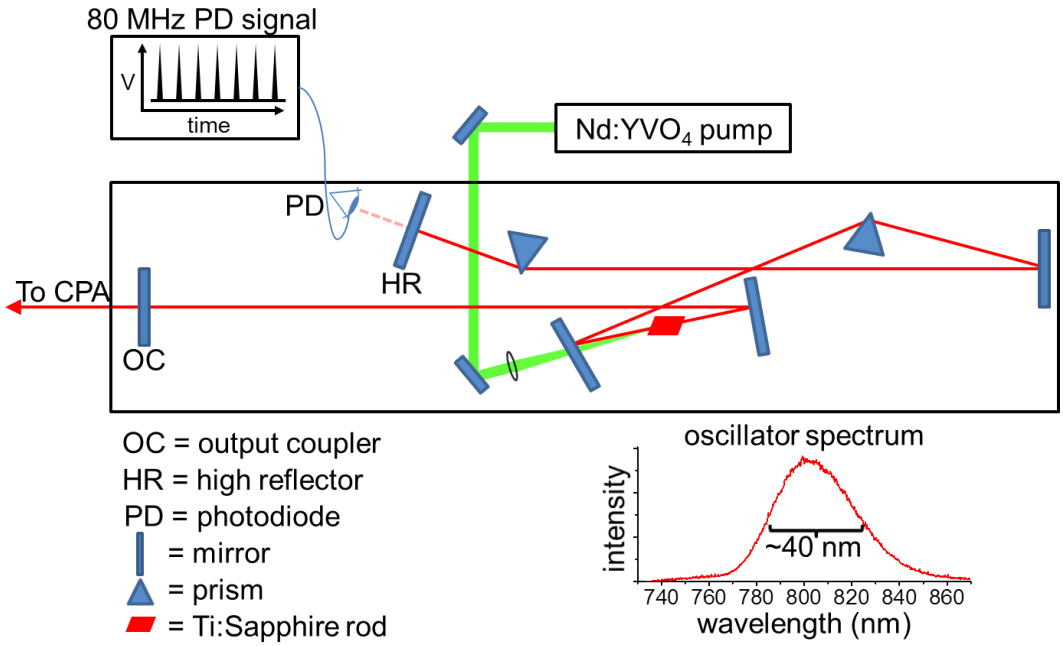

Figure 2.2. Diagram of laser oscillator. The green line shows the path of the pumping laser. The red line shows the path of the oscillator pulses. The oscillator pulse spectrum is shown as the *inset* on the bottom right. A photodiode is placed behind the high reflector to collect a triggering signal for the Q-switched laser and the Pockels cell in the amplifier.

Chirped Pulse Amplifier (CPA)

The oscillator pulses cannot simply be fed into an optical resonator for amplification. With temporal widths of ~100 fs the pulse peak power (roughly the pulse energy divided by the pulse width) will become too large and damage the gain medium. Rather, the pulses are temporally broadened, or chirped, before amplification then compressed afterwards keeping the pulse peak power below the damage threshold. This process, shown schematically in Figure 2.3, is known as chirped pulse amplification.

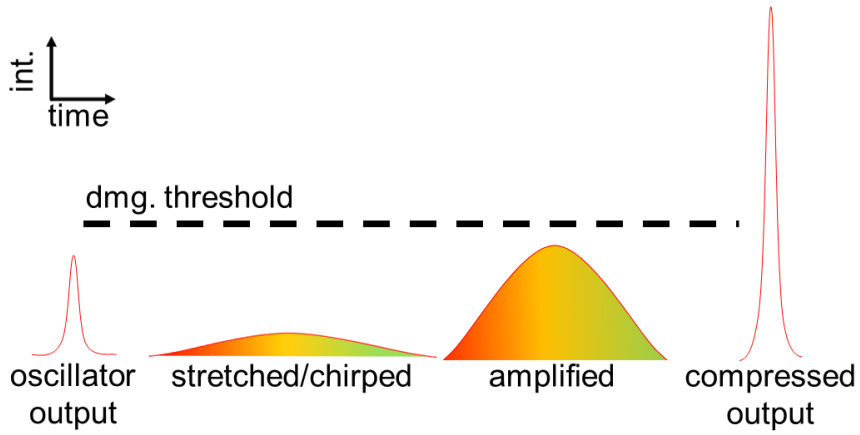

Figure 2.3. Illustration of chirped pulse amplification. The oscillator output pulses are stretched before amplification to keep their peak power below the damage threshold. After amplification the pulses are recompressed.

Here a Quantronix Titan-I CPA is used that outputs 3 mJ 800 nm ~0.9 ps pulses with a ~1 nm FWHM at a 1 kHz repetition rate. Shown in Figure 2.4, the CPA is composed of 4 separate stages: the stretcher, the regenerative amplifier, the multipass amplifier and the compressor. The amplifying stages operate using separate Ti:Sapphire rods for gain medium that are pumped by ~200 ns 15 mJ pulses from a Quantronix Darwin Nd:YLF Q-switched laser centered at 527 nm.

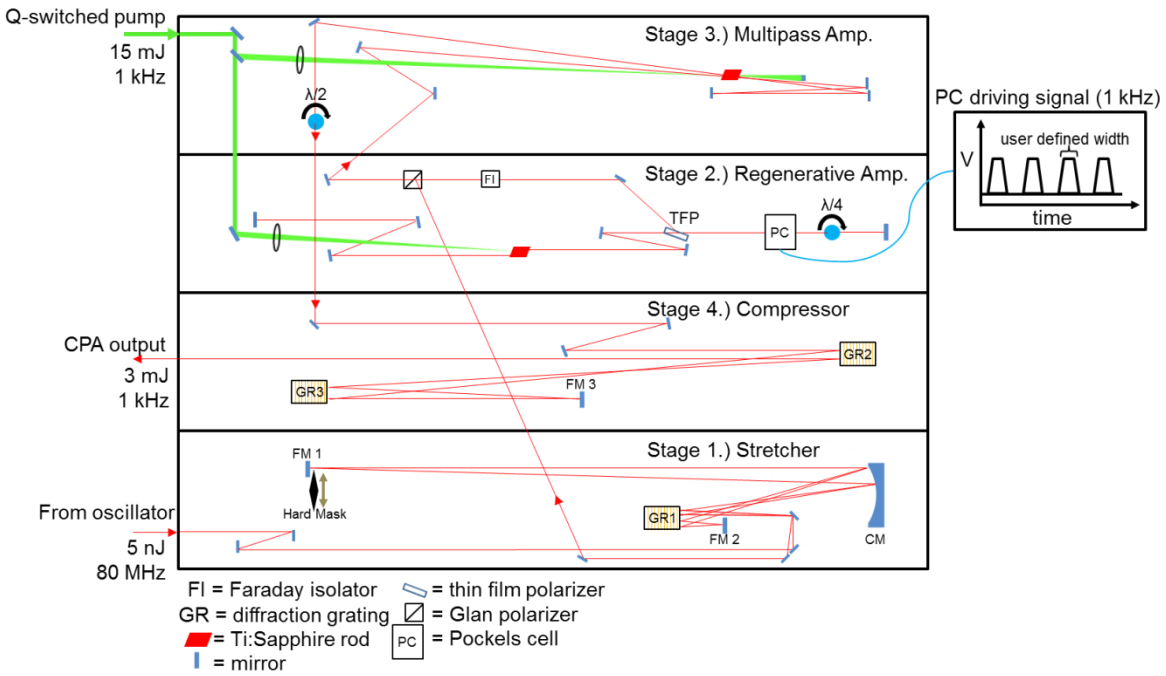

Figure 2.4. Diagram of Titan-I chirped pulse amplifier. The different stages are demarcated by the horizontal lines. The red lines show the path of the input oscillator and amplified pulses. The green lines show the path of the Darwin Q-switched pump laser. The PC driving signal is generated from the 80 MHz oscillator signal using an RF divider.

CPA Stage 1: Stretcher

The stretcher chirps the oscillator pulses from ~100 fs to ~100 ps. The pulses are first diffracted off a grating (GR1) forming a vertically elongated beam image with the longer wavelengths positioned at the top. The elongated image is reflected off a curved mirror (CM) twice, hitting the folding mirror (FM1) in the process, before returning to GR1 where the chirp is applied. Since GR1 is tilted, the longer wavelengths at the top of the elongated beam image take a shorter path length compared to the shorter wavelengths at the bottom. This equivocates to the shorter wavelengths lagging behind the longer wavelengths forming what is known as a positive chirp. A simplified diagram of this process is shown in Figure 2.5. The return through the CM/FM1 path refocuses the elongated beam image back onto GR1 which recombines the now chirped wavelengths back into their original beam image shape fed into the stretcher.

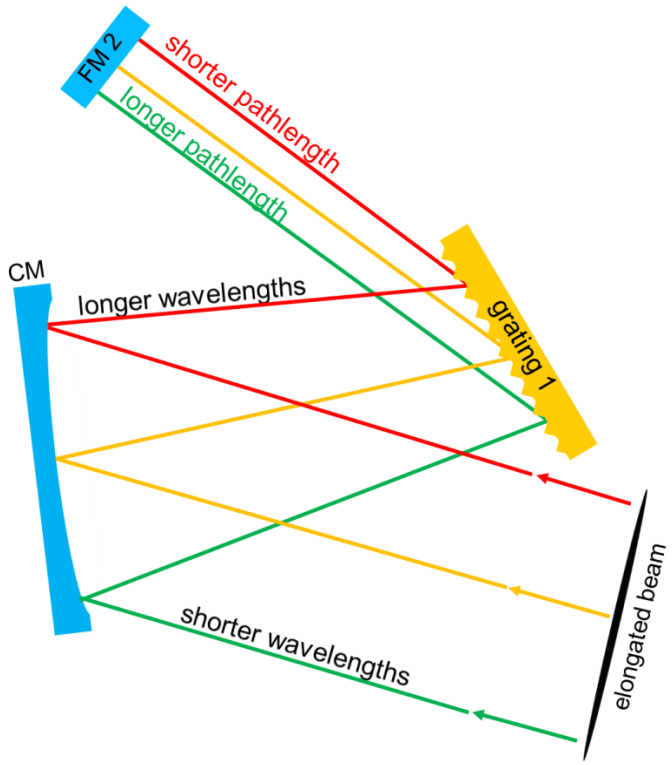

Figure 2.5. Illustration of pulse stretching. Here a positive chirp is applied to the pulses. The elongated beam image (the thin black line) is created from diffracting off the first pass of the grating. The second and third passes, shown here, create a shorter pathlength for the longer wavelengths and a longer pathlength for the shorter wavelengths. Key: CM = curved mirror, FM 2 = folding mirror #2.

To selectively excite and probe specific vibrations in organic liquids the bandwidth of the oscillator pulses must be reduced before amplification. To do this a hard mask is inserted in front of the FM1. The hard mask is a thin piece of milled metal that blocks portions of the elongated beam image passing through the CM/FM1 path. Computer calculations are used to determine a milling pattern that produces a Gaussian spectrum. The bandwidth is significantly reduced from 40 nm before the stretcher to ~1nm after the stretcher as shown in Figure 2.6.

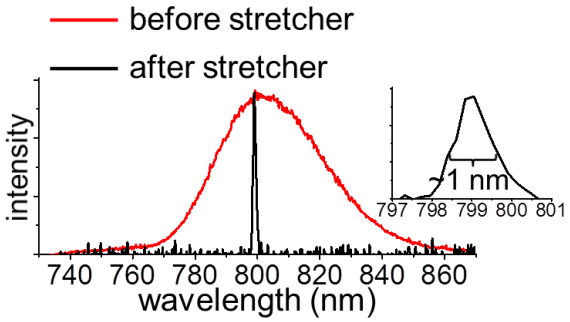

Figure 2.6. Spectrum of oscillator pulses before and after the stretcher. The stretcher has a hard-mask that substantially narrows the bandwidth. The bandwidth of the laser pulses must be narrowed to selectively pump and probe vibrations. The *inset* shows a zoomed in perspective of the spectrum after the stretcher.

CPA Stage 2: Regenerative Amplifier

Only 1 out of the 80,000 stretched pulses that reach the regenerative amplifier (RGA) each millisecond is injected by the Pockels cell (PC) to be amplified. The PC functions as an optical shutter to let pulses into the RGA cavity. The 80 MHz signal collected from the oscillator is frequency divided using an RF divider to generate a 1 kHz trigger that can switch the PC on for a user defined time window and trigger the Q-switched pump laser each millisecond. Combined with an external λ/4-plate, the PC forms a λ/4-plate when off and a λ/2-plate when on. When the PC is off, a pulse is rotated from vertical to horizontal after entering and returning from the PC. The now horizontal pulse can pass through the thin-film polarizer (TFP) and enter the RGA cavity. Before the next pulse can enter, the PC is triggered to form a λ/2-plate which doesn't affect the polarization of pulses entering and returning so the newly injected pulse remains trapped in the RGA and subsequent pulses are kept out by the TFP. The triggering window traps the pulse for 15-20 round trips when it is gradually amplified to 400 μJ by the Ti:Sapphire rod pumped with the Q-switched laser. At the end of the triggering window the PC is shut off and reverted back to a λ/4-plate which lets the amplified pulse out of the RGA. One millisecond later the PC is triggered again and the amplification process starts over.

CPA Stage 3: Multipass Amplifier

Each of the amplified RGA pulses is directed to the multipass amplifier (MPA) for a final round of amplification. The MPA Ti:Sapphire rod is pumped with ~7 times the Q-switched laser power compared to the RGA. On the first pass, the RGA pulse energy is increased from 400 μJ to 2.2 mJ. The second pass further increases this to 4.5 mJ. Here the nature of the pulse's temporal chirp becomes an issue. Since the pulses are positively chirped, their temporally leading edge, composed of the longer wavelengths, experiences more gain which creates a significant asymmetry in the spectrum as demonstrated in Figure 2.7. To correct the asymmetry, the spectrum after the MPA is monitored while the hard mask in the stretcher is finely adjusted. Finally, since the compressor gratings in the next stage are optimized for vertically polarized light, the pulse polarization is rotated using a λ/2-plate.

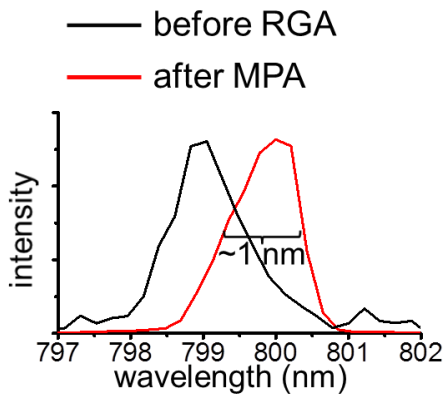

Figure 2.7. Spectrum of pulses before and after amplification. Since the pulses have a positive chirp (longer wavelengths arriving first) the longer wavelengths experience more gain than the shorter wavelengths. Note that the spectra have been normalized.

CPA Stage 4: Compressor

The compressor reverses the chirp applied by the stretcher. It consists of two gratings (GR2 and GR3) with a folding mirror (FM3). The amplified pulses are diffracted off GR2 then GR3 immediately afterwards. As shown in Figure 2.8, the gratings are tilted in such a way that

the longer wavelengths at the leading end of the pulses have a longer pathlength through the compressor than the shorter wavelengths which cancels the stretcher chirp. The pulses are reflected by FM3 and make a horizontally offset path back to GR2. After diffracting off of GR2 for the second time the pulses are returned to their input image shape with the stretcher chirp now removed and are allowed to exit the CPA. Accounting for losses from multiple grating diffraction orders and imperfect mirror reflections, the compressor outputs 3 mJ pulses.

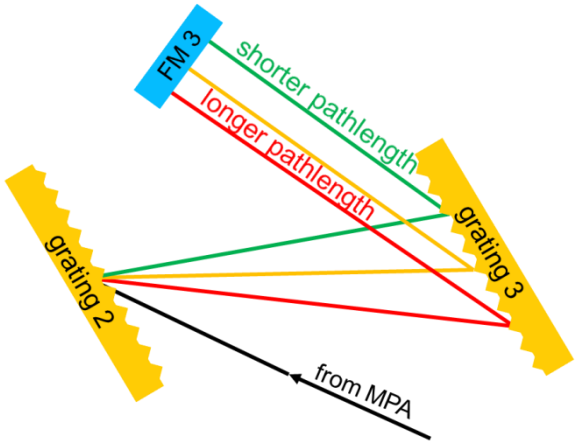

Figure 2.8. Illustration of pulse compression. To remove the positive chirp given by the stretcher the shorter wavelengths are now given a shorter pathlength while the longer wavelengths are given a longer pathlength.

Care must be taken when aligning the compressor to assure a good pulse quality. To obtain transform limited pulses the gratings must be iteratively tilted while monitoring the pulse autocorrelation after the compressor. Typically, with meticulous alignment, pulses can be compressed to ~0.9 ps which is nearly transform limited. The pulse spatial chirp must also be checked by sampling the spectrum of the beam image at different locations. Like the positive temporal chirp given by the stretcher where the shorter wavelengths trail behind the longer, a spatial chirp, illustrated in Figure 2.9, describes a situation where the longer wavelengths are spatially separated from the shorter in the beam spatial profile. This is a symptom of a tilted pulse front caused by the compressor grating grooves not being parallel to each other which can

negatively affect the subsequent portions of the laser described below. A single-shot autocorrelator is used to monitor the tilt of the pulse front while the gratings are iteratively rotated to align the grooves and eliminate the spatial chirp.

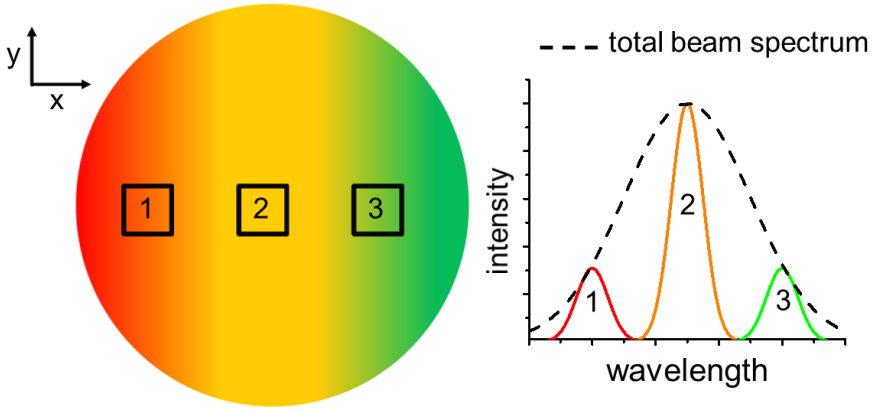

Figure 2.9. Illustration of a spatial chirp. Spatial chirp is a symptom of a tilted pulse front. The illustration shows a perspective of the beam looking down the optic axis (z). A spatial chirp has different wavelength components at different positions on the beam profile as shown in the spectrum on the right. A beam without a spatial chirp should have the same spectrum at each position.

Optical Parametric Amplifiers (OPAs)

The OPAs convert the 800 nm CPA pulses to ranges suitable for exciting vibrational transitions in the 2.4-5 μm (4000-2000 cm^{-1}) range and probing them via Raman scattering. The CPA output is equally split and half is directed into a frequency doubler (ωx2). Through a second order nonlinear optical process known as second harmonic generation, the frequency doubler, composed of a beta barium borate (BBO) crystal, upconverts the 1.5 mJ 800 nm pulses to 0.9 mJ 400 nm pulses. Half of each 400 nm pulse is directed into the pump and probe OPAs.

The OPAs used here are Light Conversion Traveling-wave Optical Parametric Amplifier of Superfluorescence (TOPAS) units. They function by a second order nonlinear process known as three photon parametric interaction. A 400 nm pulse is directed collinearly with a signal pulse of longer wavelength into a lithium triborate (LBO) crystal. As the two pulses travel through the

crystal, 400 nm photons are converted into signal photons and a third type of photon called the idler. The wavelength of the idler is determined from,

$$\frac{1}{\lambda_{400\,nm}} = \frac{1}{\lambda_{signal}} + \frac{1}{\lambda_{idler}} \tag{2.1}$$

which, multiplying by *hc*, one can easily see is simply an argument of energy conservation. In this picture, when interacting with a signal photon a 400 nm photon is converted into signal and idler photons whose combined energy is equivalent the 400 nm photon energy. Since the signal/400 nm photon interaction generates a new signal and idler photon, this process amplifies the signal. The TOPAS units are capable of generating a wavelength-tunable range of signals which, by Equation 2.1, is equivalent to a tunable idler.

The TOPAS units have a rather complicated optical configuration and describing this in detail, like the CPA, isn't tractable so only a rudimentary description is given here. Inside each, the 400 nm pulses are split into 3 separate paths. Paths 3 2 and 1 have 90:9:1 energy ratios respectively. Path 1 involves 3 individual passes through the LBO crystal the first of which generates a broadband superfluorescence pulse that is subsequently diffracted off of a grating mounted to a motor controlled turret separating its wavelength components in space. The grating is rotated such that a desired wavelength, the signal, is reflected back to the LBO crystal. The second pass of the 400 nm pulses in path 1 is overlapped spatially and temporally with the signal on the crystal which amplifies the signal. The signal continues traveling with the 400 nm pulses for a third pass amplifying it further. The amplified signal is directed collinearly with the path 2 400 nm pulses into the crystal amplifying the signal again. Finally the amplified signal is overlapped with the path 3 400 nm pulses for a final amplification pass, generating the majority of the idler as well, before exiting the OPA. The tunable signal range of the pump OPA is kept to

600-690 nm giving a 1.2-0.95 μm idler range while the probe OPA signal is kept fixed at 532 nm with a 1.61 μm idler. A longpass filter removes the signal and residual 400 nm pulses outside the pump OPA while the idler and residual 400 nm pulses are filtered from the probe OPA output using a wavelength separator. The pump OPA idler pulses are 15-20 μJ depending on the wavelength while the probe OPA 532 nm signal pulses are 50 μJ.

The signal pulses from the probe OPA, which are the probe pulses in the experiment, are sent through an Aerotech motor controlled delay line and a 0.8 nm bandpass filter, bringing their bandwidth to ~25 cm^{-1} FWHM, to clean out any stray light that isn't 532 nm before focusing to a 50 μm spot size onto the micro-capillary sample jet. The 1.2-0.95 μm idler pulses from the pump OPA are spatio-temporally overlapped with the second half of the 800 nm CPA output in a KTA crystal to produce 2.4-5μm (4000-2000 cm^{-1}) IR pulses, which are the pump pulses in the experiment, with 40-50 μJ depending on the wavelength and a ~25 cm^{-1} FWHM. This process, called difference frequency generation (DFG), is a type of three photon parametric interaction. This tunable range is ideal for exciting fundamental, overtones and combination bands in organic liquids. The pump pulses are directed through a germanium window to filter out any extraneous light from other nonlinear process in the KTA crystal before focusing to a 60 μm spot size onto the micro-capillary sample jet using a silicon meniscus lens. At the sample the pump and probe pulses are ~1 ps, which is slightly longer than the ~0.9 ps CPA output pulses. The apparatus temporal response was determined by cross-correlating the pump and probe pulses in water and monitoring the nonlinear scattering signal (NLS) at $\omega_{IR} + \omega_{vis}$ as a function of the delay. The temporal response was ~1 ps FWHM.

2.3 Micro-Capillary Sample Jet

The inherently weak cross-sections of Raman scattering require that background signals be minimized as much as possible. Because of this liquid jets are the most suitable since they don't utilize windows that can generate fluorescence and nonlinear signals when interacting with the pump and probe pulses.[1-3] Over the years several iterations of the sample jet have been used. To reduce the sample volume and losses from evaporation which, as mentioned below, is a health concern, a smaller jet design is preferred. A 60 μm inner diameter stainless steel capillary jet was found to produce the best results. Shown in Figures 2.1 and 2.10, the jet is mounted on a 3 axis stage in front of the light collection camera lenses.

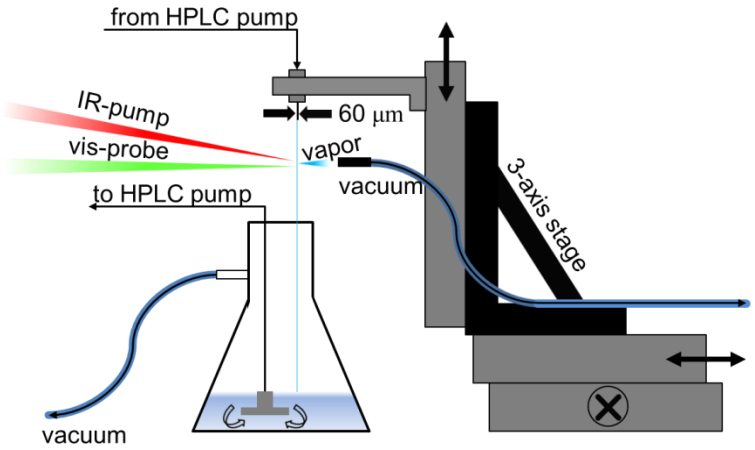

Figure 2.10. Diagram of liquid jet apparatus. The liquids are fed through a stainless steel microcapilary jet 60 μm in diameter into an Erlenmeyer flask. The jet is mounted on a 3-axis stage allowing for precise positioning. Vacuums are attached to the flask and positioned behind the beam interaction area to capture the toxic vapors.

The liquids are flowed into a side arm Erlenmeyer flask and recycled using a Hewlett Packard Series II 1090 liquid chromatography pump which utilizes a dual-syringe pump that almost entirely eliminates periodic pressure fluctuations that the previous single-syringe chromatography pump had.[4] It is important to avoid such fluctuations as they cause the liquid jet diameter to change leading to periodic changes in Raman intensity. Additionally, the liquids

studied here are rather toxic so care must be taken when using a liquid jet. The pump and probe laser pulses oftentimes boil the liquids when aligning the beams on the jet which creates a cone of nebulized liquid that must be removed from the air. A nozzle attached to a vacuum line is thusly positioned behind the laser interaction area on the jet. To avoid vapor escaping the flask a vacuum line is also attached to the flask's side arm. As a final precaution, the entire sample jet apparatus is encased in a black acrylic box with multiple vacuum lines attached to keep any extraneous vapor from escaping.

2.4 Raman Spectrograph and FTIR Instrument

The scattered light is collected and imaged 1:1 onto a 50 μm spectrograph slit using two Nikon f/1.4 camera lenses with two Kaiser Optical holographic notch filters placed in between to remove the Rayleigh scattering signal centered at 532 nm. The spectrograph, also made by Kaiser Optical, has an f/1.4 aperture and a holographic volume diffraction grating that images a 443-671 nm spectrum onto a Princeton Instruments 1340x100 liquid nitrogen cooled multichannel CCD detector with a 20 μm pixel pitch making its dispersion 5.7 cm^{-1}/pixel. The wavelength dependent pixel response is not flat across the 443-671 nm range so the CCD was calibrated using an Ocean Optics black body source. In each of the experiments, each individual spectrum at each delay was collected using a 2 minute integration time. Due to the bandwidth of the probe pulses the Raman spectra had a ~20-25 cm^{-1} resolution. A representative spectrum of a liquid (Fluorobenzene) at ambient temperature is shown in Figure 2.11 on a semi-log scale. The IR spectra presented in each of the experiments were collected using a Nicolet Magna-IR 760 FTIR instrument with a 4 cm^{-1} resolution.

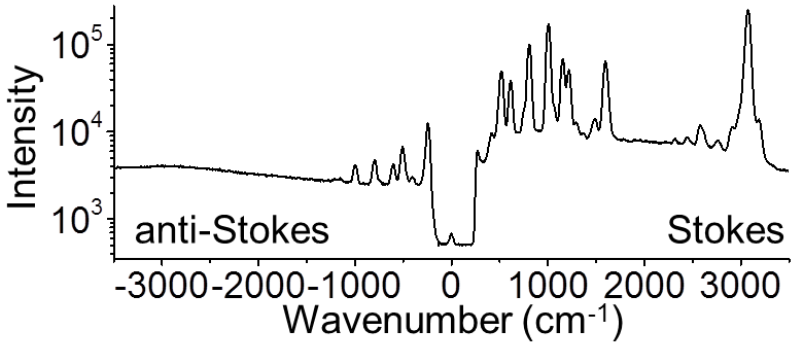

Figure 2.11. Example Raman spectrum collected from fluorobenzene at ambient temperature. The y-axis is shown in a logarithmic scale in order to see the anti-Stokes spectrum along with the Stokes.

2.5 Liquids

A list of the liquids studied in this thesis is shown in Table 2.1 along with the purity and supplier. With the exception of nitrobenzene, o-fluoronitrobenzene and o-nitrotoluene which were slightly yellow, all of the liquids were colorless. All of the liquids required no additional purification and were used as is in each of the experiments.

Liquid:	Purity:	Supplier:
Fluorobenzene	99.0%	Sigma Aldrich
Chlorobenzene	99.8%	Sigma Aldrich
Bromobenzene	99.0%	Acros Organics
Iodobenzene	98.0%	Sigma Aldrich
Nitrobenzene	>99%	Acros Organics
o-fluoronitrobenzene	99.0%	Sigma Aldrich
o-nitrotoluene	≥99%	Sigma Aldrich
Toluene	99.5%	Sigma Aldrich
Isopropylbenzne	98.0%	Sigma Aldrich
Tertbutylbenzene	99.0%	Sigma Aldrich
Nitromethane	≥98.5%	Sigma Aldrich
d3-Nitromethane	>99% (99% isotopic purity)	Cambridge Isotope
Acetonitrile	99.8%	Sigma Aldrich
d3-Acetonitrile	>99% (99% isotopic purity)	Cambridge Isotope

Table 2.1. List of liquids studied. The purities and the supplier are indicated. With the exception of nitrobenzene, o-fluoronitrobenzene, and o-nitrotoluene which were slightly yellow, all were colorless.

2.6 References

1. Chen, S.; Hong, X. Y.; Hill, J. R.; Dlott, D. D., Ultrafast Energy-Transfer in High Explosives - Vibrational Cooling. *Journal of Physical Chemistry* **1995,** *99* (13), 4525-4530.

2. Chen, S.; Lee, I. Y. S.; Tolbert, W. A.; Wen, X. N.; Dlott, D. D., Applications of Ultrafast Temperature Jump Spectroscopy to Condensed Phase Molecular-Dynamics. *Journal of Physical Chemistry* **1992,** *96* (18), 7178-7186.

3. Hong, X. Y.; Chen, S.; Dlott, D. D., Ultrafast Mode-Specific Intermolecular Vibrational-Energy Transfer to Liquid Nitromethane. *Journal of Physical Chemistry* **1995,** *99* (22), 9102-9109.

4. Pein, B. C.; Seong, N. H.; Dlott, D. D., Vibrational Energy Relaxation of Liquid Aryl-Halides X-C6h5 (X = F, Cl, Br, I). *Journal of Physical Chemistry A* **2010,** *114* (39), 10500-10507.

Chapter 3: IR-Raman Spectroscopy†

3.1 Introduction

IR-Raman spectroscopy is a technique where IR pulses pump a selected vibration, called the parent, and time-delayed visible pulses simultaneously probe, via spontaneous Raman scattering, the parent and vibrations excited by the parent, called the daughters. Here the principles and details of IR-Raman spectroscopy and its use towards the study of vibrational relaxation (VR) and vibrational cooling (VC) dynamics are introduced. Chapter 4 will discuss its application to a series of aryl-halides where the effect that increasing a substituent mass has on VR and VC is discussed. In chapter 5, extensions of IR-Raman spectroscopy, 3D IR-Raman and excitation spectroscopies, will be described.

3.2 Monitoring Excited Vibrations with Anti-Stokes Spectroscopy

It is well understood that only excited vibrations contribute to the anti-Stokes Raman (blueshifted) spectrum while vibrations in both excited and ground states contribute to the Stokes Raman (redshifted) spectrum. Considering organic liquids, most of the vibrational transitions have energies >>kT at ambient temperature and are thusly in the ground state, which leads to a mostly featureless anti-Stokes spectrum. If a vibration is excited with IR pump pulses, its detection using the anti-Stokes spectrum is quite sensitive since one is always comparing changes relative to a mostly featureless background.[1,2] The Stokes spectrum can provide the same information, however, this is more difficult.[3,4] This is because one must measure the slight changes in stokes intensity relative to the ambient temperature background[4] which can be

†Parts of this chapter are recreated from works previously published as: (1) Pein, B. C.; Dlott, D. D., Vibrational Energy and Molecular Thermometers in Liquids: Ultrafast IR-Raman Spectroscopy. In *Ultrafast Infrared Vibrational Spectroscopy*; Fayer, M.D., Ed.; Taylor & Francis: Boca Raton, 2013; p 269. (2) Sun, Y.; Pein, B. C.; Dlott, D. D., Three-Dimensional Spectroscopy of Vibrational Energy in Liquids: Nitromethane and Acetonitrile. *Journal of Physical Chemistry B* **2013**, *117(49)*, 15444.

multiple orders of magnitude larger in intensity. Additionally, since both the ground state and excited states contribute to the Stokes spectrum, one must distinguish the changes due to ground state depletion and excited state scattering, an issue the anti-Stokes spectrum does not have. The anti-Stokes spectrum will thusly be the primary means of probing vibrations in this thesis.

3.3 Vibrational Populations

A Raman spectrum quantitatively measures vibrational populations. Once a pumping wavenumber is chosen the incident Raman probe pulses are delayed relative to the pump pulses from -3 ps (probe precedes the pump) to +100 ps (pump precedes the probe). The collected Raman spectra at each delay make up the IR-Raman spectrum. Using probe pulses with frequency ω_L, at each delay t the intensity of the Stokes signals are

$$I_{\omega}^{ST}(t) \propto \omega_L(\omega_L - \omega)^3[n_{\omega}(t) + 1]\sigma_R \tag{3.1}$$

and the anti-Stokes signals are

$$I_{\omega}^{AS}(t) \propto \omega_L(\omega_L + \omega)^3 n_{\omega}(t)\sigma_R \tag{3.2}$$

where σ_R is the Raman scattering cross section at ω_L and $n_{\omega}(t)$ is the absolute transient population, or occupation number, of a vibration with frequency ω in the excited state. The proportionality constant is dependent on the collection system and is thusly the same for both. In the case that n_{ω} is << 1, which is generally the true in these experiments since the anti-Stokes signals are quite weak, Equation 3.1 and 3.2 are combined to give

$$n_{\omega}(t) \approx \frac{I_{\omega}^{AS}}{I_{\omega}^{ST}}\left[\frac{\omega_L - \omega}{\omega_L + \omega}\right]^3 \tag{3.3}$$

meaning that the absolute transient population $n_{\omega}(t)$ of a vibration at ω is proportional to the fraction I^{AS}/I^{ST} at each delay t. For multiply degenerate modes, Equation 3.3 represents their combined population. It is important to note that when n_{ω} is << 1 the Stokes stays almost constant so only a single set of Stokes intensities at a single delay are required in 3.3 (in the

experiments shown in this thesis the Stokes intensities at -3 ps are used). From a delay-time series of Raman spectra, the integrated intensities are fit with a Voigt line shape using Microcal Origin software.[5] The Voigt line shape is simply the best fitting and not a preconceived notion of the nature of the vibrational dephasing.[5]

The absolute transient populations derived here can be used in these experiments, however in practice, as will be seen in Chapter 4 and beyond, the transient population change $\Delta n_\omega(t)$ is what is actually computed. In this way the effects of IR pumping are visually far more tractable in the discussions and analysis. To do this, the anti-Stokes spectrum at negative pump-probe delay (in these experiments the -3 ps spectrum) is subtracted off of each subsequent spectrum in the IR-Raman spectrum. The intensity changes in these anti-Stokes difference spectra are fit and used in Equation 3.3, in place of the I_{AS} intensities, to compute $\Delta n_\omega(t)$.

3.4 Vibrational Energy Density

Discussed thus far, the transient population change $\Delta n_\omega(t)$ is an indication of the number of molecules that have an excited vibration at ω after the IR pump pulses arrive. However, it lacks information about the actual energy content in each vibration which will be important in Chapters 7-9 when discussing VR and VC as a nanoscale thermal conduction process. To monitor the energy content, the vibrational energy density change ΔE (J/cm^3) can be computed which indicates the change in energy in a vibration relative to its ambient temperature content. For a vibration at frequency ω, number density ρ and population change $\Delta n_\omega(t)$ the energy density change at delay time t is

$$\Delta E_\omega(t) = \rho h\omega \Delta n_\omega(t) \qquad (3.4)$$

where h is Planck's constant. In the liquids studied in this thesis, typical values for ΔE range from ~1-5 J/cm^3 depending on the vibration. It should be kept in mind that due to the IR

absorption coefficients, which result in an exponential attenuation into the sample, and the gaussian beam profiles of the pump and probe, the energy densities are spatially averaged over an inhomogeneous energy distribution in the probed sample volume.

3.5 Temperature Jump of Liquids

After pumping the molecules, eventually a thermalized (or thermally equilibrated) state at an elevated temperature ΔT is reached when the VC process is complete. For the substituted benzenes studied here, this usually occurs by ~30 ps. For a liquid with a constant volume heat capacity C_v and number density ρ, the temperature jump (T-jump) ΔT can be predicted with good accuracy using

$$\Delta T = \frac{J\alpha}{\rho C_v} \tag{3.5}$$

where J is the IR pump pulse fluence (J/cm^2) and α is the absorption coefficient at the IR pump wavenumber.[6] As the absolute vibrational populations reach constant values the ratios of any two, n_i and n_j, can be computed with the familiar relation

$$\frac{n_i}{n_j} = e^{\frac{h(\omega_j - \omega_i)}{k(T_o + \Delta T)}} \tag{3.6}$$

where h is Planck's constant, k is the Boltzmann constant and T_o is the ambient temperature. Typically the vibrations <1000 cm^{-1} are used to compute the T-jump since these have the largest populations after the liquids have thermalized. In the substituted benzenes studied here the T-jump range from ~10-40K using ~40-50 μJ IR pump pulses.

3.6 A Tool to Study Energy Flow

To interpret the energy flow using the transient populations, a model must be introduced. As mentioned in Chapter 1, VC can be described as several VR steps that bring the liquid molecules to a thermalized state. For smaller molecules, such as diatomics, in condensed phases

VC is portrayed as a vibrational cascade where highly excited vibrations, say with 20 quanta in the case of Xe-F, descend a ladder of vibrational states with progressively fewer quanta eventually leading to a thermalized state.[7] For larger polyatomic molecules, however, a ladder-like decent becomes less and less valid as shown by hot fluorescence and IR-Raman studies. In those works, it was shown that energy from pumped vibrations would randomize instead.[8]

To better describe the VR and overall VC process in condensed phase polyatomic molecules, the Dlott laboratory developed a three-stage model[5,9,10] depicted in Figure 3.1. Here, the vibrational states are broken up into 4 different categories based on previous work[11]. The first is the higher-level states, composed of the parents generated by the IR pump pulses, whose transition energies are in the 2000-4000 cm^{-1} range. The second and third are the mid- and low-level states in the ~1000-1600 cm^{-1} and ~<1000 cm^{-1} range respectively. The fourth is the continuum of lowest energy states that make up the bath.

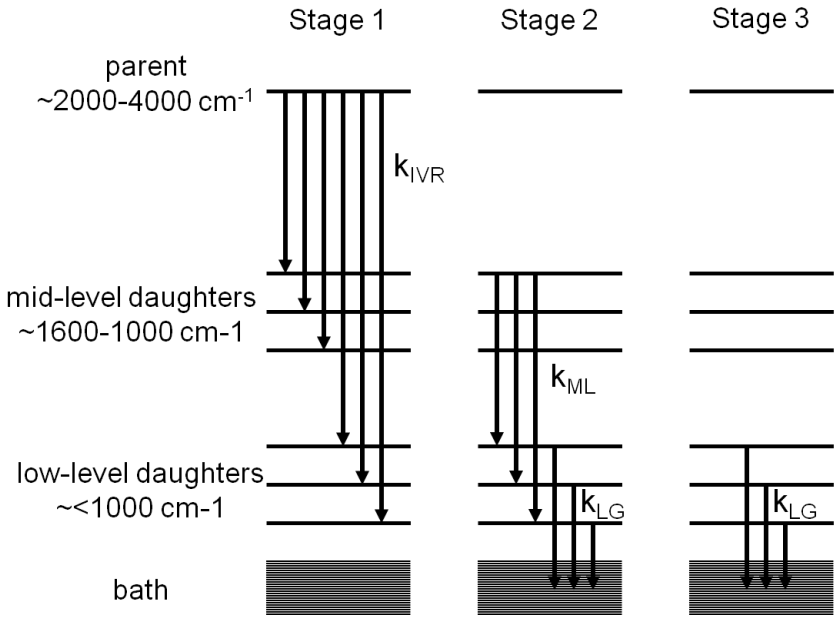

Figure 3.1. Diagram of three-stage model for VR and VC. During stage 1, the pumped parent P decays to the mid- and low-level daughters via IVR processes with a rate k_{IVR}. During stage 2, the now populated mid-level daughters, excited by the parent, excite low-level daughters while the low-level daughters excite the bath with rates k_{ML} and k_{LG} respectively. During stage 3, the low-level daughters then continue to excite the bath.

In the first stage of the three-stage model, the parent (denoted P), or bright state, is excited by the IR-pump pulses. The rate of excitation can be described as $\alpha J(t)$ where α is the absorption coefficient and $J(t)$ is the time-dependent pump fluence. Other states, such as mid- and low-level (denoted M and L) or those similar in energy to the parent, that are strongly coupled to the parent, can also be excited by the pump pulses via an intramolecular VR (IVR) process. These states are referred to as "coherently coupled" to the parent which is a term used to describe an excitation by another vibration that occurs faster or on a comparable time scale to the vibrational dephasing time T_2.[12,13] An example of coherent coupling is a 2:1 Fermi resonance that occurs between a CH-stretch and a CH-bend, where a stretch state with a single quanta is coupled to a bend state with two quanta. In this case, an IR-pumped CH-stretch state will have some CH-bend character excited along with it. If the time resolution is high enough when measuring such a process, quantum beats can be measured,[14,15] where populations could be seen oscillating back and forth between the stretch and coherently coupled bend before dephasing. However, the picosecond IR-pump and probe pulses used in this thesis are longer than T_2 and shorter than the T_1 population lifetimes, so resolving quantum beating is impossible.[16] Rather, the oscillating populations are effectively averaged over T_2 in these experiments, so states coherently coupled to the parent are observed as instantaneously excited populations.

Once P is excited, its population begins to fall with a lifetime τ_{IVR} as it excites the first-generation of M and L daughters primarily via IVR with little to no excitation of the bath. In the substituted benzenes studied here, this usually occurs during the first ~1-3 ps.[17-20] The rate, typically described in the context of the golden rule as discussed in Chapter 1, is viewed as resulting from intramolecular interactions via the vibrational potential energy surface (PES) and the vibrational density of states (DOS). The quantum yield, or efficiency, describes the relative

levels of M and L daughter populations generated by IVR from the parent. For M and L daughters *i* and *j*, the yield of the parent P to excite these states is φ_{PMi} and φ_{PLj} respectively and can be determined experimentally. However, the specific M daughters that excite specific L daughters are not determined experimentally. Instead, what is observed is the net yield describing all M states exciting L state *j*, which is written as $\varphi_{MLj}\sum M_i(t) = \sum \varphi_{MiLj} M_i(t)$ where φ_{MiLj} are the individual yields and φ_{MLj} is the net yield.

For the second stage, the populations in the M daughter states fall with a lifetime τ_{ML}, which is typically on the ~5-10 ps timescale in the substituted benzenes studied here,[17-20] exciting a second-generation of L daughter states and some of the bath, while the L states fall with a lifetime τ_{LG} (G denotes the vibrational ground state) exciting the bath. This occurs via both intra- and intermolecular VR processes which are not necessarily distinguishable in IR-Raman experiments. Finally during the third stage, the remaining population in second-generation L daughter states begins to decay and the bath is further excited with the lifetime τ_{LG}, which can range from ~20-50 ps for substituted benzenes[17-20]. Again, this stage is also composed of intra- and intermolecular processes.

To simplify this model and avoid having several fitting parameters, the lifetimes of the M daughters τ_{ML} and the L daughters τ_{LG} is assumed to be the same. This means that the variations in the individual state lifetimes in these tiers are minimal and if this is not the case then additional corrections need to be made. As shown in Figure 3.1, the VR processes in the three-stage model are described by global rate constants $k_{IVR} = (\tau_{IVR})^{-1}$, $k_{ML} = (\tau_{ML})^{-1}$ and $k_{LG} = (\tau_{LG})^{-1}$. The three-stage model can thusly be described using the following set of differential equations

$$\frac{dP(t)}{dt} = -k_{IVR}[P(t) - P^{eq}] + \alpha J(t)$$

$$\frac{dM_i(t)}{dt} = k_{IVR}\varphi_{PMi}[P(t) - P^{eq}] - k_{ML}[M_i(t) - M_i^{eq}] + \alpha' J(t) \quad (3.7)$$

$$\frac{dL_j(t)}{dt} = k_{IVR}\varphi_{PLj}[P(t) - P^{eq}] + k_{ML}\varphi_{MLj}\sum_i \left[M_i(t) - M_i^{eq}\right] - k_{LG}\left[L_j(t) - L_j^{eq}\right] + \alpha'' J(t)$$

Here P^{eq}, M^{eq} and L^{eq} are the populations of the P M and L states at the thermalized or thermally equilibrated state with temperature $T^o+\Delta T$, and the superscripted α represent the rates at which the coherently coupled M and L states are excited by the IR pumped parent.

To determine the global rate constants and the quantum yields, in previous works, the P and individual M and L populations can be meticulously fit according to the above equations.[5,21] In this thesis a much easier method, though admittedly an approximation to Equation 3.7, is used, where the time constants appearing in the rising edges of the transient vibrational populations were compared to the decay lifetimes of higher energy vibrational populations to associate which VR process was responsible for the rise.[22] As shown in Chapter 4, approximate quantum yields can be determined this way by comparing the fall, in say the parent population, with the rise in the lower energy daughter populations that rise on the same time scale.

3.7 Strengths and Weaknesses of IR-Raman Spectroscopy

In the IR-Raman technique, the Raman probe is a strong tool for tracking VR in organic liquids since, in principle, it allows simultaneous monitoring of each vibration for molecules lacking a center of symmetry. Additionally, as discussed below, it has a particular sensitivity to IR transitions with weaker absorption cross sections. However, there are some notable weaknesses that must be discussed which include the selection bias of the Raman probe and the collection of nonlinear artifacts that come with using ultrashort intense pulses.

Enhanced Sensitivity

An important strength of the IR-Raman technique is that the experiments have an increased sensitivity to pump weaker IR transitions. This is a consequence of the experimental apparatus, discussed in Chapter 2, and the different optical penetration depths of the pump and probe pulses.[13] In an IR-Raman experiment, the anti-Stokes signals, resulting from pumping with IR pulses at an absorption peak and in an absorption valley, can have the same intensity. The Raman probe pulses are nonresonant and probe the entire ~60 μm thick sample. As long as the IR penetration depth is less than the sample thickness, all the IR photons will be absorbed and the number of excitations that generate the anti-Stokes signals will remain constant. It is only when the IR pulses are tuned to a region where the absorption is weak enough that the penetration depth becomes comparable to the sample thickness and the number of probed excitations begins to decrease.[13]

Raman Spectroscopy Selection Bias

Each of the substituted benzenes studied here lacks a center of symmetry so theoretically each vibration should be Raman active. In practice though, many of the vibrations are not resolvable either due to small Raman cross-sections or proximity with other vibrational frequencies. In the substituted benzenes studied in this thesis, only ~30% of the vibrations are visible which admittedly introduces a selection bias and begs the question of how representative the observed vibrational energy is of the total.

To prove that the observed energy in substituted benzenes is representative of the total, a technique based off of ultrafast calorimetry, was developed by the Dlott laboratory, is considered. In this previous work, benzene was spiked with a molecular thermometer, CCl_4,[13,22-24] which monitored the total energy dissipation from the IR-pumped benzene.[21] By subtracting

the observed energy from the total input energy, the time dependence of the unobserved energy could be determined, and except at the earliest times, its time dependence was the same as the observed energy. Thus the modes observed, at least in the phenyl groups, should provide a relatively unbiased measure of the total energy content of the phenyl groups.[21]

Artifacts

Several kinds of artifacts can be observed in IR-Raman spectra. Here artifacts mean optical signals in the anti-Stokes region, unrelated to vibrational populations, which decay with the much faster optical dephasing time constants T_2 rather than vibrational population time constants T_1. These artifacts are generated by nonlinear optical processes, and even quite high-order processes are a concern because the pump and probe pulses are intense, the samples are concentrated neat liquids, and the anti-Stokes signals are weak. Nonlinear effects that can be ignored in many pump-probe experiments become significant and sometimes overwhelming in IR-Raman experiments.[13]

The artifacts seen in IR-Raman experiments are created by processes that can broadly be described as nonlinear light scattering (NLS).[25] NLS is defined as scattered light at frequencies other than those present in the incident laser pulses. Some nonlinear laser processes produce coherent beams such as difference frequency generation (DFG) which was discussed in Chapter 2. The geometry of the IR-Raman apparatus is such that the pump and probe beams are directed away from the collection optics which minimize the detection of such coherent beams. However, in a liquid medium, the scattered light from a coherent signal can be detected and can compete with the anti-Stokes signals. For pump and probe pulse with frequencies ω_{IR} and ω_{vis} respectively, the three most important types of artifacts arise from sum-frequency generation (SFG), via the second-order nonlinear susceptibility $\chi^{(2)}$, which generates signals at $\omega_{IR} + \omega_{vis}$;

four-wave mixing (4WM), via the third-order nonlinear susceptibility $\chi^{(3)}$, which generates signals at $2\omega_{IR} + \omega_{vis}$; and self-phase modulation (SPM) of the Raman probe pulses, which spectrally broadens the probe pulses and generates signals near zero wavenumbers.

In the SFG literature, where liquid surfaces and interfaces are studied, it is frequently mentioned that $\chi^{(2)}$ vanishes in nonchiral liquids, but that is only true in the dipole approximation.[26] Quadrupole and other higher-order terms in the polarization expansion can lead to weak SFG. In all of the experiments discussed in this thesis, the liquids used generate an SFG artifact at $\omega_{IR} + \omega_{vis}$, which corresponds to the anti-Stokes wavenumber ω_{IR}. This is the same wavenumber as the parent vibrational excitation generated by the IR pump pulses. SFG artifacts appear only near $t = 0$, when the IR and visible pulses are time-coincident, so the populations of the excited parent can usually be discerned at times later than this.

A 4WM artifact depends on $\chi^{(3)}$, which is nonvanishing in all liquids, so the 4WM artifacts in liquids can be more intense than SFG artifacts. A signal at $2\omega_{IR} + \omega_{vis}$ would appear at the anti-Stokes wavenumber $2\omega_{IR}$, which is generally outside of the detected range for the tunable range of the pump pulses, and should in principle be rejected by the spectrograph used in these experiments. However because the spectrograph is imperfect, 4WM artifacts can sometimes be observed in anti-Stokes spectra as long decaying tails extending into spectrum from the higher wavenumber region. The 4WM artifacts are also observed only near $t = 0$.

The SPM artifacts are related to the ever-present issue of Rayleigh scattering backgrounds in Raman spectroscopy. These backgrounds are signals in a Raman spectrum that tail off from a maximum at zero wavenumbers. As discussed in Chapter 2, a notch filter is used to suppress Rayleigh scattering. However, due to the intensity of the probe pulses, SPM caused the spectrum of the probe pulses to broaden, and sometimes this broadened light is transmitted

through the notch filter. SPM artifacts look like Rayleigh scattering backgrounds, and are time-independent. The SPM effect can be eliminated by attenuating the probe pulses, but due to the weak signals in these experiments, the probe intensity is run right up to the SPM threshold and occasionally a laser or sample jet fluctuation will create an SPM artifact. Near $t = 0$, when the pump and probe pulses are time-coincident, the electric fields of the pump pulses enhance SPM of the probe pulses. This type of pump-enhanced SPM artifact also appears as a Rayleigh scattering background, but the pump-enhanced SPM artifact has an intensity maximum at $t = 0$.

3.8 References

1. Laubereau, A.; Kaiser, W., Vibrational Dynamics of Liquids and Solids Investigated by Picosecond Light-Pulses. *Reviews of Modern Physics* **1978,** *50* (3), 607-665.

2. Seilmeier, A.; Kaiser, W., Ultrashort Intramolecular and Intermolecular Vibrational-Energy Transfer of Polyatomic-Molecules in Liquids. *Topics in Applied Physics* **1988,** *60*, 279-317.

3. Seifert, G.; Zurl, R.; Graener, H., Novel Information About Vibrational Relaxation in Liquids Using Time-Resolved Stokes Probing after Picosecond Ir Excitation. *Journal of Physical Chemistry A* **1999,** *103* (50), 10749-10754.

4. Wang, Z. H.; Pang, Y.; Dlott, D. D., Vibrational Energy Dynamics of Water Studied with Ultrafast Stokes and Anti-Stokes Raman Spectroscopy. *Chemical Physics Letters* **2004,** *397* (1-3), 40-45.

5. Shigeto, S.; Pang, Y.; Fang, Y.; Dlott, D. D., Vibrational Relaxation of Normal and Deuterated Liquid Nitromethane. *Journal of Physical Chemistry B* **2008,** *112* (2), 232-241.

6. Hare, D. E.; Franken, J.; Dlott, D. D., Coherent Raman Measurements of Polymer Thin-Film Pressure and Temperature During Picosecond Laser-Ablation. *Journal of Applied Physics* **1995,** *77* (11), 5950-5960.

7. Hoffman, G. J.; Imre, D. G.; Zadoyan, R.; Schwentner, N.; Apkarian, V. A., Relaxation Dynamics in the B(1/2) and C(3/2) Charge-Transfer States of Xef in Solid Ar. *Journal of Chemical Physics* **1993,** *98* (12), 9233-9240.

8. Iwaki, L.; Dlott, D. D., *Vibrational Energy Transfer in Condensed Phases*. IOP Publishing Ltd.: London, 2001.

9. Shigeto, S.; Dlott, D. D., Vibrational Relaxation of an Amino Acid in Aqueous Solution. *Chemical Physics Letters* **2007,** *447* (1-3), 134-139.

10. Fang, Y.; Shigeto, S.; Seong, N. H.; Dim, D. D., Vibrational Energy Dynamics of Glycine, N-Methylacetamide, and Benzoate Anion in Aqueous (D2o) Solution. *Journal of Physical Chemistry A* **2009,** *113* (1), 75-84.

11. Nitzan, A.; Jortner, J., Vibrational Relaxation of a Molecule in a Dense Medium. *Molecular Physics* **1973,** *25* (3), 713-734.

12. Deak, J. C.; Iwaki, L. K.; Dlott, D. D., When Vibrations Interact: Ultrafast Energy Relaxation of Vibrational Pairs in Polyatomic Liquids. *Chemical Physics Letters* **1998,** *293* (5-6), 405-411.

13. Deak, J. C.; Iwaki, L. K.; Rhea, S. T.; Dlott, D. D., Ultrafast Infrared-Raman Studies of Vibrational Energy Redistribution in Polyatomic Liquids. *Journal of Raman Spectroscopy* **2000,** *31* (4), 263-274.

14. Felker, P. M.; Zewail, A. H., Direct Observation of Nonchaotic Multilevel Vibrational-Energy Flow in Isolated Polyatomic-Molecules. *Physical Review Letters* **1984,** *53* (5), 501-504.

15. Tokmakoff, A.; Kwok, A. S.; Urdahl, R. S.; Francis, R. S.; Fayer, M. D., Multilevel Vibrational Dephasing and Vibrational Anharmonicity from Infrared Photon-Echo Beats. *Chemical Physics Letters* **1995,** *234* (4-6), 289-295.

16. Iwaki, L. K.; Dlott, D. D., Three-Dimensional Spectroscopy of Vibrational Energy Relaxation in Liquid Methanol. *Journal of Physical Chemistry A* **2000,** *104* (40), 9101-9112.

17. Pein, B. C.; Seong, N. H.; Dlott, D. D., Vibrational Energy Relaxation of Liquid Aryl-Halides X-C6h5 (X = F, Cl, Br, I). *Journal of Physical Chemistry A* **2010,** *114* (39), 10500-7.

18. Pein, B. C.; Sun, Y.; Dlott, D. D., Controlling Vibrational Energy Flow in Liquid Alkylbenzenes. *The Journal of Physical Chemistry B* **2013,** *117* (37), 10898-10904.

19. Pein, B. C.; Sun, Y.; Dlott, D. D., Unidirectional Vibrational Energy Flow in Nitrobenzene. *Journal of Physical Chemistry A* **2013,** *117* (29), 6066-72.

20. Pein, B. C.; Dlott, D. D., Modifying Vibrational Energy Flow in Aromatic Molecules: Effects of Ortho Substitution. *Journal of Physical Chemistry A* **2014**.

21. Seong, N. H.; Fang, Y.; Dlott, D. D., Vibrational Energy Dynamics of Normal and Deuterated Liquid Benzene. *Journal of Physical Chemistry A* **2009,** *113* (8), 1445-1452.

22. Deak, J. C.; Iwaki, L. K.; Dlott, D. D., Vibrational Energy Redistribution in Polyatomic Liquids: Ultrafast Ir-Raman Spectroscopy of Acetonitrile. *Journal of Physical Chemistry A* **1998,** *102* (42), 8193-8201.

23. Graham, P. B.; Matus, K. J. M.; Stratt, R. M., The Workings of a Molecular Thermometer: The Vibrational Excitation of Carbon Tetrachloride by a Solvent. *Journal of Chemical Physics* **2004,** *121* (11), 5348-5355.

24. Deak, J. C.; Iwaki, L. K.; Diott, D. D., Vibrational Energy Redistribution in Polyatomic Liquids: Ultrafast Ir-Raman Spectroscopy of Nitromethane. *Journal of Physical Chemistry A* **1999,** *103* (8), 971-979.

25. Terhune, R. W.; Maker, P. D.; Savage, C. M., Measurements of Nonlinear Light Scattering. *Physical Review Letters* **1965,** *14* (17), 681-&.

26. Shen, Y. R., *The Principles of Nonlinear Optics*. Wiley-Interscience: 2003.

Chapter 4: Vibrational Energy Flow in Liquid Aryl-Halides†

4.1 Introduction

In this chapter, IR-Raman spectroscopy is used to compare the vibrational relaxation (VR) and vibrational cooling (VC) processes of the liquid aryl-halides X-Bz (X = F, Cl, Br, I, -Bz = C_6H_5) at ambient temperature. As a reminder, VR refers to the energy relaxation of specific vibrational states whereas VC refers to the thermalization process, where molecules with highly nonthermal vibrational excitations undergo sequential and parallel VR steps resulting in equilibrium at an increased temperature.[1,2] In prior works[3,4] on benzene (H-Bz) and the work presented in this chapter, the temperature jump (T-jump) ΔT depended on laser conditions and absorption coefficients, as discussed in Chapter 3, and typically ranged from 10-40K.[3] Aryl halides were chosen in part due to the previous studies of energy flow in H-Bz.[3,4] This also allows the study of energy flow in a series of molecules with a gradually increasing attached mass where the basic phenyl structure is the same and the vibrations are mostly unaffected. For a "molecular toolbox" this is useful since it shows how substituent mass effects energy flow in a phenyl group.

Five prominent ring stretching transitions are observed, ν_{CH} (~3070 cm^{-1}), ν_{CC} (~1580 cm^{-1}), δ_{CCH} (~1160 cm^{-1}), ν_{CCH} (~1000 cm^{-1}) and ν_{CCC} (~610 cm^{-1}), whose frequencies in H-Bz and in the aryl-halides are quite similar, along with three substituent-dependent transitions denoted $\nu^{i}_{C\text{-}X}$, i = 1-3, whose frequencies redshift with increasing halide mass. Unfortunately $\nu^{3}_{C\text{-}X}$, the lowest-frequency substituent-dependent transition, could not be studied in detail due to its proximity to the Raman laser line.

†Parts of this chapter are recreated from work previously published as: Pein, B. C.; Seong, N.-H.; Dlott, D. D., Vibrational Energy Relaxation of Liquid Aryl-Halides X-C_6H_5 (X = F, Cl, Br, I). *Journal of Physical Chemistry A* **2010**, *114*, 10500.

This chapter will investigate to what degree these molecules behave similarly or differently by comparing the dynamics of the individual corresponding vibrations in each liquid. Discussed in Chapter 1, this is referred to as the chemical physics approach. In subsequent comparisons of the VR and VC processes within the series of aryl-halides F-Bz, Cl-Bz, Br-Bz, I-Bz, increasing mass will be referred to, however this is not meant to imply that halide substitution cannot also affect these processes via size effects, symmetry lowering, and electronegativity. This chapter will look for processes whose rates increase or decrease monotonically with halide mass because such processes should be understandable in terms of general trends in the relationships between structure and vibrational dynamics. On the other hand, processes whose rates do not vary in this manner would most likely result from coincidental resonances or level crossings. If the differences among aryl-halides are dominated by coincidental resonances, then it does not make sense to try to interpret this data in terms of a general mass-dependent trend or to draw a general conclusion.

As discussed in Chapter 1, VR processes are frequently described in the context of the golden rule,[5] where the rate of energy flow depends on anharmonic coupling matrix elements and the density of states (DOS). Within this framework these aryl halides present an interesting conundrum. With an initial parent CH-stretch excitation near 3070 cm^{-1}, one expects the DOS to increase with increasing halide mass, but opposing this effect would be the expectation that the anharmonic coupling between a CH-stretch and the rest of the molecule would decrease with increasing halide mass. Such an effect was seen in previous experiments as discussed below. It could be worthwhile to see how these factors interact to determine energy flow from the CH-stretch. Additionally, it is thought that anharmonic coupling exponentially weakens with increased quantum number difference between coupled states.[6] For example, a CH-stretch state

with a single quanta coupling to a CH-bend with two quanta represents two states with a quantum number difference of 3. The DOS can thusly be broken up into different tiers of states[7-11] where each tier indicates the number of quanta the states contain. It will be interesting to see how the DOS in lower tiers is affected by halide mass and how this relates to energy flow from the parent CH-stretch. One would expect faster CH-Stretch VR rates for molecules with larger DOS in lower tiers.

In prior related works, Bakker and coworkers[12,13] used one-color IR pump-probe measurements to compare CH-stretch excitations of dilute solutions of chloroform, bromoform and iodoform in CCl_4 or deuteroacetone solvents. Normally the one-color IR technique reports only the decay of the parent CH-stretch, but they were also able to observe transients in the parent transition that could be attributed to the influence of the daughter CH-bend as well. These transients provide a crude estimate of the overall VC lifetimes. As the halide mass was increased from Cl to I, the CH-stretch VR lifetimes increased significantly, by about a factor of three, and the overall time constant for VC also increased by about a factor of three.[12] A solvent effect was also noted. The lifetimes in CCl_4 were significantly longer than in deuteroacetone.[13]

In interpreting results in this chapter, it will be useful to keep in mind what was previously observed in H-Bz, where the ν_{CH} was pumped and the same five prominent ring modes studied here were monitored, along with one other mode, δ_{OOP}(CH).[3] Pumping H-Bz with an IR pulse centered at 3063 cm^{-1} with FWHM of 40 cm^{-1} resulted in instantaneous excitation of the parent ν_{CH} as well as ν_{CC}, ν_{CCH} and ν_{CCC}, where instantaneous denotes occurring during the ~1 ps pulse duration. This instantaneous ~1 ps excitation is indicative of coherent coupling among those excitations. As a reminder, coherent means the energy redistribution occurs on a time scale comparable to or faster than the dephasing time constant T_2.[3,14] After

excitation, the parent CH-stretch decayed with a T_1 = 6.2 ps lifetime, and a 6.2 ps transient was observed in the rising edges of δ_{CCH}, ν_{CCH} and ν_{CCC} but not ν_{CC}.[3] Thus the rising edge of ν_{CC} had only the 1 ps component, but the rising edges of ν_{CCH} and ν_{CCC} had both 1 ps and 6.2 ps components. Some lower-energy H-Bz daughter vibrations had lifetimes in the 55-125 ps range. The VC process resulting from the multiple VR steps had a nonexponential time dependence with a half-life of ~ 30 ps. The IR-pumped H-Bz appeared to have been thermalized by ~100 ps.

Being in the liquid phase both inter- and intramolecular interactions are present and must be considered. According to previous work by Stewart and McDonald[15], isolated-molecule CH-stretch relaxation of benzene and fluorobenzene is negligible on the microsecond time scale, so the picosecond time scale relaxations observed here in liquid F-Bz is entirely a consequence of intermolecular interactions, and presumably this is also true for Cl-Bz, Br-Bz and I-Bz. Distinguishing intramolecular VR (IVR) versus intermolecular VR processes will not be of any focus here however there are some previous results to keep in mind. In the previous IR-Raman study on H-Bz and perdeuterobenzene[3] it was found that energy flow was primarily from IVR prior to ~5 ps. Since the underlying structure and spectrum isn't drastically perturbed, as will be seen, it would seem logical to associate VR processes that occur prior to ~5 ps as intramolecular.

4.2 Results

IR and Raman Spectra and Assignments

The aryl-halide Stokes Raman spectra and the IR spectra in the ν_{CH} region are shown in Figures 4.1 and 4.2. Here the substituent-dependent modes $\nu^1_{C\text{-}X}$ and $\nu^2_{C\text{-}X}$ redshift with increasing mass. The five phenyl modes ν_{CH} (~3070 cm^{-1}), ν_{CC} (~1580 cm^{-1}), δ_{CCH} (~1160 cm^{-1}), ν_{CCH} (~1000 cm^{-1}) and δ_{CCC} (~610 cm^{-1}) exhibit a reasonably close correspondence to H-Bz modes ν_1 (3063 cm^{-1}), ν_{16} (1589 cm^{-1}), ν_{17} (1176 cm^{-1}), ν_2 (992 cm^{-1}) and ν_{18} (606 cm^{-1}).

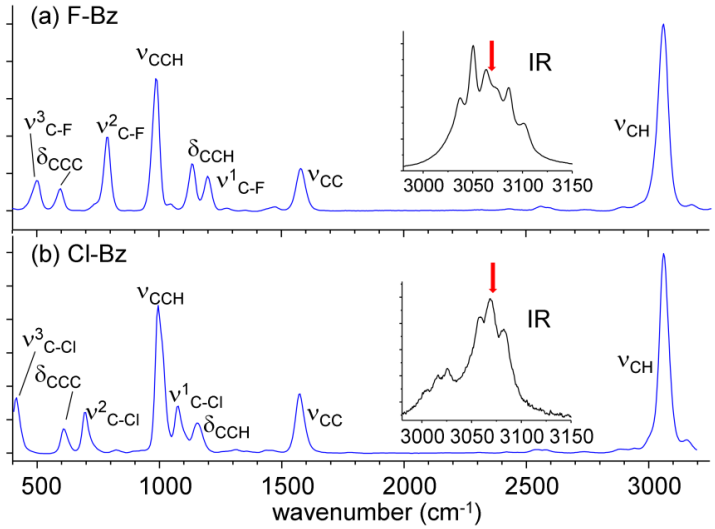

Figure 4.1. IR and Raman spectra of fluorobenzene and chlorobenzene. The Stokes spectra for (a) fluorbenzene (F-BZ) and (b) chlorobenzen (Cl-Bz) at ambient temperature. The *insets* show IR spectra in the region of ν_{CH} and the arrows indicate the 3068 cm^{-1} central wavenumber of the IR pump pulses.

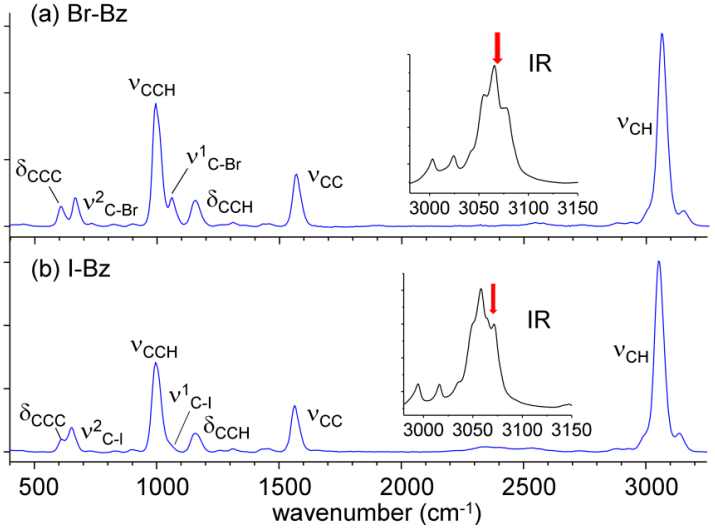

Figure 4.2. IR and Raman spectra of bromobenzene and iodobenzene. The Stokes spectra for (a) bromobenzene (Br-BZ) and (b) iodobenzene (I-Bz) at ambient temperature. The *insets* show IR spectra in the region of ν_{CH} and the arrows indicate the 3068 cm^{-1} central wavenumber of the IR pump pulses.

In the IR CH-stretch region, the spectra have multiple overlapping peaks. The Raman spectra in the CH-stretch region of all the aryl-halides consist primarily of a single intense peak similar to ν_1 of H-Bz centered at 3068-3075 cm^{-1}, so in these experiments the IR pump pulses were tuned to 3068 cm^{-1} for all four aryl-halides. In this way corresponding transitions were pumped in each aryl-halide and the same amount of energy was deposited into each species.

Tuning the IR pump pulses a few wavenumbers within the pumped band in the vicinity of 3068 cm^{-1} appeared to change only in minor ways the relative intensities of the time-dependent anti-Stokes intensities.

Densities of States

The DOS calculations were performed using the Beyer-Swinhart method, which utilizes a counting algorithm to generate a list of states consisting of single and multiple quanta excitations from an input array of the fundamental excitation energies of F-Bz[16], Cl-Bz[17], Br-Bz[18] or I-Bz.[19] The algorithm then sorts the generated states according to energy. For the calculations, a typical assumption of 5% anharmonicity was used. To smooth the DOS data, the results were averaged using 100 cm^{-1} width bins. The FORTRAN script for these calculations can be found in the appendix accompanying this thesis.

total states from 3000-3200 cm^{-1}	F-Bz	Cl-Bz	Br-Bz	I-Bz
Total DOS	10328	19185	30052	43312
N = 1	5	5	5	5
N = 2	12	10	8	8
N = 3	478	462	442	434
N = 4	1938	2048	2117	2131
ΣN = 1-4	2433	2525	2572	2578

Table 4.1. Densities of states in CH-stretch region of aryl-halides. The total DOS (top) are summed over all tiers of states. The separate tier values are shown as N =1, 2, 3 and 4. The sum of tiers 1-4 is shown at the bottom.

DOS for successive tiers of vibrational states were computed, where the first tier consists of fundamental vibrations with a single quanta, the second tier combinations and overtones with two quanta of excitation and so on. The differences among the aryl-halides stem primarily from the mass-dependent redshifts of the substituent-dependent modes $\nu^{i}_{C\text{-}X}$. In Table 4.1 the density of states near the pump wavenumber for the first four tiers are listed. Figure 4.3a shows the

combined energy-dependent DOS for the first four tiers only, computed by summing tiers with up to four quanta of excitation.

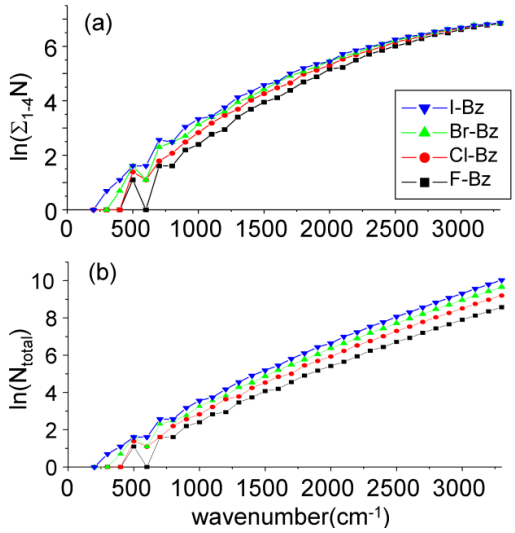

Figure 4.3. Computed densities of states for aryl-halides. (a) Lower-tier DOS of states having 1-4 quanta of excitation (four-tier DOS). (b) Total DOS of states having any number of excitations. A 5% anharmonicity was used in these calculations.

The use of four tiers is arbitrary and is meant simply to illustrate the considerable differences between lower and higher tiers. Figure 4.3b shows the combined total DOS for all tiers. In the lower-energy regions, say <1600 cm^{-1}, these two DOS are quite similar with the DOS increasing with increasing aryl-halide mass. But in the higher-energy region, especially in the CH-stretch region near 3070 cm^{-1}, Table 4.1 shows that the DOS for Tier 1 is identical for all aryl-halides, and in fact the DOS for Tiers 1-3 are practically identical. It is only in Tier 4 and above that significant differences among the aryl-halides emerge. Thus Figure 4.3 shows that the four-tier DOS is almost identical for all aryl-halides whereas the total DOS is quite different. The total DOS for I-Bz is about a factor of five larger than for F-Bz in the CH-stretching region. The reasons for the differences between the higher-frequency four-tier and total DOS in Figures 4.3a and 4.3b are the contributions from higher overtones of substituent-dependent vibrations. As an

extreme example, the fundamental $\nu^3_{C\text{-}X}$ mode in I-Bz is at ~200 cm^{-1}, and its ~20th harmonic contributes to the higher-energy total DOS but not to the four-tier DOS.

Anti-Stokes Transients

The IR-Raman spectra, composed of the anti-Stokes difference spectra at each pump-probe delay, are shown in Figure 4.4. Note the nonlinear delay time axis that is expanded at shorter times and compressed at longer times.

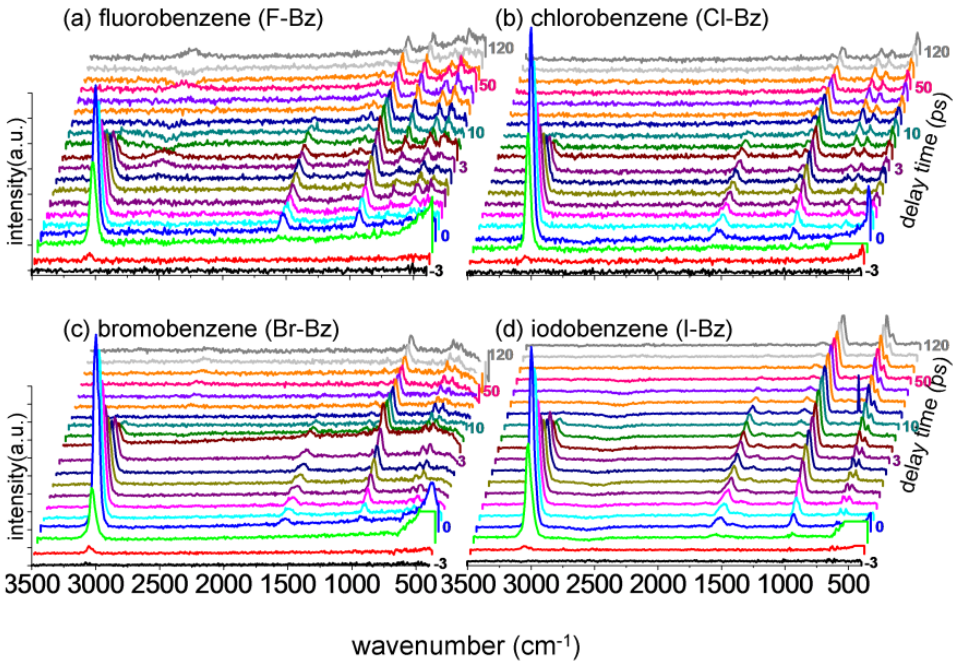

Figure 4.4. IR-Raman spectra of aryl-halides. Acquired following ν_{CH} pumping (3068 cm^{-1}). Note the nonlinear time axes. The broader features seen at the lowest wavenumber and occasionally in the 2500 cm^{-1} range are artifacts stemming from nonlinear interactions of the intense pump and probe pulses with the liquid media.

As a reminder, IR-Raman spectra have the ambient temperature intensities, obtained at -3 ps, subtracted away. At the lowest wavenumber near t = 0, and sometimes in the ~2500 cm^{-1} region, there are broader intensity artifacts which stem from a variety of nonlinear interactions between pump and probe pulses.[20,21] There may be narrower intensity artifacts[22,23] whose intensity

depends on the type of liquid, at the wavenumber of the pump laser. These artifacts are discussed in detail in Chapter 3.

Using the data in Figure 4.4, the instantaneous populations of seven vibrational transitions of the four aryl-halides were determined, as shown in Figures 4.5-4.11. The population transients of the lower wavenumber transitions do not decay back to zero, but instead to a plateau value due to the bulk T-jump ΔT.[24-27]

The population transients were normalized as follows. In Figure 4.5, for the parent ν_{CH} vibration, the quantity plotted is the instantaneous occupation number, or population, derived from Stokes and anti-Stokes spectra. The peak value of the parent transient depends on the IR absorption coefficient and the laser condition on a given day. As shown in Figure 4.5 between 3% and 5% of the aryl-halide molecules are being excited. In Figures 4.6-4.11, which display transients for daughter vibrations, the populations were normalized to the initial parent ν_{CH} population. With this normalization, the quantity plotted in Figures 4.6-4.11 is the quantum yield of daughter generation from the parent excitation.

Parent ν_{CH}

Figure 4.5 shows the parent ν_{CH} pumped by IR pulses. The parent signals always rise instantaneously. The *inset* shows semilog plots of the data. Around $t = 0$ there is a small contribution from nonlinear light scattering[21,22,28,29] whose intensity depends on the alkyl-halide. This shorter-time contribution, if not noticed, can cause the lifetime to be underestimated.[30] The lifetimes of the ν_{CH} excitations using data from times >3 ps were 2.5, 2.7, 2.8 and 3.4 ps (estimated error ±0.1 ps) for F, Cl, Br and I respectively. Therefore T_1 increases slightly and monotonically with increasing halide mass and is noticeably shorter than the 6.2 ps value[3] for H-Bz.

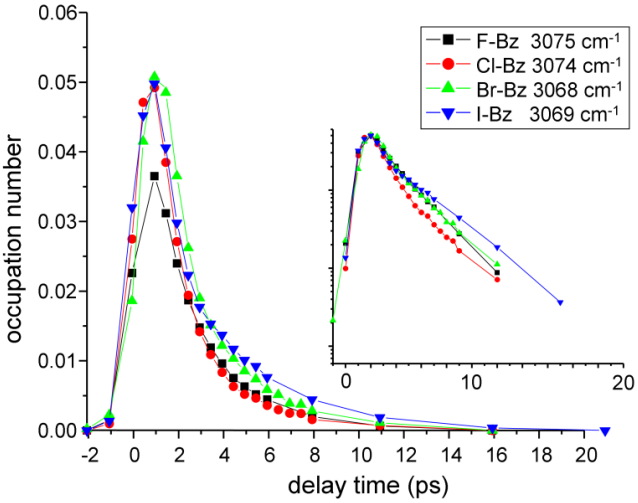

Figure 4.5.Time-dependent vibrational populations of parent ν_{CH} transitions. As shown in the *inset* there is a small contribution from a coherence artifact near $t = 0$.

Ring Stretch ν_{CC} (~1580 cm^{-1})

The ν_{CC} ring stretch (~1580 cm^{-1}) data are shown in Figure 4.6. All the transients evidence an instantaneous rise. The Br-Bz and I-Bz also have a slower component in the rise not observed in F-Bz or Cl-Bz which shifts the peak from ~+1 ps to longer time. For instance the I-Bz data peaks at ~3.5 ps. The lifetimes were 7.3, 6.2, 6.3 and 11.2 ps, with an estimated error of (±0.2 ps) for F-Bz, Cl-Bz, Br-Bz and I-Bz respectively, compared to the 20 ps lifetime of H-Bz.[3]

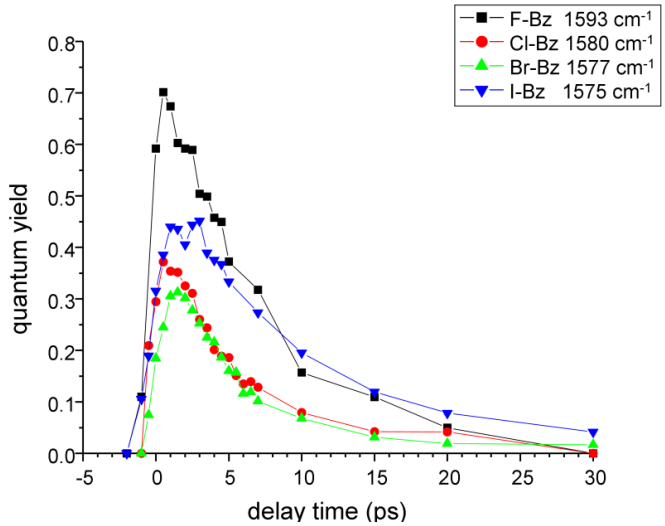

Figure 4.6. Time-dependent quantum yields of ν_{CC} vibrations. These yields resulted from IR pumping of ν_{CH}.

Asymmetric Ring Bend δ_{CCH} (~1160 cm^{-1})

The asymmetric ring bend δ_{CCH} has a smaller Raman cross-section, and in the case of F-Bz it overlaps one of the substituent-dependent vibrations, so the data in Figure 4.7 are noisier than in Figures 4.5 and 4.6. Looking at the inset to see the rising edge in more detail, only Cl-Bz has a prominent instantaneous rise, with the other transients rising more slowly so that the Cl-Bz transient peaks at ~5 ps while the F-Bz and Br-Bz transients peak at ~10-15 ps and the I-Bz transient peaks at ~20 ps. The δ_{CCH} lifetimes are longer than ν_{CH} or ν_{CC} lifetimes. Due to the noise and the plateau it is hard to get an accurate T_1, but it is estimated that T_1 is similar for all four aryl halides, and in the 30-50 ps range. This estimate can be compared to the measured value of 150 ps for H-Bz.[3]

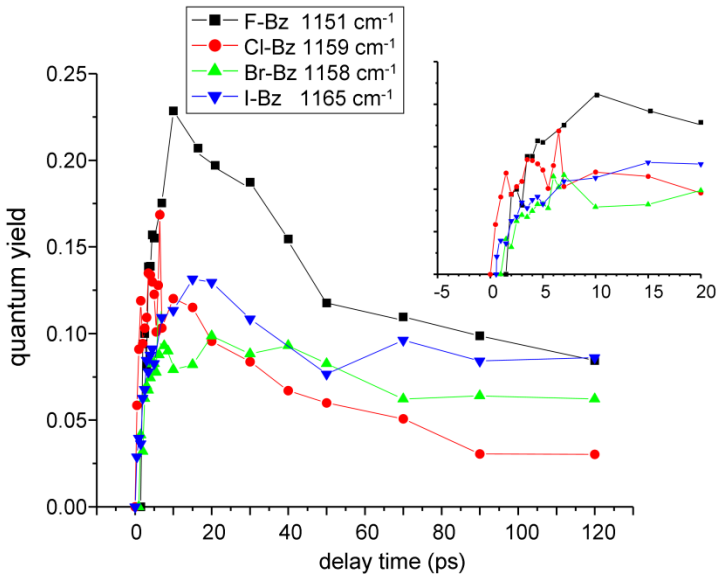

Figure 4.7. Time-dependent quantum yields of δ_{CCH} vibrations. These yields resulted from IR pumping of ν_{CH}. The *inset* shows the shorter-time yields on an expanded scale.

Symmetric Ring CCH Stretch ν_{CCH} (~1000 cm^{-1})

The symmetric ring stretch ν_{CCH} transients in Figure 4.8 have rising edges that show an instantaneous and also a slower component that results in a peak at 4-5 ps, except for I-Bz which has a flat region extending out to 25 ps. The lifetimes are similar for the four aryl-halides and can be estimated to be 30-40 ps. These estimates can be compared to the measured value of 55 ps for H-Bz.[3]

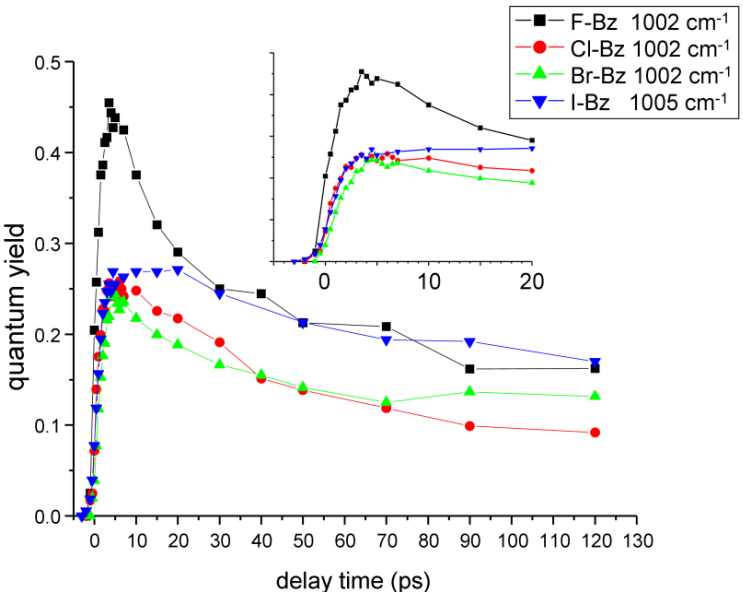

Figure 4.8. Time-dependent quantum yields of ν_{CCH} vibrations. These yields resulted from IR pumping of ν_{CH}. The *inset* shows the shorter-time yields on an expanded scale.

In-Plane Deformation Mode ν_{CCC} (~610 cm^{-1})

The ν_{CCC} transients shown in Figure 4.9 are noisy. The *inset* shows that the rise contains some of the instantaneous component and some of the slower ~3 ps component that causes the F-Bz, Cl-Bz and Br-Bz transients to peak at ~5 ps. The I-Bz data has a smaller-amplitude slower component in its rise that causes it to peak at ~50 ps.

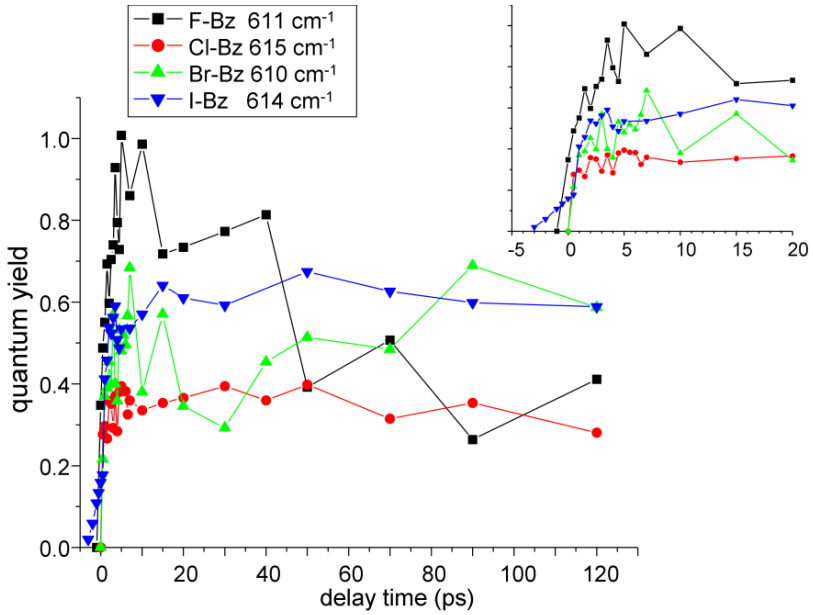

Figure 4.9. Time-dependent quantum yields of ν_{CCC} vibrations. These yields resulted from IR pumping of ν_{CH}. The *inset* shows the shorter-time yields on an expanded scale.

Substituent-Dependent Mode $\nu^1_{C\text{-}X}$

In the $\nu^1_{C\text{-}X}$ transients shown in Figure 4.10, the F-Bz, Cl-Bz and Br-Bz data have an instantaneous rise component and also a bit of the slower component that causes the data to peak in the 4-5 ps time range. The I-Bz data have a strange feature. The signal does not start to rise until about 5 ps. This is due to experimental error caused by a lower-wavenumber SPM artifact leading to poor baseline subtraction. Regardless of its initial rise, the I-Bz transient peaks at a later delay time than the others. The $\nu^1_{C\text{-}X}$ lifetimes can be estimated to be in the 40-50 ps range.

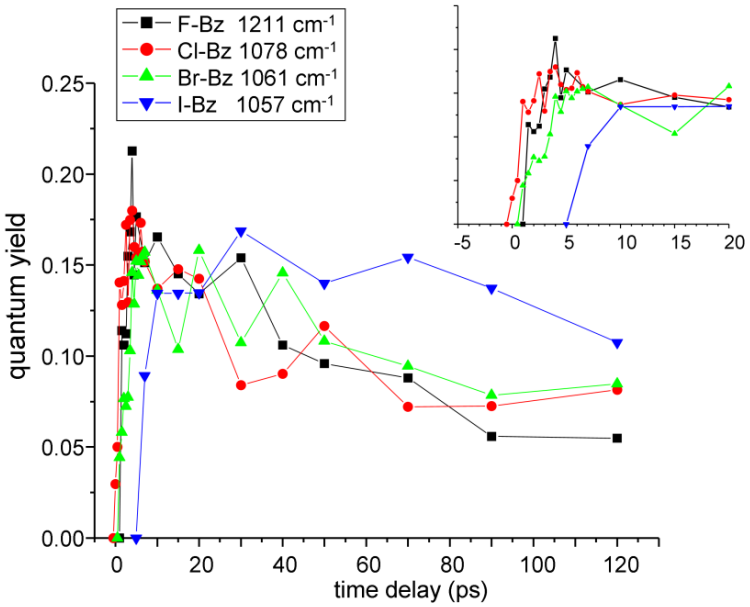

Figure 4.10. Time-dependent quantum yields of substituent-dependent $\nu^1_{C\text{-}X}$ vibrations. These yields resulted from IR pumping of ν_{CH}. The *inset* shows the shorter-time yields on an expanded scale.

Substituent-Dependent Mode $\nu^2_{C\text{-}X}$

The substituent-dependent $\nu^2_{C\text{-}X}$ mode transients in Figure 4.11 evidence no instantaneous component in the rising edges. With F-Bz and Cl-Bz there are slower rises to peaks in the 10-20 ps range. The I-Bz and Br-Bz transients have a slower-rise component leading to peaks at ~40 ps. The I-Bz transient has another strange feature (Figure 4.11, *inset*), a small signal at negative delay times which is believed to be a result of experimental artifacts leading to poor baseline subtraction. The lifetimes of these transients cannot be estimated due to the presence of the relatively large amplitude longer-time plateau that is characteristic of lower-wavenumber transients.

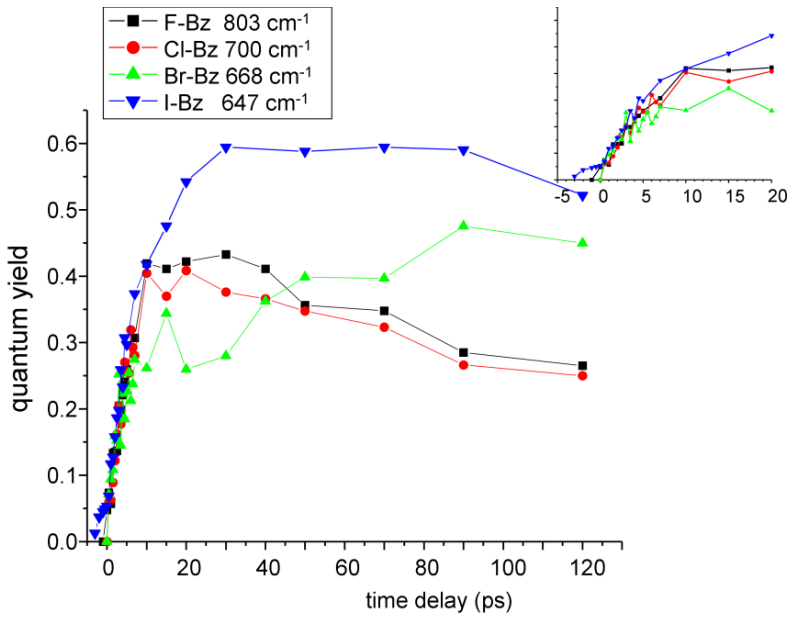

Figure 4.11. Time-dependent quantum yields of substituent-dependent $\nu^2_{C\text{-}X}$ vibrations. These yields resulted from IR pumping of ν_{CH}. The *inset* shows the shorter-time yields on an expanded scale.

4.3 Discussion

The aryl-halides are complicated molecules with 30 normal modes. With limited signal-to-noise ratios and the observation of only 10 of these modes (ν_{CC}, δ_{CCH} and ν_{CCC} are doubly-degenerate), it does not make sense to try to create a complete description of the VR pathways and VC mechanism as was done before on smaller molecules where almost all of the vibrations are observable.[31] As mentioned in Chapter 3, a useful method of analyzing the type of data obtained here is to look at the time constants appearing in the rising edges of the transients and comparing them to the decay lifetimes of higher-energy states to determine which VR processes were responsible for the observed rise.[32] In particular the rising edges will be looked at to determine the amplitudes of the instantaneous (1 ps) component, the ~3 ps parent ν_{CH} decay, the 6-11 ps ν_{CC} decay and the longer-lived 30-50 ps states such as ν_{CCH} and δ_{CCH}. In addition the results will be compared and discussed in the context of prior results[3] for H-Bz.

One notable observation is that the ν_{CH} VR rates decrease monotonically with increasing halide mass. In contrast, the VR rates and quantum yields for $\nu_{CH} \rightarrow \nu_{CC}$ processes do not share this monotonic behavior. The VR rates for ν_{CC} instead decrease in the order Cl, Br, F, I, and the peak quantum yields from Figure 4.6 decrease in the order F, I, Cl, Br.

The aryl-halide quantum yields extracted from the transient data in Figures 4.5-4.11, and from a prior study[3] of H-Bz are summarized in Table 4.2. Even a quick look here shows that the VR of the four aryl-halides is overall quite similar, which is interesting in light of Figure 4.3b, which shows how the total DOS can be strongly affected by halide mass. In the rest of this discussion the table entries where significant differences in VR can be observed among the aryl-halides will be the primary focus.

vibration	wavenumber cm^{-1}	liquid	instantaneous (~1.5 ps)	parent decay (~3 ps)	ν_{CC} (~10 ps)	ν_{CCH} or δ_{CCH} (~30 ps)
ν_{CH}						
	3063	H-Bz	1.0	0	N/A	N/A
	3075	F-Bz	1.0	0	0	0
	3074	Cl-Bz	1.0	0	0	0
	3068	Br-Bz	1.0	0	0	0
	3069	I-Bz	1.0	0	0	0
ν_{CC}						
	1589	H-Bz	1.65	0	N/A	N/A
	1593	F-Bz	0.7	0	0	0
	1580	Cl-Bz	0.37	0	0	0
	1577	Br-Bz	0.25	0.05	0	0
	1575	I-Bz	0.45	0.1	0	0
δ_{CCH}						
	1176	H-Bz	0	0.42	N/A	N/A
	1151	F-Bz	0	0.15	0.07	0
	1159	Cl-Bz	0.12	0.03	0.02	0
	1158	Br-Bz	0	0.1	0.02	0
	1165	I-Bz	0	0.1	0.05	0
ν_{CCH}						
	992	H-Bz	2.0	0.4	N/A	N/A
	1002	F-Bz	0.2	0.26	0	0
	1002	Cl-Bz	0.1	0.16	0	0
	1002	Br-Bz	0.1	0.15	0	0
	1005	I-Bz	0.1	0.18	0.08	0
ν_{CCC}						
	606	Bz	1.2	0.4	N/A	N/A
	611	F-Bz	0.6	0.26	0	0
	615	Cl-Bz	0.28	0.09	0	0
	610	Br-Bz	0.4	0.16	0	0
	614	I-Bz	0.4	0.13	0.1	0
$\nu^1_{C\text{-}X}$						
	----	H-Bz	N/A	N/A	N/A	N/A
	1211	F-Bz	0.12	0.05	0	0
	1078	Cl-Bz	0.15	0.03	0	0
	1061	Br-Bz	0.05	0.1	0	0
	1057	I-Bz	0	0.13	0.3	0
$\nu^2_{C\text{-}X}$						
	----	H-Bz	N/A	N/A	N/A	N/A
	803	F-Bz	0	0.42	0	0
	700	Cl-Bz	0	0.4	0	0
	668	Br-Bz	0	0.3	0.08	0.08
	647	I-Bz	0	0.35	0.2	0.1

Table 4.2. Aryl-halide quantum yields for different components of the population rises. The yields are sorted by vibration in each of the aryl-halides and H-Bz and the lifetime associated with the rise.

The features of Table 4.2 that appear exceptional are summarized:

1. The rise of ν_{CC} (~1580 cm^{-1}) has an instantaneous part for all aryl-halides and for H-Bz, but in Br-Bz and I-Bz there is an additional 3 ps rise component attributed to $\nu_{CH} \rightarrow \nu_{CC}$.

2. In the rise of midrange vibrations ν_{CCH} (~1000 cm^{-1}), ν_{CCC} (~610 cm^{-1}) and $\nu^1_{C\text{-}X}$, only I-Bz has a slower (~10 ps) rise component. This slower component is attributed to the processes $\nu_{CC} \rightarrow \nu_{CCH}$, $\nu_{CC} \rightarrow \nu_{CCC}$ or $\nu_{CC} \rightarrow \nu^1_{C\text{-}X}$, which do not occur to any significant extent in H-Bz, F-Bz, Cl-Bz or Br-Bz.

3. In the rise of $\nu^2_{C\text{-}X}$ (647-803 cm^{-1}) both Br-Bz and I-Bz have slower (~10 ps and ~30 ps) rise components not observed in the other aryl-halides. These slower components are attributed to $\nu_{CC} \rightarrow \nu^2_{C\text{-}X}$ (~10 ps) and $\delta_{CCH} \rightarrow \nu^2_{C\text{-}X}$ (~30 ps) which do not occur in F-Bz or Cl-Bz.

4. In the rise of δ_{CCH} (~1160 cm^{-1}), there is an instantaneous component in Cl-Bz but not in any other aryl-halide.

The first observation above results from an enhancement in the rate of the $\nu_{CH} \rightarrow \nu_{CC}$ process in Br-Bz and I-Bz. The second observation results from an enhancement in the rates of $\nu_{CC} \rightarrow \nu_{CCH}$, $\nu_{CC} \rightarrow \nu_{CCC}$ or $\nu_{CC} \rightarrow \nu^1_{C\text{-}X}$ processes in I-Bz. The third observation results from an enhancement in the rate of $\nu_{CC} \rightarrow \nu^2_{C\text{-}X}$ (~10 ps) and $\delta_{CCH} \rightarrow \nu^1_{C\text{-}X}$ (~30 ps) in Br-Bz and I-Bz. Since the first three observations result from processes that are not seen to any significant extent with F-Bz and Cl-Bz, but which are enhanced in Br-Bz and I-Bz (processes 1 and 3) or only in I-Bz (process 2), it seems reasonable to think of them as processes whose rates increase with increasing substituent mass, although due to the inability to observe these processes in F-Bz or Cl-Bz it cannot be said that the rate increase is "monotonic". In any case the first three

observations listed are logically associated with the increase in DOS with increasing substituent mass.

Observation 4 clearly does not represent a mass-dependent trend since only Cl-Bz evidences the instantaneous rise of δ_{CCH}. For this reason, specific effects resulting from accidental resonances should be searched for. The vibrational spectra of the aryl halides were reexamined, and in Figure 4.12 the IR spectra in the 1120-1250 cm^{-1} range is shown. It is clear that Cl-Bz evidences an anomalous broadening in the 1160-1210 cm^{-1} range. This broadening is suggestive of interactions due to Fermi resonances not present in the other aryl-halides, which evidently leads to enhanced coherent coupling with the parent ν_{CH} vibration in Cl-Bz.

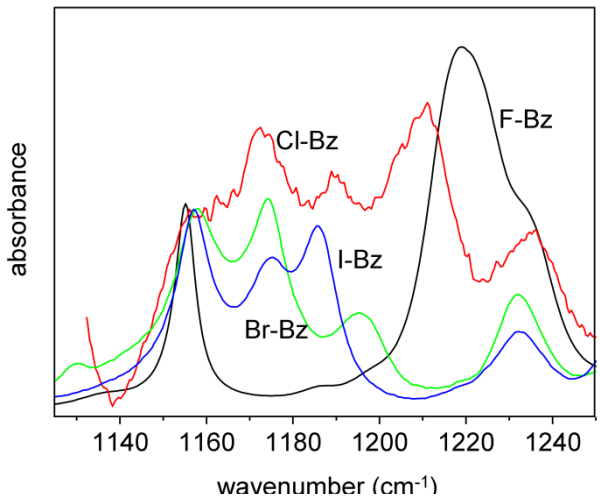

Figure 4.12. Mid-IR spectra of aryl-halides. Comparing the IR spectra in the 1120-1250 cm^{-1} range of the 4 liquids, Cl-Bz shows anomalous broadening not seen in the other species.

4.4 Conclusions

IR-Raman spectroscopy was used to study vibrational relaxation after ν_{CH} pumping at 3068 cm^{-1}, of four ambient temperature liquid aryl-halides. Vibrational energy dynamics of five transitions primarily associated with the phenyl ring could be measured, that are similar enough in the four aryl-halides to permit direct comparisons of corresponding vibrations. Two of the

three vibrations which have substantial substituent-dependent frequency shifts could also be observed. The data were understood primarily by looking at the various time constants in the rising edges of the anti-Stokes transients, and relating them to decay lifetimes of higher-energy vibrations. Generally speaking, the aryl-halide VR lifetimes were shorter than H-Bz lifetimes. For instance the ν_{CH} and ν_{CC} lifetimes in H-Bz were 6.2 ps and 20 ps while the corresponding values in aryl-halides ranged from 2.5-3.4 ps for ν_{CH} and from 6.2-11.2 ps for ν_{CC}.

The overall VR and VC processes in the aryl halides were strikingly similar in light of the large differences in total DOS seen in Figure 4.3b. But after a close inspection four significant differences listed in the section above were highlighted, based on the quantum yield data in Table 4.2. Three of those differences resulted from VR channels that were more efficient in Br-Bz and I-Bz (or I-Bz alone) which were not seen in F-Bz or Cl-Bz. These appear to be examples of general trends related to the effects of molecular structure on VR rates. The fourth observation involved coherent coupling of δ_{CCH} of Cl-Bz with the pumped parent ν_{CH} that was not observed in the other compounds, and this observation resulted from a specific interaction caused by coincidental resonances.

The most interesting observations that resulted from the comparison of aryl-halides were that the VR rates for ν_{CH} *decreased* with increasing mass whereas the first three observations above were explained by an *increase* in the VR rates out of midrange vibrations ν_{CC} (~1580 cm^{-1}) and δ_{CCH} (~1060 cm^{-1}), or to midrange vibrations via $\nu_{CH} \rightarrow \nu_{CC}$. These countervailing effects can be rationalized on the basis of the four-tier DOS in Figure 4.3a, but are entirely incompatible with the total DOS in Figure 4.3b. No special meaning is ascribed to the use of four tiers; that value was chosen simply as a useful way of communicating the differences between lower-tier and all-tier effects. The lower-tier DOS shows there are only minor differences in the DOS in

the CH-stretch region, but in the midrange region the DOS increases with halide mass. So in general the comparison of VR rates among the aryl-halides supports the idea that the first few tiers of the DOS are the most important.

Regarding the monotonic decrease of VR rates of CH-stretch excitations with increasing mass, since the lower-tier DOS for these processes are similar, it is logical to ascribe this observation to a monotonic mass-dependent decrease in anharmonic coupling. Since the reduced mass of CH-stretch oscillators is so small, the heavier halides create a mass mismatch on one carbon site that slightly hinders the overall VR of CH-stretch excitations.

The increase in midrange vibration relaxation in the heavier aryl-halides has implications for the overall VC process. Even though the initial state decay is slower in the heavier species, it is the decay of midrange vibrations, which are usually the longest-lived vibrations that generally control VC.[1,2] For controlling vibrational energy flow for molecular-scale devices, this demonstrates possible routes for more efficient energy dissipation from phenyl groups.

4.5 References

1. Hill, J. R.; Dlott, D. D., A Model for Ultrafast Vibrational Cooling in Molecular-Crystals. *Journal of Chemical Physics* **1988,** *89* (2), 830-841.

2. Hill, J. R.; Dlott, D. D., Theory of Vibrational Cooling in Molecular-Crystals - Application to Crystalline Naphthalene. *Journal of Chemical Physics* **1988,** *89* (2), 842-858.

3. Seong, N. H.; Fang, Y.; Dlott, D. D., Vibrational Energy Dynamics of Normal and Deuterated Liquid Benzene. *Journal of Physical Chemistry A* **2009,** *113* (8), 1445-52.

4. Iwaki, L. K.; Deak, J. C.; Rhea, S. T.; Dlott, D. D., Vibrational Energy Redistribution in Liquid Benzene. *Chemical Physics Letters* **1999,** *303* (1-2), 176-182.

5. Kenkre, V. M.; Tokmakoff, A.; Fayer, M. D., Theory of Vibrational-Relaxation of Polyatomic-Molecules in Liquids. *Journal of Chemical Physics* **1994,** *101* (12), 10618-10629.

6. Parmenter, C. S., Vibrational Redistribution within Excited Electronic States of Polyatomic-Molecules - the Spiers Memorial Lecture. *Faraday Discussions* **1983,** *75*, 7-22.

7. Bingemann, D.; King, A. M.; Crim, F. F., Transient Electronic Absorption of Vibrationally Excited Ch2i2: Watching Energy Flow in Solution. *Journal of Chemical Physics* **2000,** *113* (12), 5018-5025.

8. Cheatum, C. M.; Heckscher, M. M.; Bingemann, D.; Crim, F. F., Ch2i2 Fundamental Vibrational Relaxation in Solution Studied by Transient Electronic Absorption Spectroscopy. *Journal of Chemical Physics* **2001,** *115* (15), 7086-7093.

9. Heckscher, M. M.; Sheps, L.; Bingemann, D.; Crim, F. F., Relaxation of the C-H Stretching Fundamental Vibrations of Chi3, Ch2i2, and Ch3i in Solution. *Journal of Chemical Physics* **2002,** *117* (19), 8917-8925.

10. Elles, C. G.; Crim, F. F., Connecting Chemical Dynamics in Gases and Liquids. *Annual Review of Physical Chemistry* **2006,** *57*, 273-302.

11. Gruebele, M., Vibrational Energy Flow: A State Space Approach. *Advances in Chemical Physics, Vol 114* **2000,** *114*, 193-261.

12. Bakker, H. J.; Planken, P. C. M.; Kuipers, L.; Lagendijk, A., Ultrafast Infrared Saturation Spectroscopy of Chloroform, Bromoform, and Iodoform. *Journal of Chemical Physics* **1991,** *94* (3), 1730-1739.

13. Bakker, H. J.; Planken, P. C. M.; Lagendijk, A., Role of Solvent on Vibrational Energy Transfer in Solution. *Nature* **1990,** *347*, 745-747.

14. Deàk, J. C.; Iwaki, L. K.; Dlott, D. D., Vibrational Energy Redistribution in Polyatomic Liquids: Ultrafast Ir-Raman Spectroscopy of Nitromethane. *Journal of Physical Chemistry A* **1999,** *103*, 971-979.

15. Stewart, G. M.; McDonald, J. D., Intramolecular Vibrational Relaxation from C-H Stretch Fundamentals. *Journal of Chemical Physics* **1983,** *78*, 3907-3915.

16. Keefe, C. D.; MacDonald, J. L., Absolute Integrated Infrared Intensities of Liquid Fluorobenzene between 4000 and 400 Cm^{-1} at 25 Degrees C. *Vibrational Spectroscopy* **2006,** *40*, 168-176

17. Jain, Y. S.; Bist, H. D., The out-of-Plane Vibrational Modes of Chlorobenzene in Its Ground and First Singlet Excited States *Journal of Molecular Spectroscopy* **1976,** *47*, 126-133.

18. Keefe, C. D.; Donovan, L. A.; Fleet, S. D., Vibrational Assignment and Dipole Moment Derivatives of Liquid Bromobenzene at 25 Degrees C. *Journal of Physical Chemistry A* **1999,** *103*, 6420-6428

19. Keefe, C. D.; Butler, E.; Gillis, E.; MacDonald, J. L., Optical Constants, Dielectric Constants, Molar Absorption Coefficients, Molar Polarizability, Vibrational Assignment and Transition Moments of Liquid Iodobenzene between 4000 and 400cm^{-1} at 25 Degrees C *Spectrochimica Acta A* **2007,** *67*, 125-138

20. Deàk, J. C.; Iwaki, L. K.; Rhea, S. T.; Dlott, D. D., Ultrafast Infrared-Raman Studies of Vibrational Energy Redistribution in Polyatomic Liquids. *Journal of Raman Spectroscopy* **2000,** *31*, 263-274.

21. Deàk, J. C.; Rhea, S. T.; Iwaki, L. K.; Dlott, D. D., Vibrational Energy Relaxation and Vibrational Spectral Diffusion in Liquid Water and Deuterated Water. *Journal of Physical Chemistry A* **2000,** *104*, 4866-4875.

22. Wang, Z.; Pang, Y.; Dlott, D. D., Vibrational Energy Dynamics of Water Studied with Ultrafast Stokes and Anti-Stokes Raman Spectroscopy. *Chemical Physics Letters* **2004,** *397*, 40-45.

23. Wang, Z.; Pang, Y.; Dlott, D. D., Hydrogen-Bond Disruption by Vibrational Excitations in Water. *Journal of Physical Chemistry A* **2007,** *111*, 3196-3208.

24. Chen, S.; Hong, X.; Hill, J. R.; Dlott, D. D., Ultrafast Energy Transfer in High Explosives: Vibrational Cooling. *Journal of Physical Chemistry* **1995,** *99*, 4525-4530.

25. Chen, S.; Lee, I.-Y. S.; Tolbert, W.; Wen, X.; Dlott, D. D., Applications of Ultrafast Temperature Jump Spectroscopy to Condensed Phase Molecular Dynamics. *Journal of Physical Chemistry* **1992,** *96*, 7178-7186.

26. Chen, S.; Tolbert, W. A.; Dlott, D. D., Direct Measurement of Ultrafast Multiphonon up Pumping in High Explosives. *Journal of Physical Chemistry* **1994,** *98*, 7759-7766.

27. Hong, X.; Chen, S.; Dlott, D. D., Ultrafast Mode-Specific Intermolecular Vibrational Energy Transfer to Liquid Nitromethane. *Journal of Physical Chemistry* **1995,** *99*, 9102-9109.

28. Wang, Z.; Pang, Y.; Dlott, D. D., The Vibrational Stokes Shift of Water (Hod in D_2o). *Journal of Chemical Physics* **2004,** *120*, 8345-8348.

29. Wang, Z.; Pang, Y.; Dlott, D. D., Long-Lived Interfacial Vibrations of Water. *Journal of Physical Chemistry B* **2006,** *110*, 201150-20117.

30. Fendt, A.; Fischer, S. F.; Kaiser, W., Vibrational Lifetime and Fermi Resonance in Polyatomic Molecules. *Chemical Physics* **1981,** *57*, 55-64.

31. Shigeto, S.; Pang, Y.; Fang, Y.; Dlott, D. D., Vibrational Relaxation of Normal and Deuterated Liquid Nitromethane. *Journal of Physical Chemistry B* **2008,** *112*, 232-241.

32. Deàk, J. C.; Iwaki, L. K.; Dlott, D. D., Vibrational Energy Relaxation of Polyatomic Molecules in Liquids: Acetonitrile. *Journal of Physical Chemistry* **1998,** *102*, 8193-8201.

Chapter 5: Three-Dimensional IR-Raman and Excitation Spectroscopies

5.1 Introduction

Up till the aryl-halide study discussed in the previous chapter, in the IR-Raman experiments done by the Dlott laboratory[1-4] and others[5,6], the pump wavenumber dimension was never thoroughly exploited. In early IR-Raman works on ethanol[5] and methyl iodide[6] to name a few,[7,8] even though multiple CH-stretches could be pumped with the infrared (IR) pulses only a single pump wavenumber was used. In these studies it was asserted that the CH-stretches exchanged energy quickly leading to similar results for a range of IR pump wavenumbers. This general notion of pump-independent CH-stretch vibrational relaxation (VR) dynamics was later shown to be inaccurate when IR-Raman experiments pumped two different CH-stretches in methanol and monitored notably different results.[9] In the aryl-halide study, only a single pump wavenumber was used since slightly tuning it negligibly changed the daughter populations. However it cannot be presumed that other substituted benzenes would behave in a similar way, especially when the substituent has its own vibrations such as methyl CH-stretches, as the methanol study demonstrated.[9]

To extensively measure the effects of varying the pump in the IR-Raman experiments it would be desirable to collect several IR-Raman spectra using a broad and continuous range of *different* pump wavenumbers. Such a set of spectra, when stitched together, is known as a 3D IR-Raman spectrum where the 3 dimensions are pump wavenumber, probe wavenumber and pump-probe delay.[10] Recall, from Chapter 1, that these form a delay time series of 2D surfaces with pump and probe wavenumber dimensions. This would have been a valuable addition to the aryl-halide study however, since the laser apparatus used was in its earlier stages at the time,

performing such a series of experiments would have been a rather laborious task. Each IR-Raman spectrum using the older version of the apparatus required an extensive amount of time to optimize and collect, so acquiring several wasn't reasonable. The goal of this chapter is to introduce an updated version of the laser apparatus that allows 3D IR-Raman experiments as well as a novel type of spectroscopy for pumping energy into specific locations of molecules, excitation spectroscopy, to be performed. In Chapter 6, as a demonstration of the capabilities of the 3D IR-Raman technique, two liquids previously studied by the Dlott laboratory, acetonitrile and nitromethane,[3,4,11] will be investigated using the newer version of the apparatus. In Chapters 7-9, excitation spectroscopy will be used to study energy flow in nitrobenzene and substituted nitrobenzenes as well as a collection of alkylbenzenes.

5.2 Experimental Issues of 3D IR-Raman Spectroscopy

Recall that the IR pump pulses are generated via difference frequency generation. In a typical IR-Raman experiment, for each pumping wavenumber one has to tune the OPA to a new idler wavelength then phase-velocity match the idler pulses with 800 nm pulses in the KTA crystal. Each time the pump OPA is tuned to a new wavelength the Poynting vector of the idler slightly drifts. As shown below in Figure 5.1,

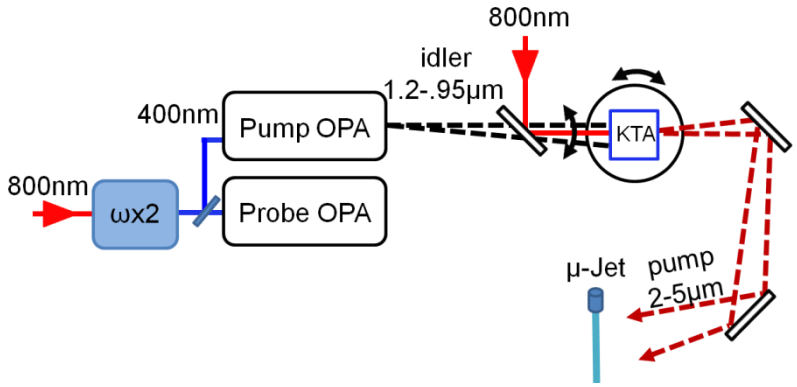

Figure 5.1. Diagram of pump Poynting vector drift. The idler pulses from the pump OPA slightly drift when being tuned. The pump pulses generated from the KTA also drift due to this.

after phase-velocity matching the pulses in the KTA crystal, the drift is transferred to the pump pulses. First of all, this means that tuning the pump wavenumber requires one to reestablish overlap of the pump and probe beams at the sample, a rather meticulous process. Additionally, the user has to manually input the positioning of the delay stage motor, through a rudimentary pc user interface, and acquire the Raman spectra with user commands at each delay which was time consuming. Combining these two requirements with sample evaporation rates and the global stability of the laser components throughout the day makes performing a 3D IR-Raman experiment difficult if not impractical.

5.3 A Solution Using Automation

To acquire 3D spectra the laser was retrofitted with an automated alignment and data collection system as shown in Figure 5.2.

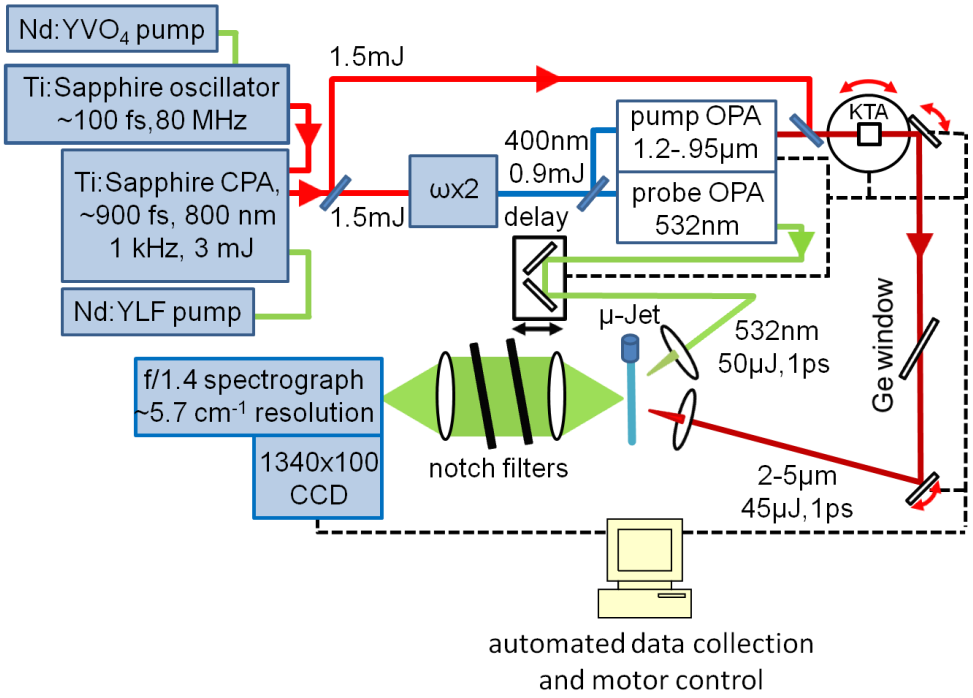

Figure 5.2. Diagram of retrofit IR-Raman laser apparatus. Motors were added to the mirrors after the KTA crystal and to the KTA crystal turret. The spectrograph, delay stage, motors and pump OPA are all linked to a central computer in this configuration. The LabVIEW software controls all of these elements to allow one to perform 3D IR-Raman experiments.

Linear motors were added to the mirrors after the KTA crystal and a rotation motor was added to the KTA crystal turret all of which were computer controlled. A script was created in LabVIEW to control the motors, the Aerotech pump-probe delay stage, the pump OPA tuning and the spectrograph data collection. In this newer version of the apparatus the user first generates a tuning curve for the KTA turret to assure optimal phase-velocity matching for each of the pump OPA's idler wavelengths. Next, a tuning curve for the mirrors is generated by placing a glass slide, coated with lithium niobate ($LiNbO_3$) powder suspended in poly(methyl methacryalate), in the sample jet plane. The $LiNbO_3$ generates an intense nonlinear light scattering signal from sum frequency generation when the pump and probe are spatially and temporally overlapped. Using this signal, a set of mirror motor positions are recorded for each pump wavenumber which are used for the mirror tuning curve. After KTA and mirror tuning curves are made the user can input a range of pump wavenumbers and a set of pump-probe delay times. Once initialized, the LabVIEW script begins with the first pump wavenumber and performs a single IR-Raman experiment after which the pump OPA, controlled by the script, is tuned to the next pump wavenumber while the motors respond with their calibrated values and the cycle begins again. Using this new apparatus, a 3D spectrum composed of $\geq$15 individual IR-Raman spectra (depending on the number of delays) could be obtained in a day with minimal user intervention.

5.4 Excitation Spectroscopy

In Chapter 4, VR is treated as energy flowing from an initial pumped parent, or bright state, to a background of states. This approach, the chemical physics approach, compares the VR processes of corresponding vibrations in a collection of molecules. As discussed in Chapter 1, the materials chemistry approach, which treats energy flow as nanoscale thermal conduction,[12] is also a viable description. In this picture, rather than focusing on energy in the individual

vibrations, energy is thought of as moving from location to location, say from the substituent to the phenyl moiety of a substituted benzene. The normal modes of a molecule can be computed, using quantum chemical calculations, and classified according to their atomic displacements. As shown in Figure 5.3, in nitrobenzene for example, the modes can be classified as (a) phenyl or (b) substituent if their atomic displacements are localized to the phenyl or substituent moieties respectively while if they are delocalized to both they can be classified as (c) global. In this way, the spatial localization (phenyl or subsituent modes) or delocalization (global modes) of energy contributed by a vibration can be determined. With these classifications, monitoring energy in and IR-Raman experiment is reduced from looking at each individual vibration to looking at where energy is located in the molecules at a given instant.

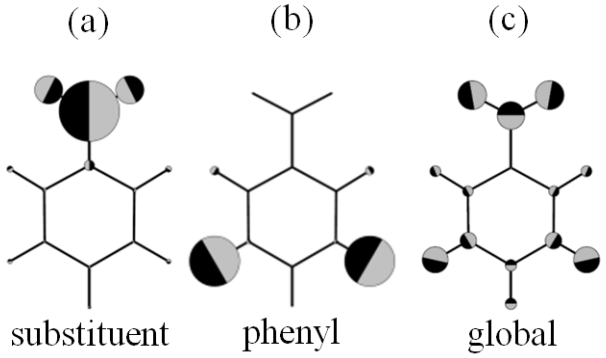

Figure 5.3. Illustrated examples of mode classes. (a) substituent (b) phenyl and (c) global modes of nitrobenzene. The spheres indicate the magnitude of the individual atomic displacements. The colors indicate the direction of the displacement.

Studying energy flow in this way requires a method to input, or localize, energy to a specific location which there are a few. One could fabricate a material where molecules are bound to a surface, like a metal or electrode, that can be flash-heated by a laser pulse.[13,14] Another possibility would be to pump energy into a specific location with submolecular resolution using scanning tunneling microscope tips and femtosecond IR pulses.[15] The 3D IR-Raman technique provides a way to do this also, through excitation spectroscopy, that involves

using the pump and probe laser pulses to create and probe localized vibrational excitations. Until recently, only the 3D IR-Raman technique had such a capability however there have been recent advances in two-color 2DIR methods[16,17] or relaxation-assisted 2DIR[18-21] that must be mentioned which permit such studies.

One could judge the initial localization of the vibrational energy that is pumped into a molecule based solely on the assignments and mode classifications of the IR transitions however in practice this is not possible. The bandwidth of the IR-pump pulses is larger than the natural line width of the IR transitions so multiple excited parent vibrations are inevitable. This issue is further augmented due to the enhanced sensitivity of the IR-Raman apparatus to pump weak IR transitions so combination bands and overtones that are not easily assignable in the IR spectrum are inevitably pumped. As the aryl-halide study showed, during the first few picoseconds after the pump pulses arrive, some of the daughter vibrations are excited by the parent either through coherent coupling or through intramolecular VR (IVR) processes. For the liquids studied here, there are typically 1-3 daughter vibrations that receive the vast majority of the initial energy burst from the parent. Along with the parent, these vibrations are a good indicator of the initial energy localization. Excitation spectroscopy is an excellent way to monitor these vibrations.

The excitation spectrum is a 2D projection of the total 3D IR-Raman spectrum at 1 ps pump probe delay. Using the 3D IR-Raman apparatus, the LabVIEW automation program scans the pump pulses through their tuning range, whilst optimizing the pump-probe overlap on the sample according to the mirror tuning curves. For each pump wavenumber, the program collects Raman spectra at 1 ps delay (and at -3 ps). Fitting these spectra, the population and energy density in the initially excited daughters can then be monitored as a function of the pump wavenumber. In this way, pump wavelengths that excite a desired classification of mode, say a

phenyl- or substituent-localized mode, can be found. Using the substituent- or phenyl-pump a normal IR-Raman experiment is carried out to monitor energy flowing from the initially localized excitation to the other end of the molecule.

5.5 References

1. Seong, N. H.; Fang, Y.; Dlott, D. D., Vibrational Energy Dynamics of Normal and Deuterated Liquid Benzene. *Journal of Physical Chemistry A* **2009,** *113* (8), 1445-1452.

2. Iwaki, L. K.; Deak, J. C.; Rhea, S. T.; Dlott, D. D., Vibrational Energy Redistribution in Liquid Benzene. *Chemical Physics Letters* **1999,** *303* (1-2), 176-182.

3. Deak, J. C.; Iwaki, L. K.; Dlott, D. D., Vibrational Energy Redistribution in Polyatomic Liquids: Ultrafast Ir-Raman Spectroscopy of Acetonitrile. *Journal of Physical Chemistry A* **1998,** *102* (42), 8193-8201.

4. Shigeto, S.; Pang, Y.; Fang, Y.; Dlott, D. D., Vibrational Relaxation of Normal and Deuterated Liquid Nitromethane. *Journal of Physical Chemistry B* **2008,** *112* (2), 232-241.

5. Lauberea.A; Kehl, G.; Kaiser, W., Picosecond Spectroscopy of Molecular Vibrations in Liquids - Vibrational Bottleneck in Ethanol. *Optics Communications* **1974,** *11* (1), 74-77.

6. Laubereau, A.; Kaiser, W., Vibrational Dynamics of Liquids and Solids Investigated by Picosecond Light-Pulses. *Reviews of Modern Physics* **1978,** *50* (3), 607-665.

7. Graener, H.; Laubereau, A., Ultrafast Vibrational-Energy Transfer of Polyethylene Investigated with Picosecond Laser-Pulses. *Chemical Physics Letters* **1987,** *133* (5), 378-380.

8. Seilmeier, A.; Kaiser, W., Ultrashort Intramolecular and Intermolecular Vibrational-Energy Transfer of Polyatomic-Molecules in Liquids. *Topics in Applied Physics* **1988,** *60*, 279-317.

9. Iwaki, L. K.; Dlott, D. D., Ultrafast Vibrational Energy Redistribution within C-H and O-H Stretching Modes of Liquid Methanol. *Chemical Physics Letters* **2000,** *321* (5-6), 419-425.

10. Iwaki, L. K.; Dlott, D. D., Three-Dimensional Spectroscopy of Vibrational Energy Relaxation in Liquid Methanol. *Journal of Physical Chemistry A* **2000,** *104* (40), 9101-9112.

11. Shigeto, S.; Pang, Y.; Fang, Y.; Dlott, D. D., 3-D Infrared-Raman Spectroscopy of Normal and Deuterated Nitromethane. *Abstracts of Papers of the American Chemical Society* **2007,** *233*.

12. Cahill, D. G.; Ford, W. K.; Goodson, K. E.; Mahan, G. D.; Majumdar, A.; Maris, H. J.; Merlin, R.; Sr, P., Nanoscale Thermal Transport. *Journal of Applied Physics* **2003,** *93* (2), 793-818.

13. Wang, Z. H.; Carter, J. A.; Lagutchev, A.; Koh, Y. K.; Seong, N. H.; Cahill, D. G.; Dlott, D. D., Ultrafast Flash Thermal Conductance of Molecular Chains. *Science* **2007,** *317* (5839), 787-790.

14. Carter, J. A.; Wang, Z. H.; Dlott, D. D., Ultrafast Nonlinear Coherent Vibrational Sum-Frequency Spectroscopy Methods to Study Thermal Conductance of Molecules at Interfaces. *Accounts of Chemical Research* **2009,** *42* (9), 1343-1351.

15. Xu, X. J. G.; Rang, M.; Craig, I. M.; Raschke, M. B., Pushing the Sample-Size Limit of Infrared Vibrational Nanospectroscopy: From Monolayer toward Single Molecule Sensitivity. *Journal of Physical Chemistry Letters* **2012,** *3* (13), 1836-1841.

16. Bian, H. T.; Zhao, W.; Zheng, J. R., Intermolecular Vibrational Energy Exchange Directly Probed with Ultrafast Two Dimensional Infrared Spectroscopy. *Journal of Chemical Physics* **2009,** *131* (12).

17. Chen, H. L.; Bian, H. T.; Li, J. B.; Wen, X. W.; Zheng, J. R., Ultrafast Multiple-Mode Multiple-Dimensional Vibrational Spectroscopy. *International Reviews in Physical Chemistry* **2012,** *31* (4), 469-565.

18. Kasyanenko, V. M.; Lin, Z. W.; Rubtsov, G. I.; Donahue, J. P.; Rubtsov, I. V., Energy Transport Via Coordination Bonds. *Journal of Chemical Physics* **2009,** *131* (15).

19. Kasyanenko, V. M.; Tesar, S. L.; Rubtsov, G. I.; Burin, A. L.; Rubtsov, I. V., Structure Dependent Energy Transport: Relaxation-Assisted 2dir Measurements and Theoretical Studies. *Journal of Physical Chemistry B* **2011,** *115* (38), 11063-11073.

20. Naraharisetty, S. R. G.; Kasyanenko, V. M.; Rubtsov, I. V., Bond Connectivity Measured Via Relaxation-Assisted Two-Dimensional Infrared Spectroscopy. *Journal of Chemical Physics* **2008,** *128* (10).

21. Rubtsov, I. V.; Naraharisetty, S. R. G.; Keating, C.; McClure, B. A.; Rack, J. J.; Kasyanenko, V. M., Relaxation-Assisted Dual-Frequency Two-Dimensional Infrared Spectroscopy: Measuring Distances and Bond Connectivity. *Ultrafast Phenomena Xvi* **2009,** *92*, 400-402.

Chapter 6: 3D IR-Raman Spectroscopy of Nitromethane and Acetonitrile†

6.1 Introduction

In this chapter 3D IR-Raman spectroscopy is applied to liquid nitromethane (NM) and acetonitrile (ACN) and their fully deuterated analogs d_3-NM and d_3-ACN in order to demonstrate the capabilities of the technique. NM, d_3-NM and ACN have been the subject of previous studies from the Dlott laboratory,[1-6] where vibrational relaxation (VR) pathways of each liquid were studied using two different pump wavenumbers. This chapter discusses the acquisition of complete 3D data sets on these liquids, along with the first results on d_3-ACN. Here the detailed VR pathways will not be the focus, although that information is clearly present in the 3D spectra. Instead the nature of 3D IR-Raman spectroscopy, and how the patterns evident in 3D spectra can be used to understand VR dynamics in these different liquids will be the primary focus.

In the liquids studied here, the parent excitations were in spectrally-congested regions where fundamental CH-stretches or CD-stretches lie on top of, and may be mixed with combinations and overtones of lower-energy modes. Understanding the mixture of excitations that comprise a parent state is possible because in IR-Raman and 3D IR-Raman spectroscopy, those excitations appear as excitations of the underlying fundamental transitions. This is the result of the $\Delta v = \pm 1$ selection rules of Raman scattering. As an example, in NM, the combination band excitation $\nu_a(NO_2) + \nu_s(NO_2)$ near 2950 cm^{-1} would appear at shorter delay times (t = 0,1 ps) as excitation of ~1562 cm^{-1} $\nu_a(NO_2)$ and ~1402 cm^{-1} $\nu_s(NO_2)$.[6] The anharmonic

†Parts of this chapter are recreated from work previously published as: Sun, Y.; Pein, B. C.; Dlott, D. D., Three-dimensional Spectroscopy of Vibrational energy in Liquids: Nitromethane and Acetonitrile. *Journal of Physical Chemistry B* **2013**, *117(49)*, 15444.

shifts associated with combination and overtone bands are generally not detectable because they are usually less than the probe laser bandwidth.

In the rest of this chapter, the IR and Raman spectra and vibrational assignments of the four liquids studied will first be described. Following this, the 3D IR-Raman spectra obtained will be discussed and examined.

6.2 3D IR-Raman Spectroscopy Signals

In chapter 4, VR was analyzed using the populations of the individual aryl-halide vibrations. As a reminder, the population of a vibration at frequency ω is proportional to $I_\omega^{AS}/I_\omega^{ST}$. However, it is difficult to express 3D spectra in this form because I_ω^{ST} is close to zero in broad regions between vibrational transitions. Rather, only the change in time-dependent anti-Stokes intensities $\Delta I_\omega^{AS}(t)$ is plotted, which as a reminder is equal to the anti-Stokes intensity at delay t with the ambient temperature background subtracted away. To help account for the I_ω^{ST} factors, reference Stokes spectra are drawn on top of each 3D spectrum.

Depending on the liquid, the bulk temperature jump (T-jump) ΔT created by an IR pulse is typically 10-40K in IR-Raman experiments. The liquids are mostly thermalized after ~10 ps, so the 3D data acquisition was stopped at 10 ps. However from previous studies by the Dlott laboratory it is known there may be small amounts of energy trapped in longer-lived excitations, and ACN or NM may not be fully thermalized until 100-200 ps.[3,4]

As discussed in Chapter 3, the magnitude of ΔT is

$$\Delta T = \frac{J\alpha}{C_v} \qquad (6.1)$$

where J is the IR laser fluence, α is the IR absorption coefficient and C_v the heat capacity. When a 3D spectrum was acquired, as the IR pulse was tuned through peaks and valleys of the

IR absorption spectrum, the IR absorption coefficient varied and ΔT varied accordingly so each pump wavenumber will have a different ΔT. In order to help account for this, a reference IR absorption profile is drawn in the lower-left corner of each 3D spectrum. One should keep in mind that the relationship of I_ω^{AS} to α and ΔT is complicated. Nominally I_ω^{AS} should increase exponentially with ΔT, but this increase is somewhat offset by the IR-Raman technique's enhanced sensitivity to weaker IR transitions. So the pump wavenumber dependence of I_ω^{AS} will be more gradual than suggested by the reference IR absorption profiles.

6.3 Results

IR and Raman Spectra and Assignments

Here the conventional IR and Raman spectra for each sample, accompanied by assignments, are discussed. Figures 6.1-6.4 show these spectra for NM and ACN. Figures 6.1-6.3 are adapted from prior Dlott laboratory publications,[3,6] and Figure 6.4 was newly collected. The spectral assignments for NM and d_3-NM,[7-12] and ACN and d_3-ACN[13,14] were taken from prior studies.

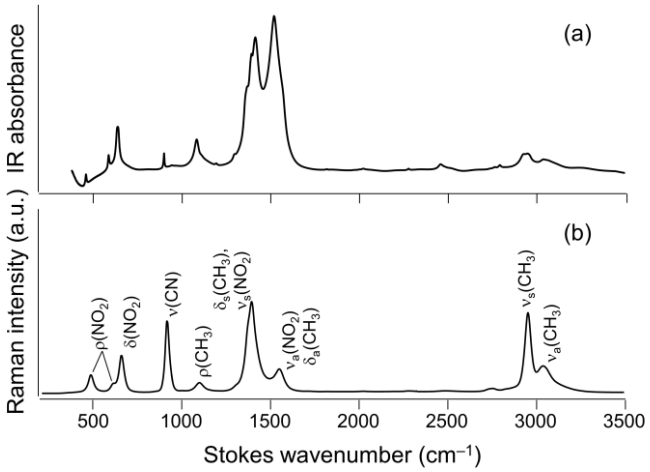

Figure 6.1. Infrared and Raman spectrum of nitromethane. The infrared spectrum (a) has a 4 cm^{-1} resolution. The Stokes spectrum (b), shown with assignments, was obtained using the picosecond probe laser. The resolution was 20 cm^{-1}. Adapted from ref. [6], copyright ACS.

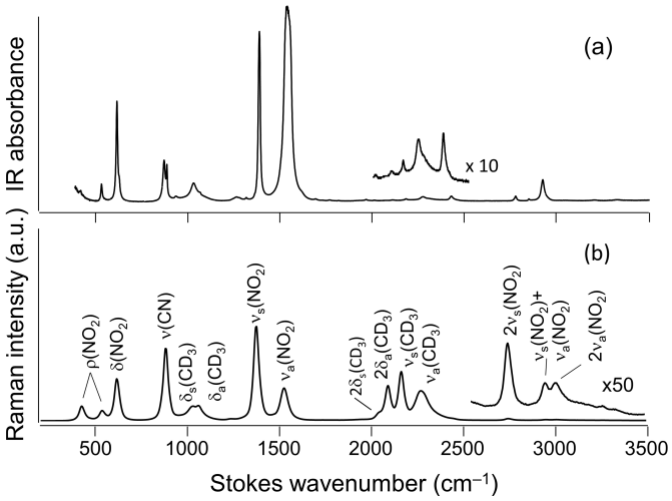

Figure 6.2. Infrared and Raman spectrum of d3-nitromethane. The infrared spectrum (a) has a 4 cm^{-1} resolution. The Stokes spectrum (b), shown with assignments, was obtained using the picosecond probe laser. Nitro-stretch overtones and combination bands could be seen in the ~3000 cm^{-1} region. The resolution was 20 cm^{-1}. Adapted from ref. [6], copyright ACS.

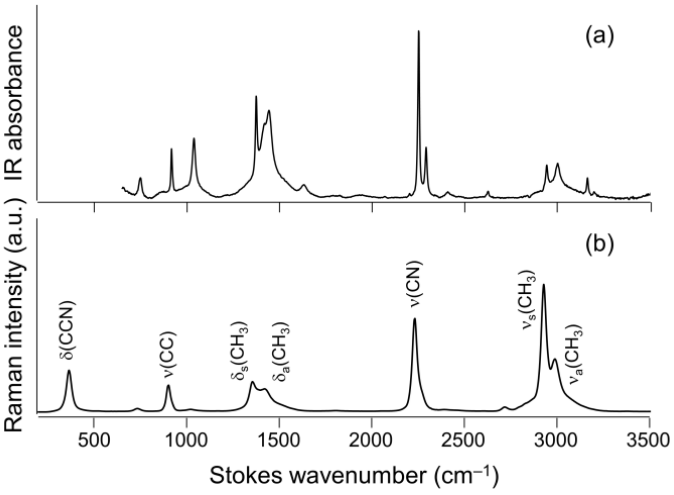

Figure 6.3. Infrared and Raman spectrum of acetonitrile. The infrared spectrum (a) has a 4 cm^{-1} resolution. The Stokes spectrum (b), shown with assignments, was obtained using the picosecond probe laser. The resolution was 20 cm^{-1}. Adapted from ref. [3], copyright ACS.

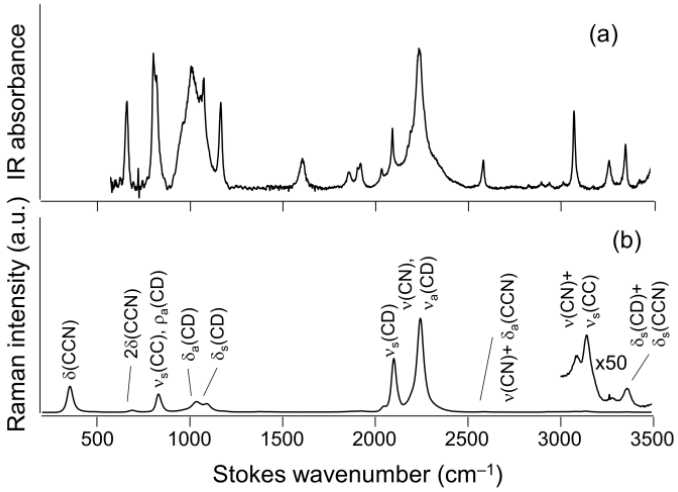

Figure 6.4. Infrared and Raman spectrum of d3-acetonitrile. The infrared spectrum (a) has a 4 cm^{-1} resolution. The Stokes spectrum (b), shown with assignments, was obtained using the picosecond probe laser. The resolution was 20 cm^{-1}. Above 2500 cm^{-1}, several overtones and combination bands could be observed, especially those involving ν(CN).

A few aspects of these spectra are worth mentioning. In the CH-stretch region (~2900 cm^{-1}) and the CD-stretch region (~2200 cm^{-1}), the NM spectra are more congested than the ACN spectra. For example, compare some of the sharper ACN IR absorption bands near 3000 cm^{-1} in Figure 6.3a and near 2200 cm^{-1} in Figure 6.4a to the corresponding broader NM bands in Figures 6.1a and 6.2a. In those regions spectral assignments are not simple, and even today not entirely conclusive. Nearby or directly underneath the CH-stretch and CD-stretch fundamentals are numerous overtones and combinations of the lower-energy modes. Ordinarily the IR absorption coefficients for these overtones and combinations would be small, but they can borrow intensity from the fundamental transitions. So pumping in this region with IR pulses does not create simple CH-stretch or CD-stretch excitations, but rather a mixture of them with lower-energy states. The most well-known example of this effect arises from the 2:1 Fermi resonance between CH-stretch and CH-bend (or CD-stretch and CD-bend), where, as observed in both NM[4,6] and ACN,[2,3] pumping the stretch transition promptly creates bend excitations as well. Another important factor is that in NM, the nitro-stretches near 1500 cm^{-1} are so close in energy to the

CH-bends that they are strongly mixed, and a CH-stretch/nitro-stretch 1:2 resonance is also possible.

With d_3-NM (Figure 6.2) the CD-bends are downshifted enough to become well-separated from the nitro-stretches, and also from the CN-stretch. However there is another kind of mixing. The CD-bends near 1100 cm^{-1} are resonant with the methyl rocking $\rho(CD_3)$, which was 1104 cm^{-1} in NM.

In ACN (Figure 6.3) there is a 2:1 Fermi resonance between $\nu_a(CH_3)$ and $2\delta_a(CH_3)$, but not between $\nu_s(CH_3)$ and $2\delta_s(CH_3)$.[3] As a result, the $\nu_a(CH_3)$ and $\delta_a(CH_3)$ transitions are noticeably broader than $\nu_s(CH_3)$ and $2\delta_s(CH_3)$. The same pattern is seen in d_3-ACN (Figure 6.4). In ACN the CN-stretch is an isolated excitation, but in d_3-ACN the CN-stretch is close to and strongly mixed with the CD-stretch $\nu_a(CD)$.

3D IR-Raman Spectra

The 3D anti-Stokes spectra are shown in Figures 6.5-6.8 of section 6.6 found at the end of this chapter. Since the intensities spanned a wide range, the intensity scale was made logarithmic, as indicated in the color guide in the upper right hand corner. The diagonals where the parent excitations and sum-frequency generation (SFG) nonlinear scattering artifacts (at $\omega_{probe} + \omega_{IR}$) appear are indicated by guide lines in the $t = 0$ spectra. A Stokes Raman spectrum with vibrational assignments runs along the top of each 3D spectrum. The Raman spectrum provides a reference for the wavenumber dependence of the Raman cross-section. An IR absorption spectrum runs along the left side of the 3D spectrum in the lowest panel. The IR spectrum provides a reference for ΔT dependence on pump wavenumber as discussed above. Recall that the 3D spectra are made up of several constituent IR-Raman spectra, each using different pump wavenumbers.

The 3D spectra were rectangular. The *x*-axis (anti-Stokes Raman wavenumber) range was fixed at 250-4000 cm^{-1}. The aspect ratio was between 3:1 and 5:1, depending on the selected IR wavenumber tuning range. The 3D spectra were quite complicated. Along the diagonal were two fundamental CH-stretch (or CD-stretch) transitions and several combination bands or overtone transitions. Because Raman spectroscopy allows one to simultaneously probe a wide wavenumber region, for every diagonal peak there were ~10 off-diagonal peaks. Note that in contrast to 2DIR spectra,[15] where there are $v = 1 \rightarrow 0$ transitions and $v = 0 \rightarrow 1$ transitions on either side of the diagonal, here using 3D IR-Raman where anti-Stokes Raman is used as the probe, only the $v = 1 \rightarrow 0$ transitions are detected.

6.4 Discussion

Due to the complexity of the 3D spectra in this study the discussion will be limited to a broad overview. The earlier-time t = 0,1 ps spectra are used to characterize the nature of the initial parent and daughter excitations, which is the excitation spectrum as discussed in the previous chapter, and the subsequent time-dependence to characterize each liquid's VR processes.

In a 3D spectrum, the time evolution of the horizontal stripes contains information about how vibrational energy progresses from a particular excited parent state toward a thermalized state. The time dependence of vertical stripes contains information about how vibrational population relaxation depends on which parent state was pumped. If a vertical stripe had a uniform intensity at a given instant, it would mean the excitations in that stripe had no memory of which parent state was initially excited. At longer times when the liquid has thermalized, there is no explicit memory of which state was initially excited, except in the limited sense that ΔT depends on the IR absorption coefficient α of the parent state. After the liquid thermalizes,

vertical stripes in the 3D spectrum would not be expected to be entirely uniform; the intensity variation along a vertical stripe would reflect variations in IR absorption coefficients across the pump tuning range.

Artifacts

The three types of artifacts, SFG, four-wave mixing (4WM) and self-phase modulation (SPM), were all observed at one time or another in Figures 6.5-6.8. For a reminder, each of these artifacts was thoroughly discussed in Chapter 3. The diagonal signals may include contributions from both parent vibrational populations and SFG artifacts. One can determine if a signal along the diagonal is solely an SFG artifact, because in that case there would be no vibrational population and no anti-Stokes signals in the corresponding horizontal stripe. For example, in Figure 6.7 at 2500 cm^{-1}, the diagonal signals appear to be purely SFG artifacts.

In Figure 6.8 the strongest effect of 4WM artifacts are seen. These are the stripes running from the far right side of the figure at t = 0,1 ps. These signals are the lower-wavenumber tails of the scattered light from a coherent 4WM signal generated at $2\omega_{IR} + \omega_{vis}$, which in the anti-Stokes spectrum would be peaked off the right hand side of the Figure, at 5800 cm^{-1}.

In Figure 6.5 both types of SPM artifacts are seen. These are the signals at the lowest wavenumbers, below the $\rho(NO_2)$ transitions. They appear as horizontal stripes extending toward zero wavenumber. A time-independent SPM artifact was observed when the IR pump was 3200 cm^{-1}. This run evidently exceeded the probe pulse intensity threshold for SPM. At some other IR wavenumbers such as 3000 cm^{-1}, intense SPM artifacts near t = 0 are seen, which resulted from pump-pulse enhanced SPM of the probe pulse. After 1 ps, these pump-enhanced SPM signals disappeared.

Nitromethane

First the shorter-time NM spectra at t = 0,1 ps in Figure 6.5 will be considered as the IR pump pulses were scanned through the CH-stretch region, from 3200 cm^{-1} to 2700 cm^{-1}. At 3200 cm^{-1}, well above the nominal CH-stretch absorption, there are no clearly-evident absorption bands (Figure 6.1a), but nonetheless Figure 6.5 shows excitations promptly appearing in ν(CN), $\delta(NO_2)$ and $\rho(NO_2)$. Thus there must be a combination-band transition near 3200 cm^{-1} that combines the character of these three modes. This example illustrates the ability of shorter-time 3D IR-Raman spectroscopy to detect and characterize weak combination-band transitions. At 3100 cm^{-1} there is a diagonal signal, but very little population in the lower-wavenumber modes, so the diagonal signal at 3100 cm^{-1} was primarily an SFG artifact. At 3000 cm^{-1}, where the IR pulses were near the absorption maximum of $\nu_a(CH_3)$, the 3D spectrum shows that both $\nu_a(CH_3)$ and $\nu_s(CH_3)$ were excited. This is a consequence of spectral overlap between the $\nu_a(CH_3)$ absorption peak and the higher-energy tail of $\nu_s(CH_3)$. This 3000 cm^{-1} excitation condition also promptly produced all lower-wavenumber vibrations except 607 cm^{-1} $\rho(NO_2)$. At 2900 cm^{-1}, pumping into the absorption maximum of $\nu_s(CH_3)$, little $\nu_a(CH_3)$ was seen but all lower-wavenumber vibrations except $\rho(NO_2)$ were seen, with 1402 cm^{-1} (symmetric CH-bend/nitro-stretch) especially prominent. At 2800 cm^{-1} all lower-wavenumber vibrations except 1562 cm^{-1} (asymmetric CH-bend/nitro-stretch) and 607 cm^{-1} (nitro-bend) promptly appeared. At 2700 cm^{-1}, something interesting happened. A great deal of excitation appeared at 1402 cm^{-1}, even though there was little CH-stretch excitation, which suggests the first overtone of the 1402 cm^{-1} CH-bend/nitro-stretch transition was pumped and observed.

Looking at the longer-time spectra in Figure 6.5, NM is shown proceeding toward a thermalized state. It is interesting that $\rho(CH_3)$ at 1104 cm^{-1} was never excited at shorter times,

indicating that this excitation is practically decoupled from the other normal modes. It is possible that the later-time excitation of $\rho(CH_3)$, as the NM approaches thermalization, results solely from intermolecular interactions with lower-energy excitations in the bath.

Looking at the intensity profiles along the vertical stripes of the lower-wavenumber bands, recall these spectra are plotted using a logarithmic intensity scale, which flattens out the pump wavenumber dependence of the intensity. Once the NM has thermalized one would expect these intensity profiles to approximately track the IR absorption spectrum in Fig. 6.1a, which has a maximum at 2968 cm^{-1}, a much weaker maximum at 3050 cm^{-1}, and little intensity above 3150 cm^{-1} or below 2850 cm^{-1}. In fact this is not quite what is observed. All the lower-wavenumber signals at longer delay times (except $\rho(CH_3)$ do have maxima near at 2968 cm^{-1} and 3050 cm^{-1}, but they also have excess populations below (e.g. 2750 cm^{-1}) and above (e.g. 3200 cm^{-1}) the CH-stretch resonances. Populating the lower-wavenumber excitations by pumping in this region surely indicates that combination and(or) overtone bands are being excited, and the magnitude of the lower-wavenumber population results from the enhanced sensitivity of IR-Raman spectroscopy to weaker IR absorption transitions.

d_3-Nitromethane

With d_3-NM (Figure 6.6), the shorter-time spectra at t = 0,1 ps will first be considered, as the IR pulses were tuned from 3000-2150 cm^{-1}. As shown in Figure 6.2b (and at the top of Figure 6.6), between 3000 cm^{-1} and 2400 cm^{-1} the only transitions in this deuterated liquid were overtones and combinations of nitro stretches. By tuning through this range, the 3D spectrum confirmed the assignments proposed in Figure 6.2b. When the band near 3000 cm^{-1} that was proposed to be $2\nu_a(NO_2)$ was excited, only $\nu_a(NO_2)$ was observed. Similarly at 2900 cm^{-1},

proposed to be $\nu_a(NO_2) + \nu_s(NO_2)$, both $\nu_a(NO_2)$ and $\nu_s(NO_2)$ were observed. At 2700 cm^{-1}, proposed to be $2\nu_s(NO_2)$, only $\nu_s(NO_2)$ was observed.

At IR pump wavenumbers where CD-stretches were excited, the dominant daughter excitations generated by VR were the ~1400 cm^{-1} nitro-stretches, and there was hardly any excitation of the ~1100 cm^{-1} CD-bends.

Comparing Figure 6.5 and 6.6 results in a quite interesting observation about CH-stretch relaxation of NM compared to CD-stretch relaxation of d_3-NM. The usual expectation would be that CH-stretch pumping would primarily generate CH-bend excitations, and CD-stretch pumping would primarily generate CD-bend excitations.[16] But in NM the nitro-stretch excitations are resonant with the CH-bend states, whereas in d_3-NM the nitro-stretch excitations are in the region between CD-stretches and CD-bends. So the question can be posed, is the relaxation of a CH-stretch or CD-stretch excitation on the methyl group more likely to involve the methyl group itself or the adjacent nitro group? With NM it is impossible to tell because there is so much coupling between the nitro-stretch and methyl-bend, but with d_3-NM it is clear that CD-stretch relaxation to the adjacent nitro group is much more efficient than to bends on the same methyl group.

ACN

ACN (Figure 6.7) was scanned from 3600-2150 cm^{-1}. The vertical stripes in the ACN spectra were more patchy than with NM (Figure 6.5). This is a reflection that the ACN IR absorption spectrum in the pumped region (Figure 6.3a) is less congested than NM (Figure 6.1a). In the first 0,1 ps, with 3600 cm^{-1} pumping, well above CH-stretch absorbances, a diagonal signal was seen but it was not entirely SFG artifact, since the corresponding horizontal stripe shows some excited-state populations of ν(CN) and δ(CCN). Since ν(CN) is 2253 cm^{-1}, the

most likely origin would be a combination with $\delta_s(CH_3)$ (1312 cm^{-1}), but the shorter-time 3D spectrum in Figure 6.7 with 3600 cm^{-1} pumping showed very little excitation near 1312 cm^{-1} and quite a bit at 379 cm^{-1}. Thus this excitation seemingly involved ν(CN) with at least one and probably multiple quanta (up to 3) of 379 cm^{-1} δ(CCN) bending excitations. Moving the pump wavenumber lower, nothing much was seen until the CH-stretches came into resonance. The higher-energy CH-stretches produced mainly ν(CN) and ν(CC), whereas the lower-energy CH-stretches produced mainly CH-bends. Pumping the region just below the CH-stretches (2800-2400 cm^{-1}) produced little vibrational excitation except near 2600 cm^{-1} where a small amount of ν(CN) and δ(CCN) appeared, indicating that 2600 cm^{-1} IR pulses pumped the ν(CN) + δ(CCN) combination. Nothing much was seen below 2400 cm^{-1} until the 2253 cm^{-1} ν(CN) transition was pumped, and at that point $\delta_s(CH_3)$ and ν(CC) was promptly observed. Looking at the longer-time data, the primary daughter excitations from CH-stretch pumping and from CN-stretch pumping were CH-bends and ν(CC).

d_3-ACN

The d_3-ACN spectrum in Figure 6.8 was scanned from 3400-2000 cm^{-1}. At the highest wavenumbers 3400-2600 cm^{-1}, the 3D spectra confirm the assignments given in Figure 6.4b and at the top of Figure 6.8, where combination bands of ν(CN) with δ(CCN), ν_s(CC) and δ_s(CD) are indicated. When the CD-stretch and CN-stretch regions are pumped, the other prompt excitations were small amounts of CD-bend, CC-stretch and CCN-bend. Looking at the longer-time data, when the CD-stretch and CN-stretch excitations decayed they produced CD-bends, CC-stretches and CCN-bends.

6.5 Conclusions

The 3D spectra were quite complicated due to the multitude of off-diagonal peaks. With this 3D method, the cross-peaks at shorter delay times revealed the nature of the initial excitation, a key feature required for excitation spectroscopy as will be seen in the remaining chapters. Especially when the initial excitation was a combination band or overtone, and even when those bands were very weak in the IR absorption spectrum, the 3D spectra did a remarkable job of characterizing which excitations were produced when those weak bands were pumped. Looking at longer-time spectra, it was easy to characterize the VR processes and identify which daughter vibrations were created from different parent excitations.

6.6 3D IR-Raman Spectra

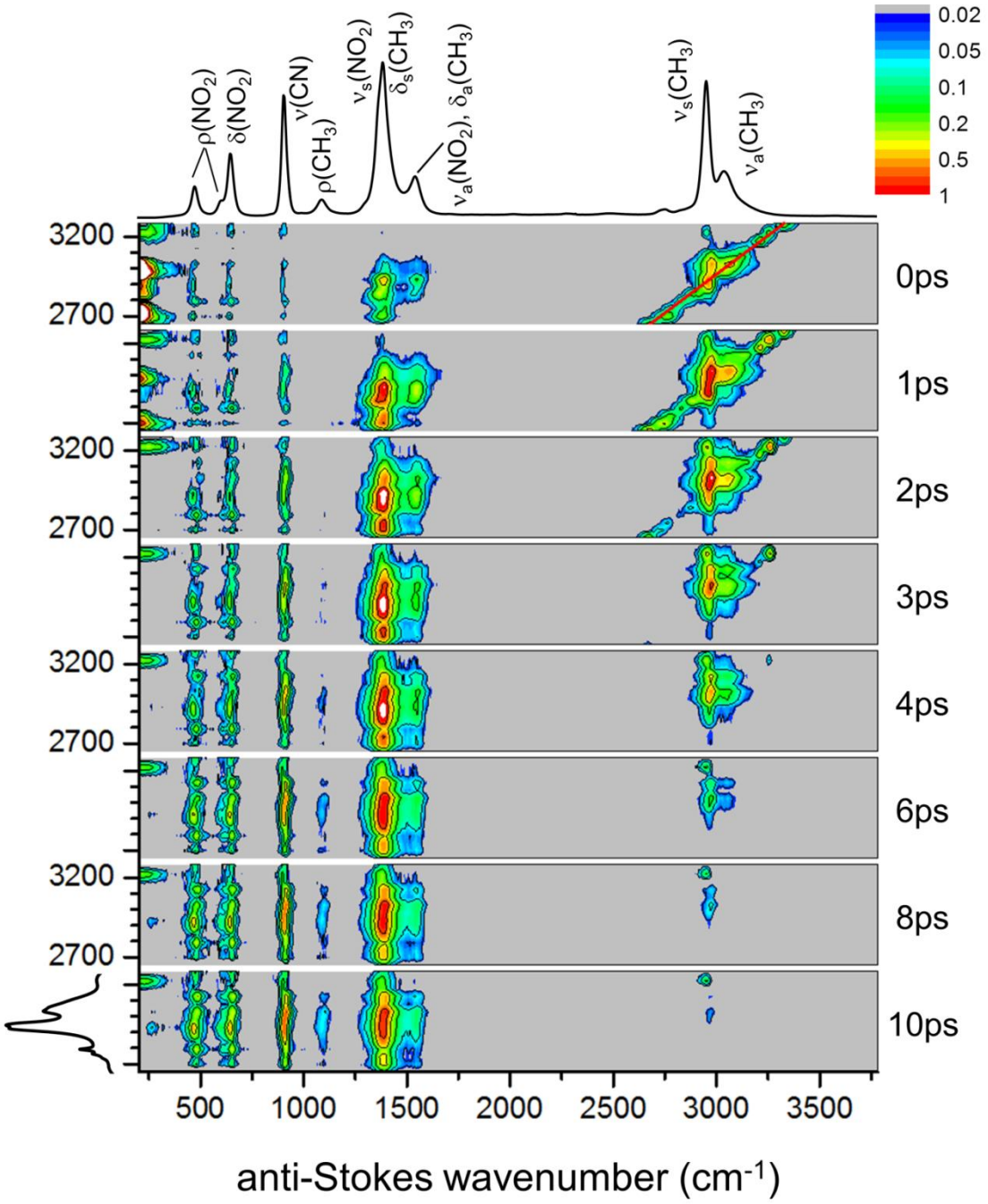

Figure 6.5. 3D IR-Raman spectrum of nitromethane. A reference Raman spectrum with assignments was drawn above the top panel and a reference IR spectrum to the left of the bottom panel. A reference diagonal was indicated in the top panel. Note logarithmic intensity scale. Figures 6.6-6.8 are explained similarly.

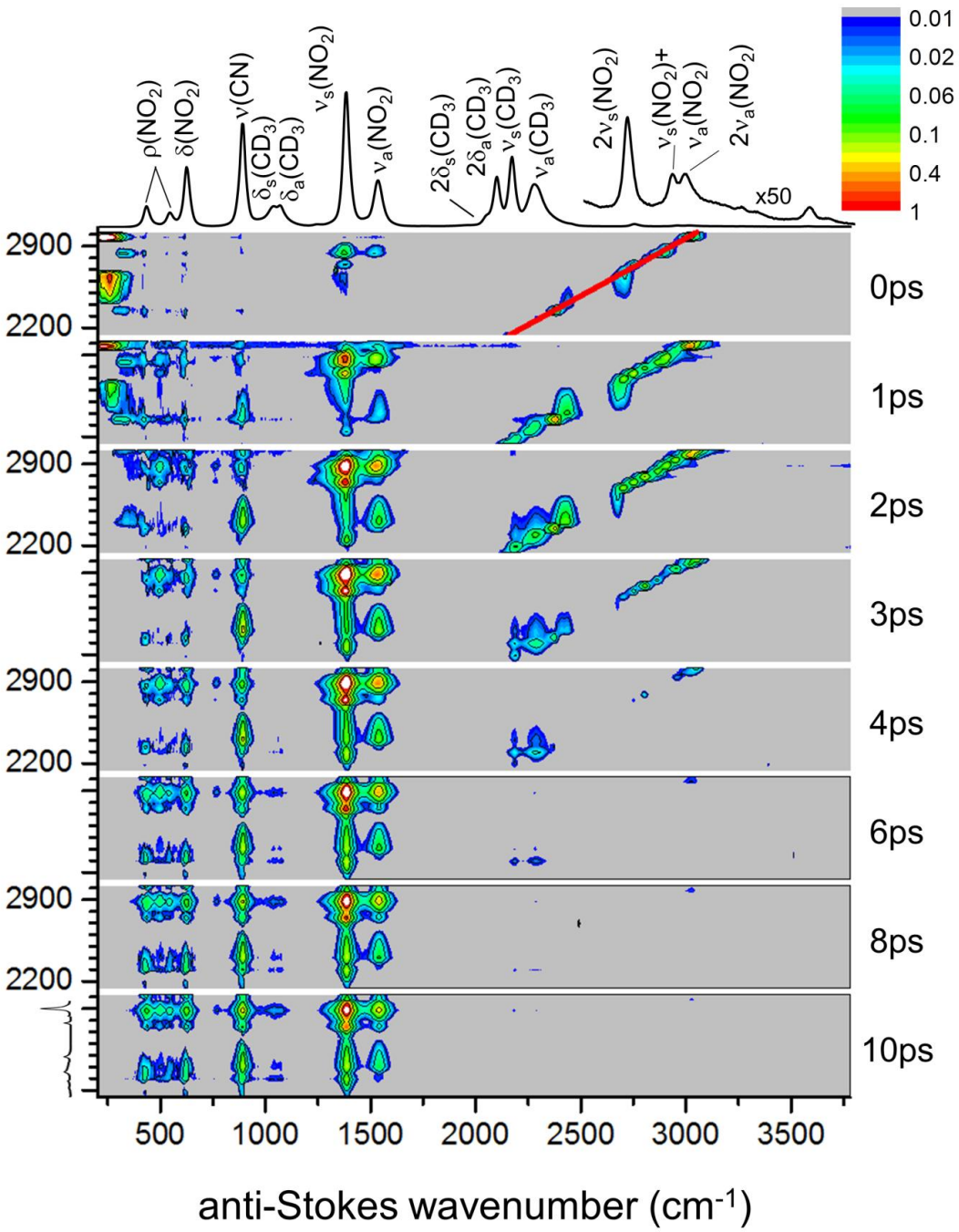

Figure 6.6. 3D IR-Raman spectrum of d_3-nitromethane.

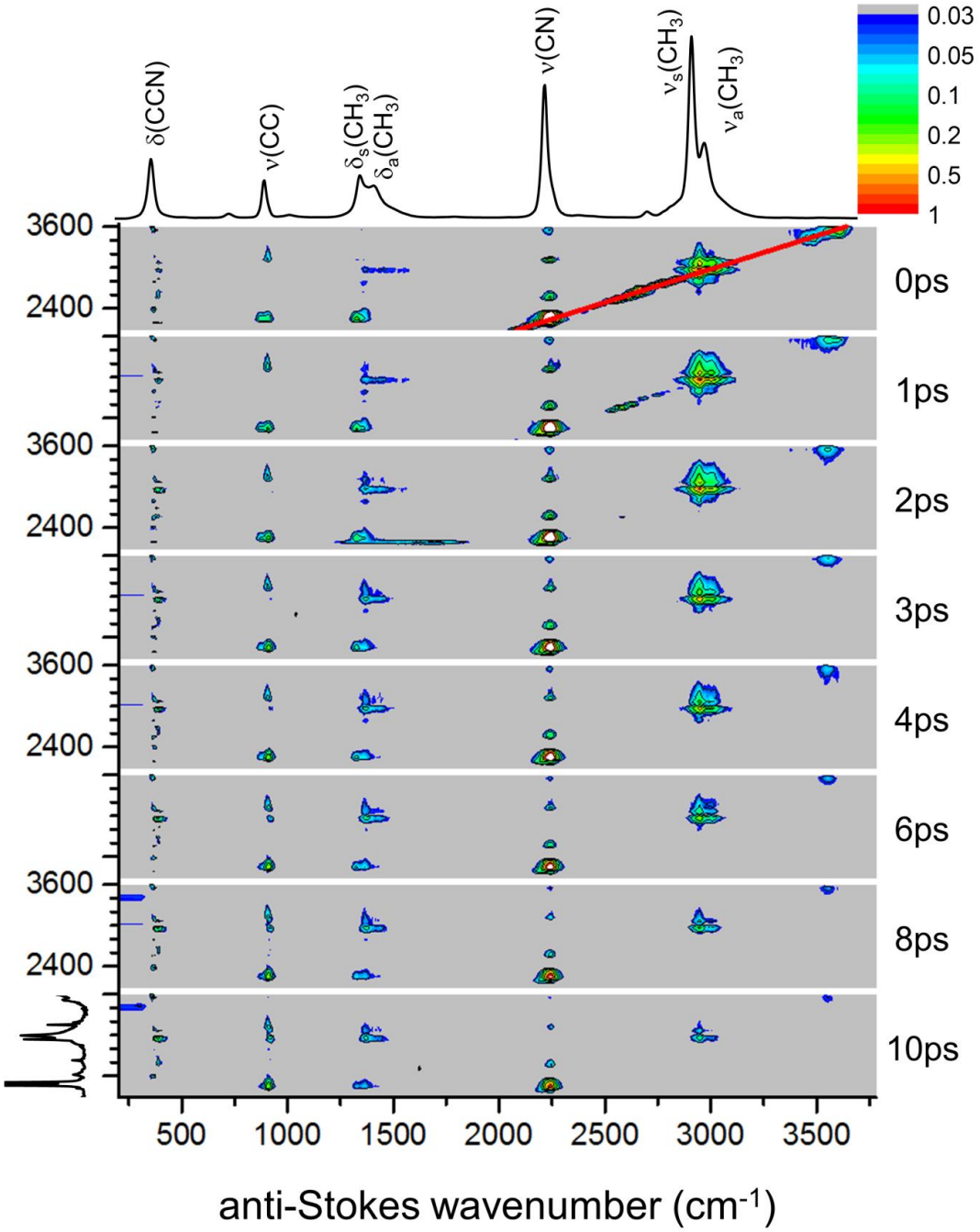

Figure 6.7. 3D IR-Raman spectrum of acetonitrile.

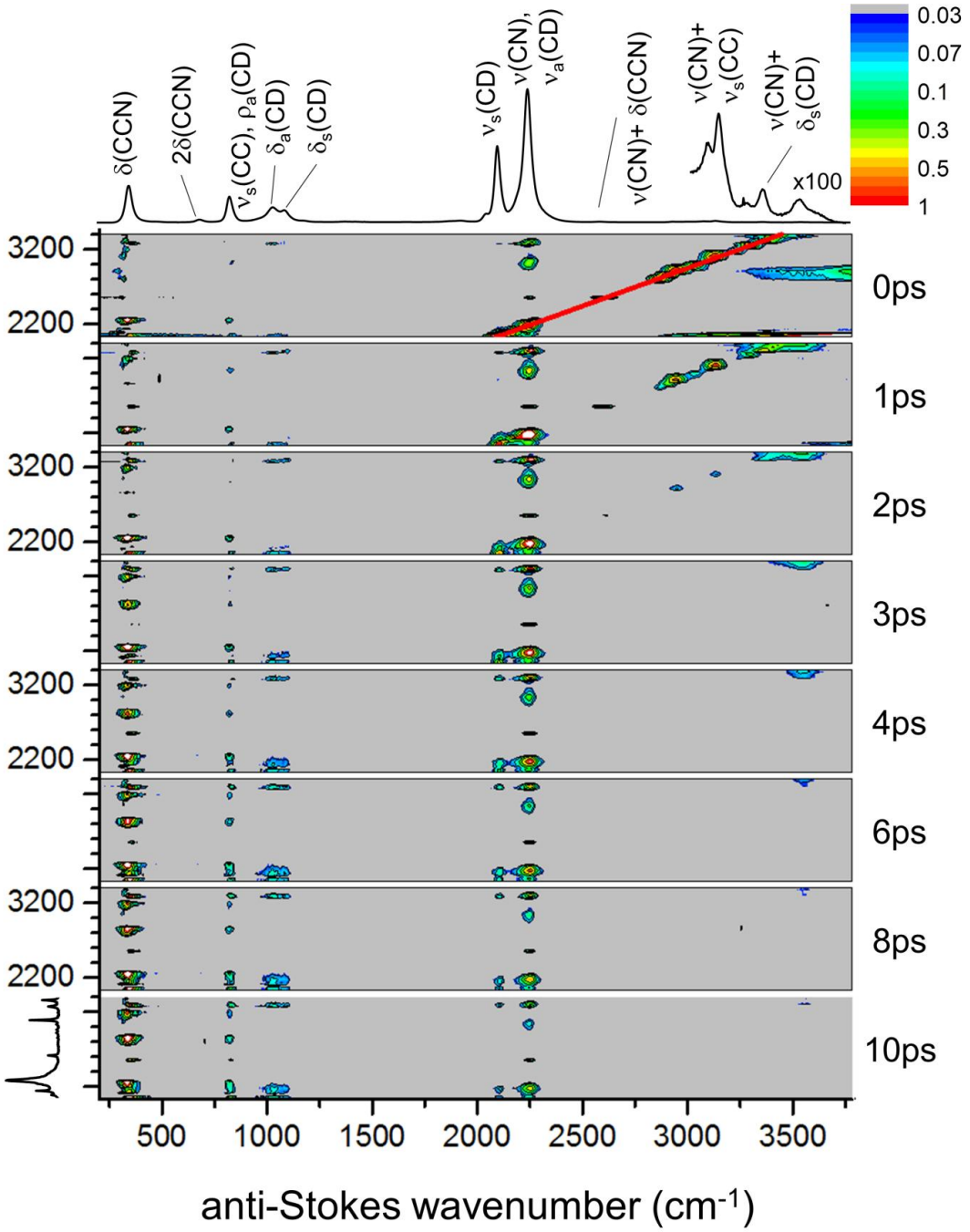

Figure 6.8. 3D IR-Raman spectrum of d_3-acetonitrile.

6.7 References

1. Deak, J. C.; Iwaki, L. K.; Dlott, D. D., High-Power Picosecond Mid-Infrared Optical Parametric Amplifier for Infrared Raman Spectroscopy. *Opt Lett* **1997,** *22* (23), 1796-8.

2. Deàk, J. C.; Iwaki, L. K.; Dlott, D. D., When Vibrations Interact: Ultrafast Energy Relaxation of Vibrational Pairs in Polyatomic Liquids. *Chemical Physics Letters* **1998,** *293*, 405-411.

3. Deàk, J. C.; Iwaki, L. K.; Dlott, D. D., Vibrational Energy Relaxation of Polyatomic Molecules in Liquids: Acetonitrile. *Journal of Physical Chemistry* **1998,** *102*, 8193-8201.

4. Deàk, J. C.; Iwaki, L. K.; Dlott, D. D., Vibrational Energy Redistribution in Polyatomic Liquids: Ultrafast Ir-Raman Spectroscopy of Nitromethane. *Journal of Physical Chemistry A* **1999,** *103*, 971-979.

5. Deàk, J. C.; Iwaki, L. K.; Rhea, S. T.; Dlott, D. D., Ultrafast Infrared-Raman Studies of Vibrational Energy Redistribution in Polyatomic Liquids. *Journal of Raman Spectroscopy* **2000,** *31*, 263-274.

6. Shigeto, S.; Pang, Y.; Fang, Y.; Dlott, D. D., Vibrational Relaxation of Normal and Deuterated Liquid Nitromethane. *Journal of Physical Chemistry B* **2008,** *112*, 232-241.

7. Wells, A. J.; Wilson, E. B., Infra-Red and Raman Spectra of Polyatomic Molecules Xiii. Nitromethane. *Journal of Chemical Physics* **1941,** *10*, 314-318.

8. McKean, D. C.; Watt, R. A., Vibrational Spectra of Nitromethanes and the Effects of Internal Rotation. *Journal of Molecular Spectroscopy* **1976,** *61*, 184-202.

9. Hill, J. R.; Moore, D. S.; Schmidt, S. C.; Storm, C. B., Infrared, Raman, and Coherent Anti-Stokes Raman Spectroscopy of the Hydrogen/Deuterium Isotopomers of Nitromethane. *Journal of Physical Chemistry* **1991,** *95*, 3037-3044.

10. Courtecuisse, S.; Cansell, F.; Fabre, D.; Petite, J. P., Comparative Raman Spectroscopy of Nitromethane-H_3, Nitromethane-D_3, and Nitroethane up to 20 Gpa. *Journal of Chemical Physics* **1998,** *108* (17), 7350-7355.

11. Shkurinov, A.; Jonusauskas, G.; Rullière, C., Vibrational Spectrum of Liquid Nitromethane Revisited Using Polarization-Sensitive Coherent Anti-Stokes Raman Scattering (Cars) Spectroscopy. *Journal of Raman Spectroscopy* **1994,** *25*, 359-364.

12. Miller, P. J.; Block, S.; Piermarini, G. J., Effects of Pressure on the Vibrational Spectra of Liquid Nitromethane. *Journal of Physical Chemistry* **1989,** *93*, 462-466.

13. Herzberg, G., *Molecular Spectra and Molecular Structure Ii. Infrared and Raman Spectra of Polyatomic Molecules*. Van Nostrand Reinhold: New York, 1945.

14. Pace, E. L.; Now, L. J., Infrared Spectra of Acetonitrile and Acetonitrile-D_3. *Journal of Chemical Physics* **1968,** *49*, 5317-5325.

15. Hamm, P.; Zanni, M. T., *Concepts and Methods of 2d Infrared Spectroscopy*. Cambridge University Press: Cambridge, 2011.

16. Laubereau, A.; Kaiser, W., Vibrational Dynamics of Liquids and Solids Investigated by Picosecond Light Pulses. *Reviews of Modern Physics* **1978,** *50* (3), 607-665.

Chapter 7: Vibrational Energy Flow in Nitrobenzene: Unidirectional Energy Flow†

7.1 Introduction

In this chapter IR-Raman and excitation spectroscopy are used to probe vibrational energy flow from one location of a molecule to another. Recall this is the materials science approach to understanding energy flow which treats it as nanoscale thermal conduction.[1] Energy flow from the nitro groups to the phenyl groups and vice versa was monitored in liquid nitrobenzene at ambient temperature. Excitation spectroscopy was used to find IR pump wavenumbers to find pulses that generated vibrational excitations initially localized on the nitro or phenyl group. Then, fixing the pump pulses at either of these selected wavenumbers, IR-Raman spectroscopy probes energy flow between the two groups. The restricted energy flow between them, and the complete lack of energy flow in the direction of nitro to phenyl, in other words a net unidirectional vibrational energy flow, was surprising. Being able to engineer molecules that promote vibrational energy flow in particular directions would be a useful capability of a "molecular toolbox" for the design of molecular electronic components, phononic components such as thermal diodes, and molecular machinery that must dissipate heat in order to perform efficiently.

As a reminder, one issue that arises with the Raman probing technique is selection bias. Not all of the vibrational modes are probed, only those with sizeable Raman cross-sections. For the nitro groups, both stretching transitions which together constitute the vast majority of energy in the nitro group are probed. But for the phenyl group only some of the transitions are

†Parts of this chapter are recreated from work previously published as: Pein, B. C.; Sun, Y.; Dlott, D. D., Unidirectional Vibrational Energy flow in Nitrobenzene. *Journal of Physical Chemistry A* **2013**, *117(29)*, 6066.

selectively probed, and for these transitions the energy in each mode can be quantitatively determined. Recall that previous work by the Dlott laboratory utilized a ultrafast calorimetry to study energy flow in benzene.[2] There a benzene solution was used containing CCl_4, a molecular thermometer,[3-7] which monitored the total energy dissipation from the pumped benzene.[2] By subtracting the observed energy the total input energy, the time dependence of the unobserved energy was determined and except at the earliest times, its time dependence was the same as the observed energy. Thus the modes observed in the phenyl groups in this nitrobenzene study should provide a relatively unbiased measure of the total energy content of the phenyl groups.[2]

Because these are molecules in the liquid phase, there will be intermolecular vibrational relaxation (VR) processes. This results in an indirect flow of energy from nitro to phenyl or vice versa, since the specific input vibrational energy will eventually be thermalized via vibrational cooling resulting from multiple VR steps. In the aryl-halide work of Chapter 4, intermolecular VR processes were not explicitly distinguished from intramolecular VR (IVR) processes in the discussion since those molecules had no distinct locations within them to measure energy flow to and from. However in the case of nitrobenzene, when discussing direct energy flow between the two groups intra- and intermolecular processes must be distinguished. For this reason the focus of this study will be the first few picoseconds, before much intermolecular energy transfer occurs. At these shorter delay times the dominant energy flow pathways are from the vibrationally hot part of the molecule into the rest of the molecule.[2]

7.2 Results

IR and Raman Spectrum and Assignments

Figure 7.1 shows the nitrobenzene Stokes Raman spectrum, obtained with the picosecond probe pulses, and the IR spectrum. The transition assignments are based on the literature,[8]

confirmed by normal mode calculations using MP2 perturbation theory with the 6-31G basis in the Gaussian 09 computational package. The results of these calculations are shown in Section 7.5 where the modes visible in the experiment are assigned and the others are numbered.

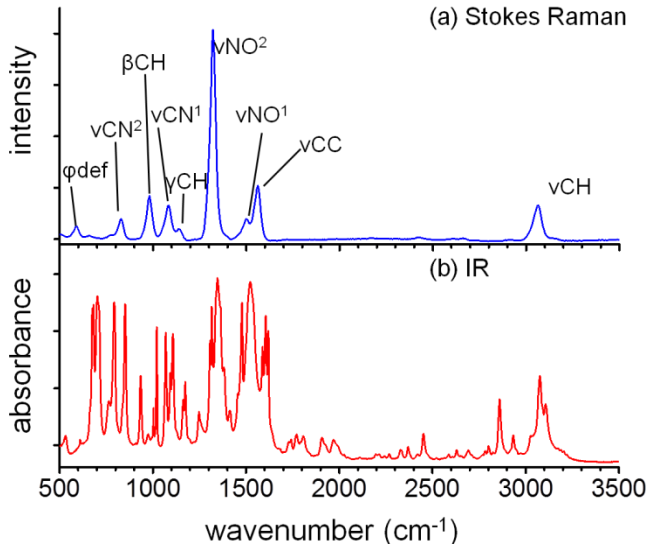

Figure 7.1. Infrared and Raman spectrum of nitrobenzene. The Raman spectrum (a) has the most intense transitions assigned. The spectrum was obtained using the picosecond laser with a 25 cm^{-1} resolution. The Infrared spectrum (b) has a 4 cm^{-1} resolution.

Section 7.6 shows illustrations of the normal modes and their classifications based on their atomic displacement. There the 36 normal modes have been grouped into three categories, 25 phenyl modes and 2 nitro modes, defined as modes where the atomic displacements were predominantly on phenyl or nitro groups, and 9 global modes, defined as those where atomic displacements were substantial on both moieties.

One helpful fact to remember is that νCC (1590 cm^{-1}) is a phenyl ring stretch and νNO^1 (1512 cm^{-1}) and νNO^2 (1335 cm^{-1}) are (respectively) anti-symmetric and symmetric nitro stretches, as depicted in Section 7.6. As will be shown, these assignments can be used for initial assessments of energy localization or energy flow between nitro and phenyl.

Excitation Spectroscopy

Figure 7.2 is the excitation spectrum, where the Raman probe pulses were fixed at 1 ps delay and the IR pump pulses were tuned from 2500-3500 cm^{-1}. As a reminder, the excitation spectrum is the 3D IR-Raman spectrum at 1 ps delay.

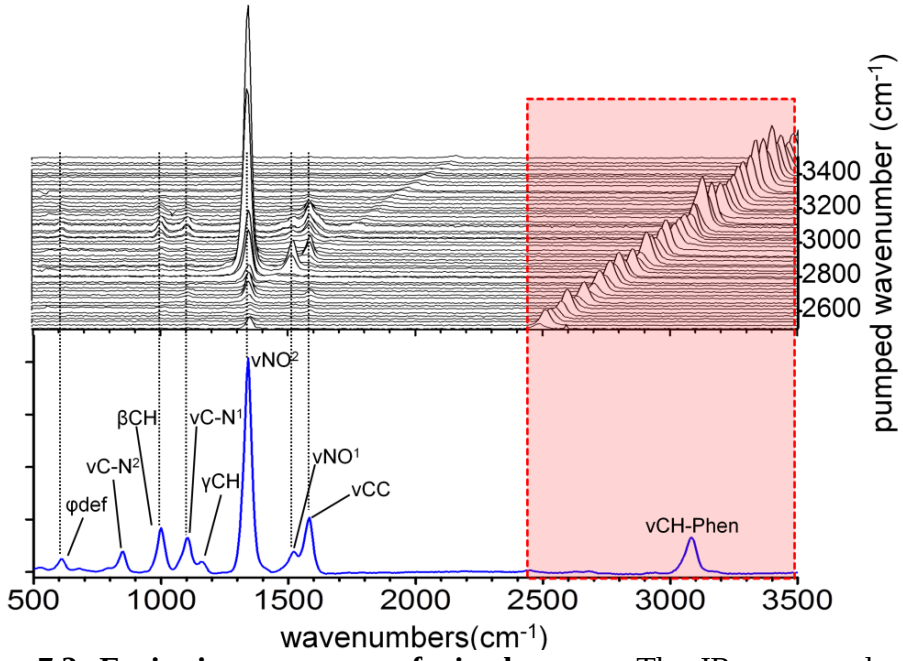

Figure 7.2. Excitation spectrum of nitrobenzene. The IR pump pulses were scanned from 2500 to 3500 cm^{-1} while the anti-Stokes Raman spectrum was monitored at 1 ps delay. The anti-Stokes intensities are proportional to the instantaneous vibrational population change $\Delta n(t)$, except on the diagonal (shaded region) where there are artifacts from nonlinear light scattering (NLS).The Stokes Raman spectrum is presented for reference. These results show which pump wavenumbers produced the most phenyl ring excitation, as judged by the intensity of the νCC transition, and which IR pump wavenumbers produced the most nitro excitations, as judged by the intensities of νNO^1 and νNO^2.

The anti-Stokes intensity changes relative to the ambient temperature values (at -3 ps) were plotted versus IR wavenumber. Recall that the population changes $\Delta n(t)$ at each delay t are proportional to proportional to the fraction $I_\omega^{AS}/I_\omega^{ST}$. The Stokes spectrum with assignments from Figure 7.1a is shown beneath the excitation spectrum, inasmuch as it represents the Raman cross-section variation with wavenumber. As a reminder the signals at $\omega_{probe} + \omega_{IR}$ along the diagonal

arise from anti-Stokes scattering from resonant nitrobenzene transitions at ω_{IR} directly pumped by IR pulses as well as contributions from sum-frequency generation nonlinear light scattering (NLS) signals.[9] These two contributions have different time dependences. The resonant signals decay with the excited-state lifetime T_1 and the NLS signals decay with the apparatus temporal response (~1 ps).

The results in Figure 7.2 could be used to find the pump wavenumbers that best selectively produced nitro or phenyl excitations. However it is better to use population, or occupation number, changes rather than anti-Stokes intensities. In Figure 7.3 $\Delta n(t = 1\ ps)$ has been plotted for the peaks with the largest values as a function of IR pump wavenumber. These were the νCC, νNO^1 and νNO^2 vibrations.

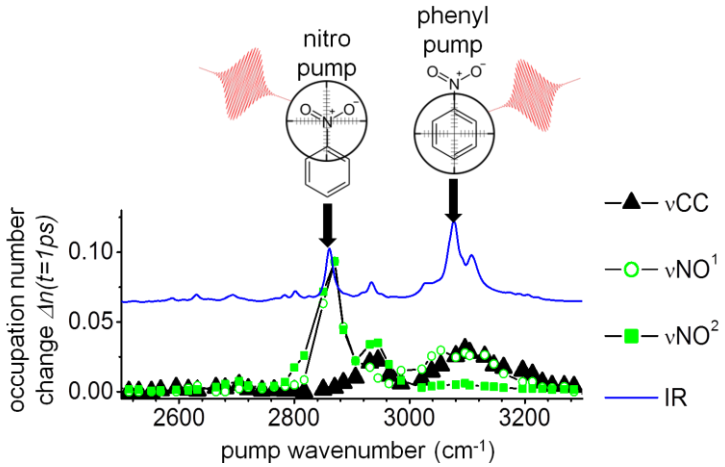

Figure 7.3. Population changes Δn(t) of nitrobenzene at 1 ps delay. The population change of νCC (a phenyl vibration), and νNO^1 and νNO^2 (nitro vibrations), as the IR pump pulses were tuned. For reference, the IR absorption spectrum is superimposed. With 2880 cm^{-1} pumping, only nitro vibrations νNO^1 and νNO^2 were excited. With 3080 cm^{-1} pumping, phenyl vibrations were excited and also some νNO^1.

Based on Figure 7.3, the 2880 cm^{-1} pulses create only νNO^1 and νNO^2 excitations with no νCC. This makes sense if one assigns the weak IR transition at 2880 cm^{-1} as the νNO^1 + νNO^2 combination band. This 2880 cm^{-1} IR wavenumber will be used for nitro pumping experiments.

There is no ideal IR wavenumber to produce only phenyl excitations. With 3080 cm^{-1}, close to the phenyl νCH stretch absorption, a substantial amount of νCC is created with no $νNO^2$, but unfortunately there was some $νNO^1$. Thus the phenyl excitation experiments with 3080 cm^{-1} pumping will have an initial population of $νNO^1$ that must be taken into account.

Anti-Stokes Transients

Figure 7.4 shows IR-Raman spectra with nitro or phenyl pumping. Note the nonlinear time axis that has more spectra in the -3-10 ps range than in the 30-100 ps range. The nitro pumping results in Figure 7.4a show that the number of daughter excitations created by relaxation of the initial nitro excitation is very limited, and in fact almost all of the observed energy is seen only in the $νNO^1$ or $νNO^2$ transitions.

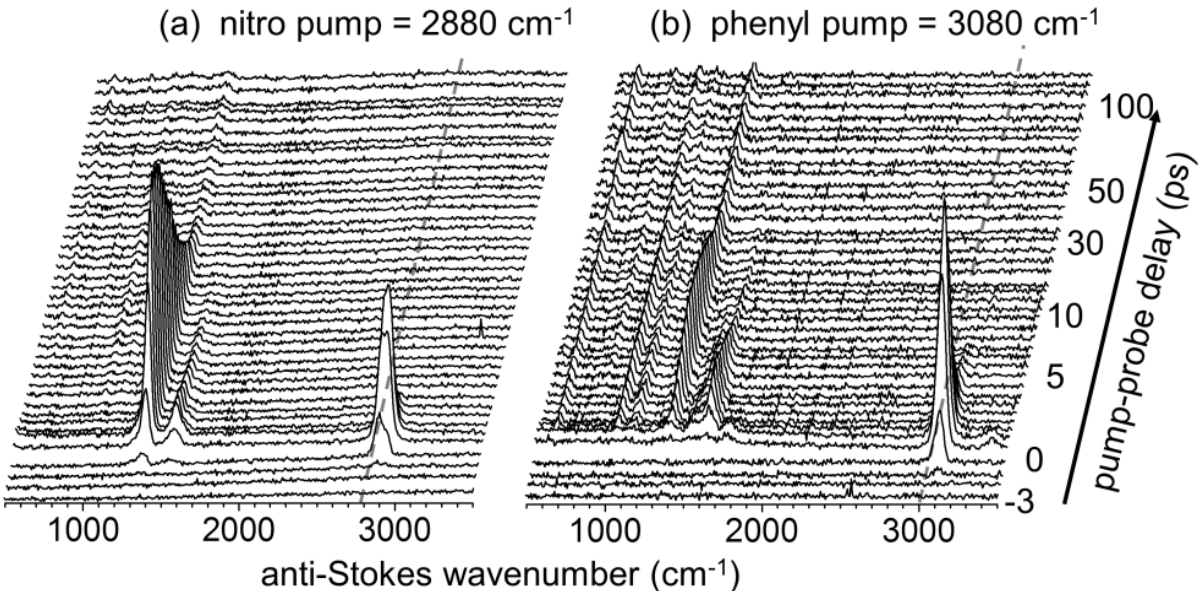

Figure 7.4. IR-Raman spectra of nitrobenzene. IR-Raman spectra using (a) nitro pumping or (b) phenyl pumping. Note the nonlinear time axis. With nitro pumping, the signals at 2880 cm^{-1} were mostly coherent artifact.

These results make it clear that when vibrational energy is deposited on the nitro group, it stays on the nitro group and does not transfer to phenyl before it decays into the bath. This is not the

case for phenyl pumping, where the daughter vibrations are numerous, and at least some of the daughter excitations were global excitations such as νCN[1].

Figure 7.5 shows time-dependent population changes *Δn(t)* following nitro or phenyl pumping. From the longer time values, after the vibrations thermalized, the net temperature jump (T-Jump) was ~30K. Using Figure 7.5, as done in the aryl-halide study, the simplest way to understand how these different vibrations became excited is to look at their rising edges.[2,10-12]

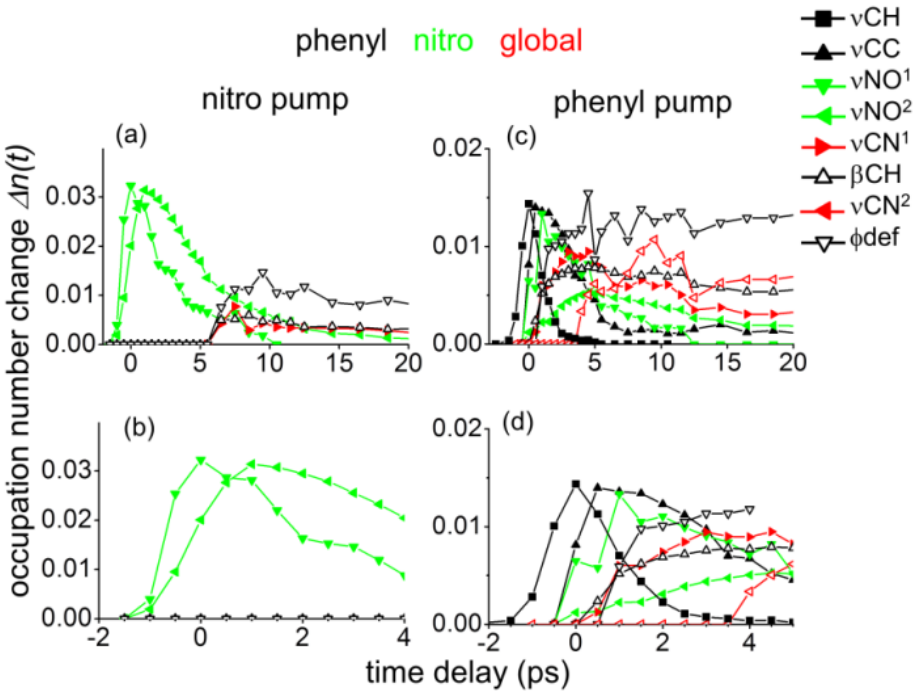

Figure 7.5. Time-dependent populations after nitro or phenyl pumping. The same transients for (a) nitro and (b) phenyl pumping are shown on expanded time ranges in (b) and (d).

Recall that from the three-stage model there are three ways vibrations are excited and that some vibrations become excited in more than one way. The three ways are: (1) Excited by the IR pulses. The daughters with instantaneous rising edges, due to coherent coupling with the parent, are recognized as being those with significant populations at $t = 0$. (2) The first-generation of daughter vibrations excited by parent decay, recognized by rising edges that track the parent decay. (3) Delayed excitations in second-generation daughters created by the decay daughter

vibrations excited in the second way. Additionally, daughters may be excited via vibrational up-pumping from the T-jump of the bath. Up-pumping describes a situation where multiple bath quanta, created by daughter VR, can excite lower energy vibrations.

In the case of nitro pumping, the parent state $\nu NO^1 + \nu NO^2$ was not directly observed, because the $\nu NO^1 + \nu NO^2 \rightarrow$ ground state transition at 2880 cm^{-1} has a small Raman cross-section. Since this experiment does not have enough spectroscopic resolution to detect the anharmonic shifts, the combination excitation $\nu NO^1 + \nu NO^2$ appears as simultaneous excitation of both fundamentals, νNO^1 near 1512 cm^{-1} and νNO^2 near 1335 cm^{-1} due to the $\Delta v = \pm 1$ selection rules of Raman scattering.[13,14] In Figure 7.5b, both νNO^1 and νNO^2 signals have a component of instantaneous excitation since both have significant populations at $t = 0$. They both rise to the same occupation number, ~3%. It is thought that the slightly different risetimes are due to noise from the measurement and data analysis, so these shorter-time signals are attributed to combination-band excitations created by IR pulses. After ~1 ps, the νNO^2 excitation level does not fall as fast as νNO^1, even though at longer times <5 ps, both appear to decay with about the same time constant. This is consistent with the idea that two populations[4] of νNO^2 are seen, one instantaneous population created by IR pumping of the combination band and one first-generation daughter population created by the process $(\nu NO^1 + \nu NO^2) \rightarrow \nu NO^2$. Furthermore some of the longer-time νNO^2 population might also be created by the process $\nu NO^1 \rightarrow \nu NO^2$ + bath (~177 cm^{-1}). Some of the νNO^1 population seen at later times might also be fundamental excitations created by the process $(\nu NO^1 + \nu NO^2) \rightarrow \nu NO^1$.

Additionally, in Figure 7.5a some ϕdef and βCH excitation is seen starting at ~5 ps. Thus ϕdef and βCH are the sole observed delayed excitations created by nitro pumping. The delayed

appearance of the lower-wavenumber ϕdef indicates it was not created by the decay of nitro excitations, but instead by vibrational up-pumping due to the T-jump of the bath.

In the case of phenyl pumping, the instantaneously-excited states were νCH plus some νNO^1, as described above, but in addition there was some instantaneous νCC. Direct laser generation of νCH and νCC has also been observed in previous studies of benzene.[2,15] The first generation daughters were βCH, νCN, ϕdef^1 and νNO^2, as determined from the transients in Figure 7.5d having rising edges that correspond to the ~1 ps decay of νCH. The νNO^2 excitations in Figure 7.5c have a rise that corresponds with the ~5 ps decay of νNO^1, which is suggestive of a $\nu NO^1 \rightarrow \nu NO^2$ relaxation pathway that created delayed νNO^2 from laser-excited νNO^1. Other delayed excitations that could be seen in Figure 7.5c were βCH, νCN^1 and ϕdef.

7.3 Discussion

Superficially, nitrobenzene appears to be quite similar to other molecules that have been studied previously in the Dlott laboratory with the IR-Raman technique.[6,7] For instance with nitrobenzene, when the νCH transition around 3080 cm^{-1} is pumped, there were three instantaneously excited vibrations, νCH, νCC and νNO^1, whereas in benzene IR pumping of νCH generated four instantaneously-excited vibrations, νCH, νCC , ϕdef, and the ring-breathing mode ν_2.[2,15] The thermalization process in benzene was ~50 ps,[2] about the same as in fluoro-, chloro-, bromo- and iodo-benzene,[16] all somewhat slower than the ~20 ps thermalization of nitrobenzene. The faster thermalization in nitrobenzene is attributed to molecule-to-bath pathways not present in benzene or the aryl-halides. These presumably involve nitro scissors and nitro torsion modes that couple very well with the bath, as seen in prior studies of nitromethane.[5,11,17]

Vibrational Energy Densities

But viewed up close, nitrobenzene has a remarkable property regarding nitro-to-phenyl energy transfer. In order to look at this more closely, in Figure 7.6a and 7.6b the energy density change in each observed mode has been plotted and coded by the three categories phenyl, nitro and global, as defined in the Section 7.6 mode vector illustrations. Recall that energy densities in IR-Raman experiments are spatially averaged over an inhomogeneous energy distribution created by the Gaussian laser beam profiles and the exponential attenuation of the IR pump pulses in the sample.[6]

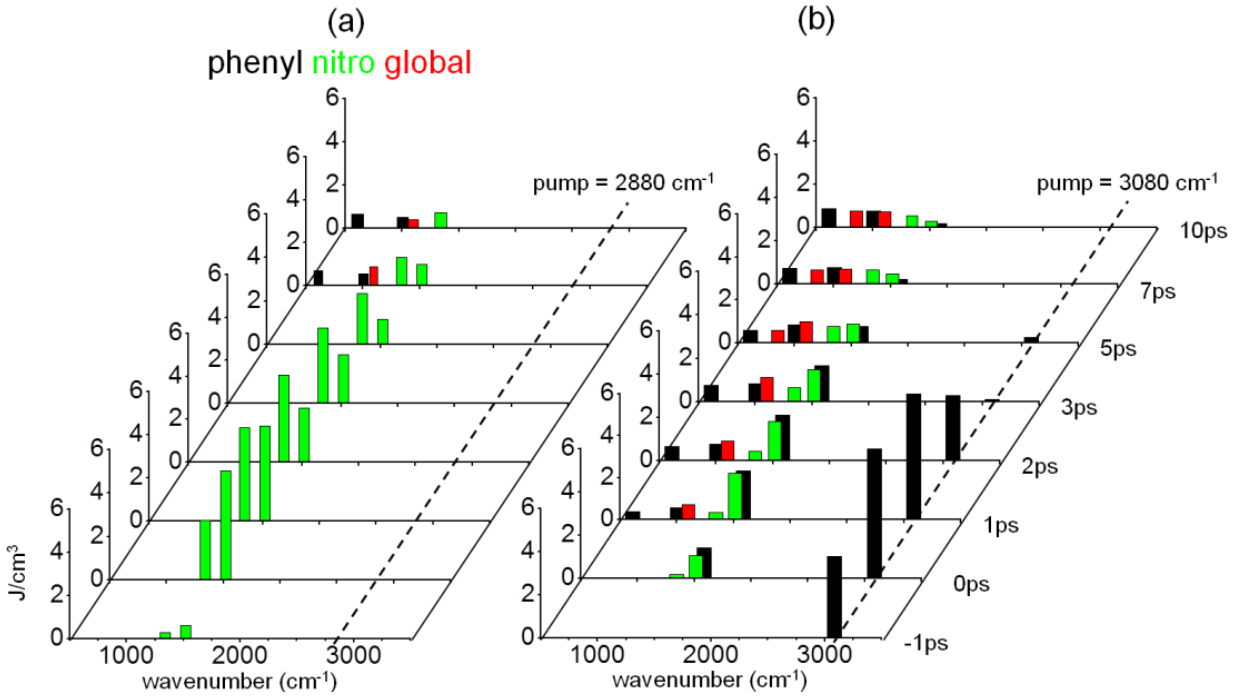

Figure 7.6. Nitrobenzene transient energy densities. For the first several picoseconds after (a) nitro pumping, only nitro excitations were present. The global and phenyl excitations were created by the T-jump of the bath. For (b) phenyl pumping, phenyl νCH excitations plus some νNO^1 where initially generated. As time progresses, the nitro population does not build up, but the generation of global modes indicates that phenyl excitations create amplitude indirectly on nitro by generating global excitations.

As discussed earlier, the energy in the observed modes is representative of the total energy flow. Then Figure 7.6a shows clearly that there was no detectable energy transfer from

the laser-excited nitro group vibrations to either phenyl or global modes during the first 5 ps. The νNO^1 + νNO^2 combination excitation is truly a local-mode excitation. Furthermore its putative daughter vibrations are the fundamentals νNO^1 and νNO^2 also localized on the nitro group, and whose decays also do not generate detectable phenyl or global excitations. In fact it appears that the only relaxation pathways for the nitro stretching excitations, combinations and fundamentals, is to dump excess energy into the bath, presumably via short-lived scissors and torsion intermediates. Around 7 ps, a little bit of phenyl and global mode excitation appears, but this is not the result of a direct nitro-to-phenyl process. Instead it results from vibrational up-pumping of these lower-energy modes by the T- jump of the bath.

In assessing Figure 7.6b, recall that the pump pulses excited the νCH, νCC and νNO^1 vibrations. There is no evidence for direct phenyl-to-nitro transfer, inasmuch as the nitro excitations do not build up with the decay of the phenyl parent νCH. There also is no evidence for νNO^1-to-phenyl transfer, inasmuch as the phenyl excitations do not build up with the decay of nitro excitations. There is some energy transfer from the higher-energy νNO^1 to NO^2. Thus it appears as if the laser-generated νNO^1 population simply decays into νNO^2 or bath excitations and does not generate any phenyl excitations. However there is a pathway for phenyl-to-nitro transfer as seen by the generation of global excitation, primarily νCN^1, which is a nitro-phenyl stretching excitation. Phenyl-to-global transfer may be viewed as a process whereby vibrational amplitude originally localized on phenyl alone, spreads out to encompass both phenyl and nitro.

To understand the restricted vibrational energy transfer of nitrobenzene without elaborating on the complexities of anharmonic coupling, it is useful to consider the atomic motions involved in the relevant normal modes. As seen in Section 7.6, the symmetric and antisymmetric nitro stretch modes have practically no amplitude on the phenyl group, so there is

little coupling to the $\nu NO^1 + \nu NO^2$ parent state excited by the IR pulses, or the νNO^1 or νNO^2 first-generation daughters. The only potentially efficient pathways for nitro-to-phenyl transfer are when the first-generation daughters excite the second-generation nitro scissors and torsion modes, global modes that could eventually produce phenyl excitation. But these nitro torsions and scissors couple more strongly to the bath than to phenyl, and they have short lifetimes so there is little opportunity to excite phenyl. With phenyl excitations, there is no efficient way to excite nitro stretch modes, so the only possible phenyl-to-nitro routes involve global mode excitations. The global modes are lower-energy modes, so most of the initial phenyl excitations end up in the other phenyl vibrations. Only the small fraction of phenyl energy that excites global modes has a chance to make it over to nitro, where it can only excite nitro motions that drain quickly into the bath. Thus nitro-to-phenyl transfer is practically absent, and phenyl excitations generate only small amplitudes of the global modes.

7.4 Conclusions

Excitation and IR-Raman spectroscopies have been used to study energy transfer between two different parts of the same molecule. Naturally one must have a molecule with two different locations. Substituted benzenes like the aryl-halides wouldn't work since they have no substituent vibrations to speak of. However benzenes with a polyatomic substituent such as nitrobenzene have this property. Quantum chemistry was used here to classify the modes into three groups, in this case phenyl, substituent and global. Then, using excitation spectroscopy, IR pump wavelengths were found that best produced excitations initially localized on phenyl or substituent. VR was then monitored after pumping each location using IR-Raman spectroscopy.

Applying this method to nitrobenzene showed that energy input to the nitro group stays on the nitro group. Energy does not flow to the phenyl group before it decays into the bath.

Even though the phenyl group could not be excited without some νNO^1 excitation, one can still draw firm conclusions, because the νNO^1 energy is not transferred to phenyl. Energy input to the phenyl group mostly stays on the phenyl group, but a small fraction goes into global modes. So with phenyl excitation, an initial excitation that has amplitude solely on the phenyl group time evolves to have some amplitude on the nitro group. Thus nitrobenzene could be viewed as a (rather poor) vibrational energy diode in that energy flow is unidirectional. Energy flow in the nitro-to-phenyl direction is absent, while energy flow in the phenyl-to-nitro direction is poor.

As discussed in Chapter 1, the remarkable behavior of the nitro group in nitrobenzene can have implications for energetic materials. Many useful secondary explosives have peripheral nitro groups, for instance TNT (trinitrotoluene) is a trinitroaromatic, or RDX (1,3,5-trinitroperhydro-1,3,5-triazine) with three nitro groups attached to a six-member heterocycle. In these materials and in many others, abstraction of nitro groups is believed to be one of the most important steps in the impact-initiation process.[18] In low-velocity initiation, where impacts of a few m/s create moving edge dislocations that generate heat by friction or dislocation pile ups,[19-21] or in shock initiation, where impacts of a km/s or more generate steep shock fronts,[22,23] energy will be preferentially pumped into peripheral functionalities with lower-frequency vibrational modes (doorway modes), such as nitro torsion or scissors.[23-25] When the pumping rate into nitro greatly exceeds the rate of flow out of nitro into other moieties such as phenyl, then highly vibrationally excited nitro groups would be produced in vast quantities.[24,25] Thus highly nonthermal energy distributions with great excesses of nitro excitations might be produced during impacts, that may result in nitro cleavage rates dramatically different from what would be observed in thermal decomposition studies using gradual heating.

7.5 Normal Mode Assignments

mode	classification	MP2	experimental
v36	phenyl	3091.83	
v35	phenyl	3091.56	
vCH-phen (v34)	phenyl	3065.83	3074
v33	phenyl	3057.55	
v32	phenyl	3046.40	
νNO^1 (v31)	subs.	1693.83	1512
v30	phenyl	1582.07	
vCC (v29)	phenyl	1570.99	1590
v28	phenyl	1452.43	
v27	phenyl	1428.43	
v26	phenyl	1397.14	
νNO^2 (v25)	subs.	1338.62	1335
v24	phenyl	1277.93	
γCH (v23)	phenyl	1156.37	1154
v22	phenyl	1147.33	
$\nu C\text{-}N^1$ (v21)	global	1087.28	1098
v20	phenyl	1061.59	
v19	phenyl	1002.52	
βCH (v18)	phenyl	966.64	1000
v17	phenyl	857.94	
v16	phenyl	852.12	
v15	phenyl	834.53	
$\nu C\text{-}N^2$ (v14)	global	806.67	845
v13	phenyl	780.62	
v12	phenyl	717.83	
v11	global	656.14	
v10	global	651.36	
φdef (v9)	phenyl	589.42	605
v8	global	497.41	
v7	phenyl	470.21	
v6	phenyl	395.91	
v5	global	382.22	
v4	phenyl	375.05	
v3	global	250.62	
v2	global	159.75	
v1	global	31.04	

Table 7.1. Nitrobenzene normal mode assignments. Vibrational frequencies and mode classifications of nitrobenzene. The named modes are those that are visible in the experiment while others are only numbered. The MP2 frequencies are in wavenumbers (cm^{-1}). If a mode has displacement primarily on the nitro or phenyl group it is classified as nitro or pheyl respectively, otherwise it is classified as global.

7.6 Normal Mode Vector Illustrations

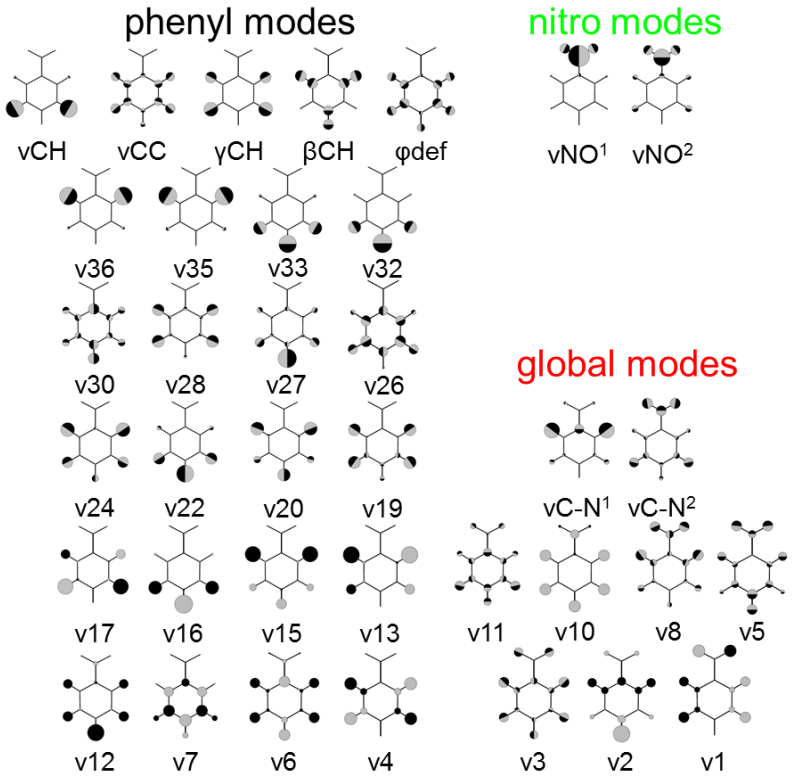

Figure 7.7. Nitrobenzene normal mode vector illustrations Classified normal modes of nitrobenzene computed using MP2 perturbation theory with the 6-31G basis set. Relative sphere size indicates relative displacement and the sphere colors represent the relative displacement direction.

7.7 References

1. Cahill, D. G.; Ford, W. K.; Goodson, K. E.; Mahan, G. D.; Majumdar, A.; Maris, H. J.; Merlin, R.; Phillpot, S. R., Nanoscale Thermal Transport. *Journal of Applied Physics* **2003,** *93*, 793-818.

2. Seong, N.-H.; Fang, Y.; Dlott, D. D., Vibrational Energy Dynamics of Normal and Deuterated Liquid Benzene. *Journal of Physical Chemistry A* **2009,** *113*, 1445-1452.

3. Graham, P. B.; Matus, K. J. M.; Stratt, R. M., The Workings of a Molecular Thermometer: The Vibrational Excitation of Carbon Tetrachloride by a Solvent. *Journal of Chemical Physics* **2004,** *121*, 5348-5354.

4. Deàk, J. C.; Iwaki, L. K.; Dlott, D. D., Vibrational Energy Relaxation of Polyatomic Molecules in Liquids: Acetonitrile. *Journal of Physical Chemistry* **1998,** *102*, 8193-8201.

5. Deàk, J. C.; Iwaki, L. K.; Dlott, D. D., Vibrational Energy Redistribution in Polyatomic Liquids: Ultrafast Ir-Raman Spectroscopy of Nitromethane. *Journal of Physical Chemistry A* **1999,** *103*, 971-979.

6. Deàk, J. C.; Iwaki, L. K.; Rhea, S. T.; Dlott, D. D., Ultrafast Infrared-Raman Studies of Vibrational Energy Redistribution in Polyatomic Liquids. *Journal of Raman Spectroscopy* **2000,** *31*, 263-274.

7. Iwaki, L. K.; Deàk, J. C.; Rhea, S. T.; Dlott, D. D., Vibrational Energy Redistribution in Polyatomic Liquids: Ultrafast Ir-Raman Spectroscopy. In *Ultrafast Infrared and Raman Spectroscopy*, Fayer, M. D., Ed. Marcel Dekker: New York, 2001; pp 541-592.

8. El'kin, P.; Pulin, V.; Kosterina, E., Structural Dynamic Models and Vibrational Spectra of Nitrobenzene and Nitropyridines. *Journal of Applied Spectroscopy* **2005,** *72*, 483-487.

9. Deàk, J. C.; Rhea, S. T.; Iwaki, L. K.; Dlott, D. D., Vibrational Energy Relaxation and Vibrational Spectral Diffusion in Liquid Water and Deuterated Water. *Journal of Physical Chemistry A* **2000,** *104*, 4866-4875.

10. Shigeto, S.; Dlott, D. D., Vibrational Relaxation of an Amino Acid in Aqueous Solution. *Chemical Physics Letters* **2007,** *447*, 134-139.

11. Shigeto, S.; Pang, Y.; Fang, Y.; Dlott, D. D., Vibrational Relaxation of Normal and Deuterated Liquid Nitromethane. *Journal of Physical Chemistry B* **2008,** *112*, 232-241.

12. Fang, Y.; Shigeto, S.; Seong, N.-H.; Dlott, D. D., Vibrational Energy Dynamics of Glycine, N-Methyl Acetamide and Benzoate Anion in Aqueous (D_2o) Solution. *Journal of Physical Chemistry A* **2009,** *113*, 75-84.

13. Deàk, J. C.; Iwaki, L. K.; Dlott, D. D., When Vibrations Interact: Ultrafast Energy Relaxation of Vibrational Pairs in Polyatomic Liquids. *Chemical Physics Letters* **1998,** *293*, 405-411.

14. Graener, H.; Laubereau, A., Ultrafast Overtone Excitation for the Study of Vibrational Population Decay in Liquids. *Chemical Physics Letters* **1983,** *102*, 100-104.

15. Iwaki, L. K.; Deàk, J. C.; Rhea, S. T.; Dlott, D. D., Vibrational Energy Redistribution in Liquid Benzene. *Chemical Physics Letters* **1999,** *303*, 176-182.

16. Pein, B. C.; Seong, N.-H.; Dlott, D. D., Vibrational Energy Relaxation of Liquid Aryl-Halides X-C_6h_5 (X = F, Cl, Br, I). *Journal of Physical Chemistry A* **2010,** *114* (39), 10500-10507.

17. Hong, X.; Chen, S.; Dlott, D. D., Ultrafast Mode-Specific Intermolecular Vibrational Energy Transfer to Liquid Nitromethane. *Journal of Physical Chemistry* **1995,** *99*, 9102-9109.

18. Fried, L. E.; Manaa, M. R.; Pagoria, P. F.; Simpson, R. L., Design and Synthesis of Energetic Materials. *Annual Review of Materials Research* **2001,** *31*, 291-321.

19. Coffey, C. S., Phonon Generation and Energy Localiation by Moving Edge Dislocations. *Physical Review B* **1981,** *24*, 6984-6990.

20. Coffey, C. S.; Toton, E. T., A Microscopic Theory of Compressive Wave-Induced Reactions in Solid Explosives. *Journal of Chemical Physics* **1982,** *76*, 949-954.

21. Holmes, W.; Francis, R. S.; Fayer, M. D., Crack Propagation Induced Heating in Crystalline Energetic Materials. *Journal of Chemical Physics* **1999,** *110*, 3576-3583.

22. Tokmakoff, A.; Fayer, M. D.; Dlott, D. D., Chemical Reaction Initiation and Hot-Spot Formation in Shocked Energetic Molecular Materials. *Journal of Physical Chemistry* **1993,** *97* (9), 1901-1913.

23. Dlott, D. D.; Fayer, M. D., Shocked Molecular Solids: Vibrational up Pumping, Defect Hot Spot Formation, and the Onset of Chemistry. *Journal of Chemical Physics* **1990,** *92*, 3798-3812.

24. Dlott, D. D., Fast Molecular Processes in Energetic Materials. In *Energetic Materials: Initiation, Decomposition and Combustion, Part 2*, Politzer, P.; Murray, J. S., Eds. Elsevier: New York, 2003; pp 125-192.

25. Dlott, D. D., Multiphonon up-Pumping in Energetic Materials. In *Overviews of Recent Research on Energetic Materials*, Thompson, D.; Brill, T.; Shaw, R., Eds. World Scientific: Hackensack, New Jersey, 2005; pp 303-333.

Chapter 8: Controlling Vibrational Energy Flow in Alkylbenzenes†

8.1 Introduction

In this Chapter vibrational energy flow in a series of liquid alkylbenzenes is studied. These molecules include toluene, isopropylbenzene (IPB) and *t*-butylbenzene (TBB). For simplicity, they will often be described as a Φ-S structure. Here Φ is the phenyl group (C_6H_5) and S is one of the alkyl substituents CH_3, $CH(CH_3)_2$ or $C(CH_3)_3$ belonging to toluene, IPB and TBB respectively. Each was studied using the materials science approach to determine the rates of S→Φ and Φ→S energy transfer. The work in this chapter will demonstrate possible routes to enhancing energy flow from one end of an alkylbenzene molecule to another which, from the perspective of a "molecular toolbox", could benefit the engineering of molecular-scale devices.

This work was inspired from a classic study where vibronic emission from jet-cooled n-alkylbenzenes was used to understand the effects that the alkyl structure had on phenyl VR processes. In this previous work, Smalley and co-workers[1-3] demonstrated that increasing the alkyl chain length accelerated energy flow from the phenyl group. As mentioned in the Chapter 1, this result could be rationalized in terms of the golden rule where the increased vibrational density of states (DOS) of the longer n-alkyl chains was responsible for the acceleration. However this type of study did not take into account details of molecular structure and how the anharmonic couplings depended on the structure and interatomic distances within the alkyl group. This is a problem because, for example, energy transfer between two nearby moieties seems more likely than between two distant moieties, even when the DOS greatly favors the

†Parts of this chapter are recreated from work previously published as: Pein, B. C.; Sun, Y.; Dlott, D. D., Controlling Vibrational Energy Flow in Liquid Alkylbenzenes *Journal of Physical Chemistry B* **2013**, *117(37)*, 10898.

distant moiety. The proximity of terminal methyl groups in IPB and TBB with each other and the phenyl ring could affect phenyl relaxation. Additionally, Smalley's experiments were measuring VR occurring in an excited electronic state. Comparing VR in an excited electronic state may not be necessarily comparable to that in the ground state.

Here the same approach for initially localizing vibrational energy will be taken that was used in the nitrobenzene study. For each molecule, using quantum chemistry and literature vibrational assignments,[4-7] every mode was classified as either phenyl (Φ), substituent (S) or global (G). Using excitation spectroscopy, pump wavenumbers were then found in the CH-stretching region that maximized the initial localization of vibrational energy onto Φ or S. Using the phenyl and substituent pump wavenumbers the energies in the phenyl, substituent and global modes were measured and then the aggregate energy in these modes was monitored. Thusly a phenyl excitation transferring energy to the substituent and vice versa was observed.

In the nitrobenzene study only the first few picoseconds of VR, which is primarily intramolecular VR (IVR), were studied in order to focus on the effects of molecular structure on energy flow from one end of a molecule to another. Here, intramolecular processes will again be studied and the first couple of picoseconds will be the primary focus where the S→Φ and Φ→S vibrational energy transfer is mainly from IVR.[8-10] It is these shorter-time IVR processes that are the most relevant for modeling molecular devices such as current-carrying molecular wires where the molecules are largely isolated from their surrounding except at point contacts.

The nitrobenzene study presented a surprising observation. There it was found that phenyl-to-nitro (Φ→S) flow was inefficient but that nitro-to-phenyl (S→Φ) flow was entirely nonexistent. Thus nitrobenzene acts as a vibrational energy diode, albeit not a very good or useful one. These results were clearly at odds by what would be predicted by simple DOS

considerations. Instead the observed behavior showed that substituted benzenes could demonstrate hierarchical mode-mode couplings that can effectively shut-off S→Φ or hinder Φ→S energy flow. So in the present study particular attention will be paid to processes that deviate from what DOS considerations alone would predict while keeping in mind what the work by Smalley and co-workers demonstrated.

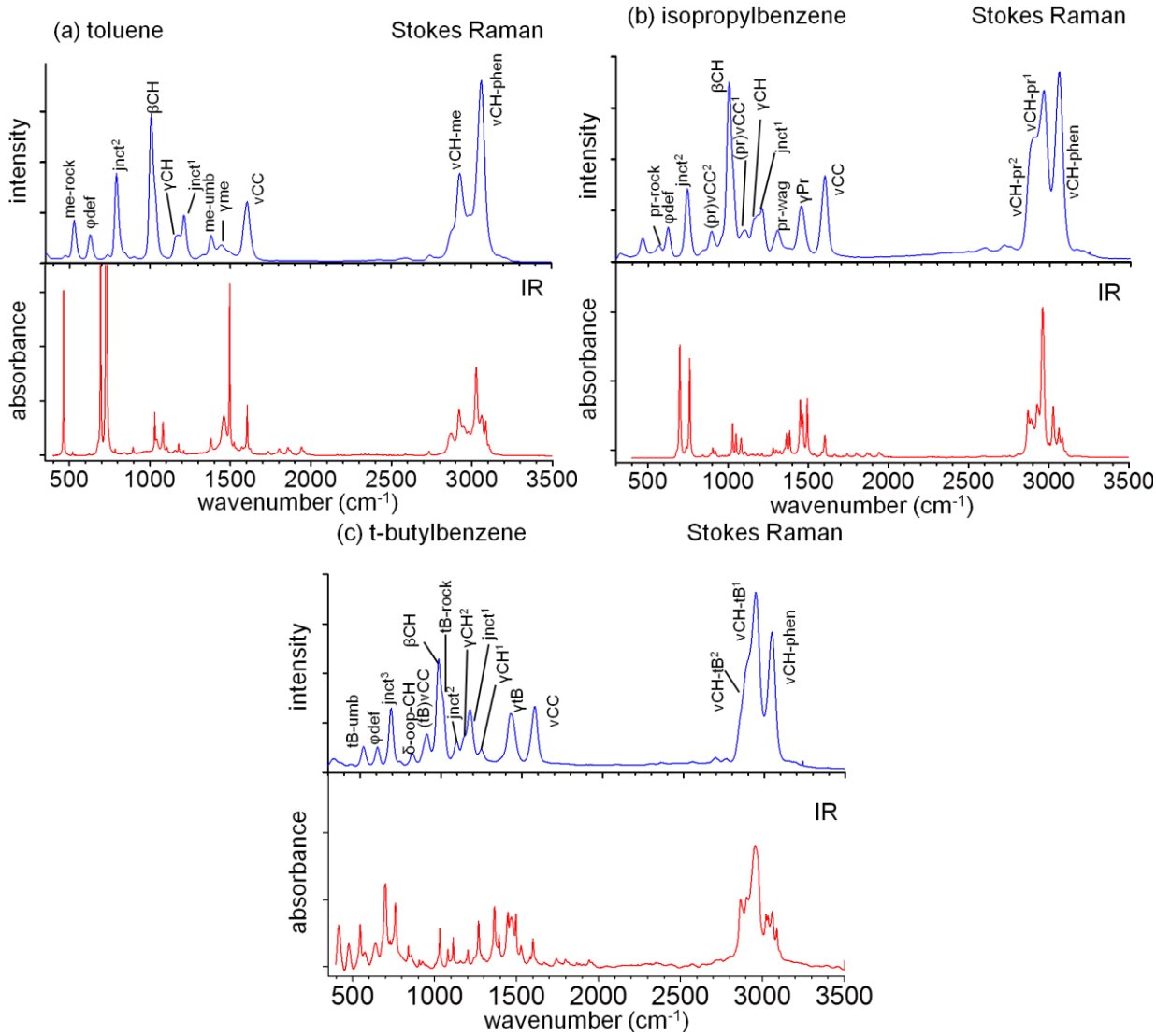

Figure 8.1. Infrared and Raman spectra of alkylbenzenes. Stokes-Raman and infrared spectra of (a) toluene, (b) isopropylbenzene (IPB) and (c) tertbutylbenzene (TBB). Raman spectra were acquired using the picosecond probe pulses giving a resolution of 25 cm^{-1}. IR spectra were acquired using FTIR with 4 cm^{-1} resolution.

8.2 Results

IR and Raman Spectra and Assignments

IR and Stokes-Raman spectra of the three alkylbenzene liquids are shown above in Figures 8.1a-c. The transitions in the Raman spectra designated by assignments were those intense enough to be studied in the IR-Raman spectra. Smaller peaks, shoulders and combination bands that were too weak to observe were not assigned. A full list of assignments, experimental and computed frequencies along with their classifications is given in Section 8.5. The normal modes were computed using MP2 perturbation theory with the 6-31G basis set in the gaussian 09 computational package. The illustrations of each mode are shown in Section 8.6. Toluene has 39 modes of which 11 were observed, IPB has 57 with 14 observed, and TBB has 66 with 15 observed. In toluene, ~25% of the phenyl and ~30% of the methyl and global modes were observed. With IPB, ~30% of the phenyl, ~30% of the propyl and ~20% of the global modes were observed. For TBB, ~35% of the phenyl, ~20% of the butyl and ~20% of the global were observed. Based on the previous ultrafast calorimetry study of benzene and d_6-benzene done by the Dlott laboratory,[8] where 33% of the 44% of the benzene and d_6-benzene vibrations were observed, it is believed each class of mode in each liquid was reasonably well represented regardless of this selection bias.

To clarify the labeling scheme, some mode descriptions are explained: νCH-phen (~3050 cm^{-1}) is the phenyl C-H stretch, νCC (~1600 cm^{-1}) is the phenyl C-C stretch with some ring C-H bend character, junction (jnct) modes (~1200 cm^{-1} and ~700-800 cm^{-1}) are global modes with displacements involving the substituent to phenyl C-C stretch, γCH (~1150-1200 cm^{-1}) are phenyl C-H bends, βCH (~1000 cm^{-1}) is ring breathing and Φdef (~650 cm^{-1}) is a phenyl ring C-C-C deformation. The substituent C-H stretches (~2950-3000 cm^{-1}) and bends (~1350-1450 cm^{-}

^{1}) are labeled as νCH-X and γX where X= methyl for toluene, isopropyl for IPB and *t*-butyl for TBB. There are C-C stretches within the substituents of IPB and TBB called (X)νCC (~900 cm^{-1}). Modes labeled tB-umb and me-umb are umbrella bending motions in TBB and toluene respectively. Note that the me-umb mode is a CH-bending mode whereas the tB-umb mode is a C-(CH_3) bending mode. These modes are analogous if the methyl groups in TBB are viewed as single unified atoms. Other notable modes include global wagging and rocking motions of the ring/substituent, and are labeled accordingly.

In Chapter 7, the modes were classified purely by atomic displacement. This was done to define where in the molecules vibrational energy was localized to. However classifying modes in this way can lead to issues since the magnitude of atomic displacement doesn't necessarily correlate well with the vibrational energy contributed by those atoms. For example, a bend can have more displacement than a stretch however the stretch can have a larger force constant meaning that its energy content doesn't scale with its displacement the same way that the bend does. For this reason, the modes were classified according to their potential energy distribution (PED) rather than purely by displacement. Fortunately, the classifications of the observable modes in nitrobenzene still hold using this type of analysis so the conclusions made there still hold. This was done using the VEDA-4 software package. A wonderful review of the software can be found online.[11] Briefly, the program utilizes vibrational energy distribution analysis (VEDA) to determine each normal mode's PED. The VEDA method transforms the Cartesian normal mode vectors into a new basis of internal 2,3 and 4 body coordinates. The contribution of each internal coordinate basis to the total, or maximum, potential energy of each mode is decomposed to give their PED percentage as shown in Section 8.5. Modes with 80% or more of their potential energy contributed by phenyl or substituent localized coordinates were classified

as phenyl (Φ) or substituent (S) respectively. If there was less than 80% PED in either phenyl or substituent localized coordinates or if there was 80% PED or more in global coordinates the mode was classified as global (G). Note that the PED for a given mode doesn't add up to 100 for all cases since there are small <1% contributions from some coordinates that are not considered.

Excitation Spectroscopy

Figures 8.2a-c show excitation spectra for the three liquids. As a reminder, these plots are 2D projection of the full 3D IR-Raman spectrum at 1 ps delay. They were obtained by frequency-scanning the IR pulses through the CH-stretch absorption regions (which were slightly different for each liquid) while monitoring the anti-Stoke spectra at a delay time of 1 ps. The excitation spectra were anti-Stokes difference spectra with the ambient temperature contributions (at -3 ps) subtracted off. The excitation spectra are indicative of the excitations generated immediately at the end of each IR pulse. For reference, below each waterfall plot the annotated Stokes spectra are shown.

As a reminder, the parent excitations generated by IR pumping were observed along the diagonal. However, along the diagonal there were nonlinear light scattering (NLS) artifacts originating from sum-frequency generation.[12,13] The parent signals decayed with lifetimes T_1, and the artifacts decayed with the apparatus temporal response (~1ps). The most heavily populated daughter modes were highlighted with red vertical dashed lines.

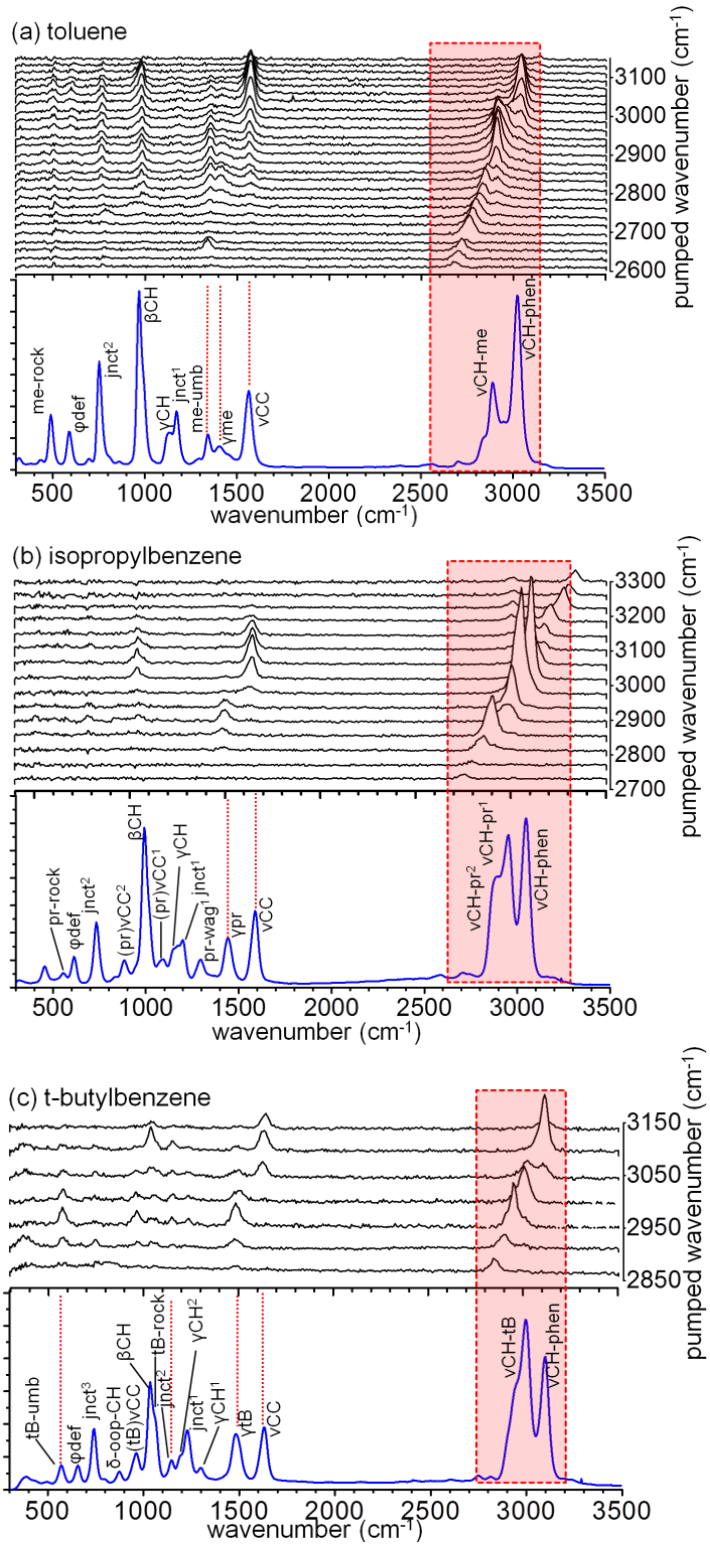

Figure 8.2. Excitation spectra of alkylbenzenes. The most intense transitions of (a) toluene, (b) isopropylbenzene (IPB) and (c) tertbutylbenzene (TBB) are assigned in the Stokes spectra (bottom). The dashed box indicates the tuning range of the IR excitation pulses that created parent excitations. The dashed lines indicate which daughter excitations were populated to the greatest extent.

An oversimplified but useful method to use Figure 8.2 to gauge the amount of excitation produced on the phenyl or substituent moieties is to look at the phenyl ring stretch νCC near 1600 cm^{-1}, and the slightly lower frequency substituent CH-bends γme, γpr and γtB . When the phenyl ring stretches predominate, the parent excitations are primarily phenyl, and when the substituent CH-bends predominate, the parent excitations are primarily substituent.

The pump wavenumber dependence of the daughter vibrations having the greatest population, or occupation number, changes $\Delta n(t = 1\ ps)$ was plotted in Figure 8.3, with the IR spectra superimposed for reference. These results were used to select IR pump wavenumbers (indicated by arrows in Figure 8.3) that maximized the selectivity of phenyl and alkyl substituent pumping.

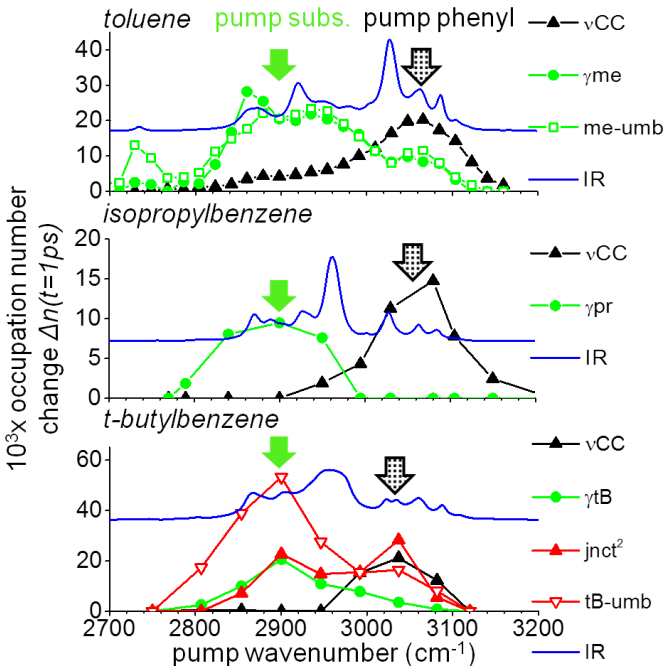

Figure 8.3. Population changes Δn(t) of alkylbenzenes at 1 ps delay. The IR-spectra superimposed for reference. The dotted black arrow indicates the phenyl pump frequency. The solid green arrow indicates the substituent pump frequency.

As shown in Figure 8.3, for toluene, phenyl pumping used 3070 cm^{-1} and substituent pumping used 2940 cm^{-1}. With toluene substituent pumping was quite selective, generating little phenyl excitation, but phenyl pumping was not as selective, since phenyl pumping also generated substituent excitations. For IPB, phenyl pumping used 3060 cm^{-1} and substituent pumping used 2950 cm^{-1} and both were highly selective. For TBB, phenyl pumping used 3050 cm^{-1} and substituent pumping used 2960 cm^{-1}. Phenyl pumping generated little substituent excitation and substituent pumping generated little phenyl excitation, but no matter where the IR pulses were tuned, a considerable amount of global excitations jnct[2] and tB-umb were produced. Thus in TBB, $\Phi \rightarrow S$ and $S \rightarrow \Phi$ energy transfer will always occur against a background of global excitations. As this discussion makes clear, complete specificity of phenyl or substituent pumping could not be achieved with toluene or TBB, but for simplicity, in the next section phenyl or substituent pumping will be referred to, keeping in mind the specificity caveats discussed here.

Anti-Stokes Transients

Figures 8.4-8.6 show the results of time-dependent IR-Raman experiments using either phenyl or the substituent (methyl) pumping pulses for all three liquids. In each IR-Raman spectrum, note the nonlinear time axis on the right edge, which emphasizes the shorter time delays, the dashed lines indicating the pump pulse wavenumbers, and the insets focusing on daughter vibrations <1700 cm^{-1}. The signals at the pump pulse wavenumber at the shorter time delays near $t = 0$ arise from both parent excitations and NLS artifacts. In the parent region ≥1 ps, vibrational excitations predominate.

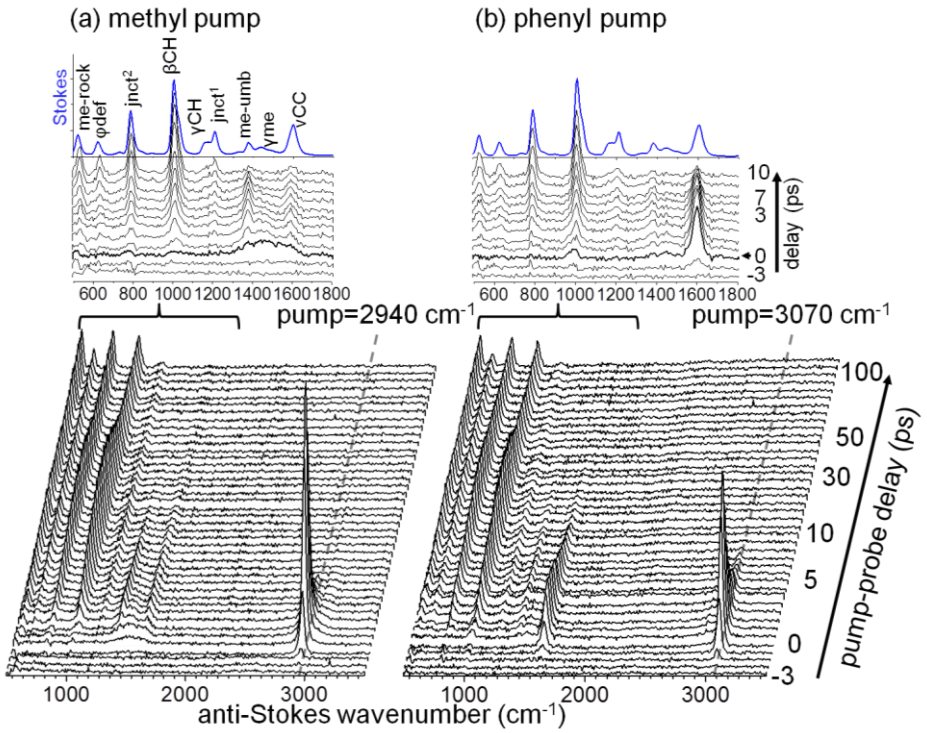

Figure 8.4. IR-Raman spectra of toluene. Results using the (a) methyl pump and (b) phenyl pump are shown.

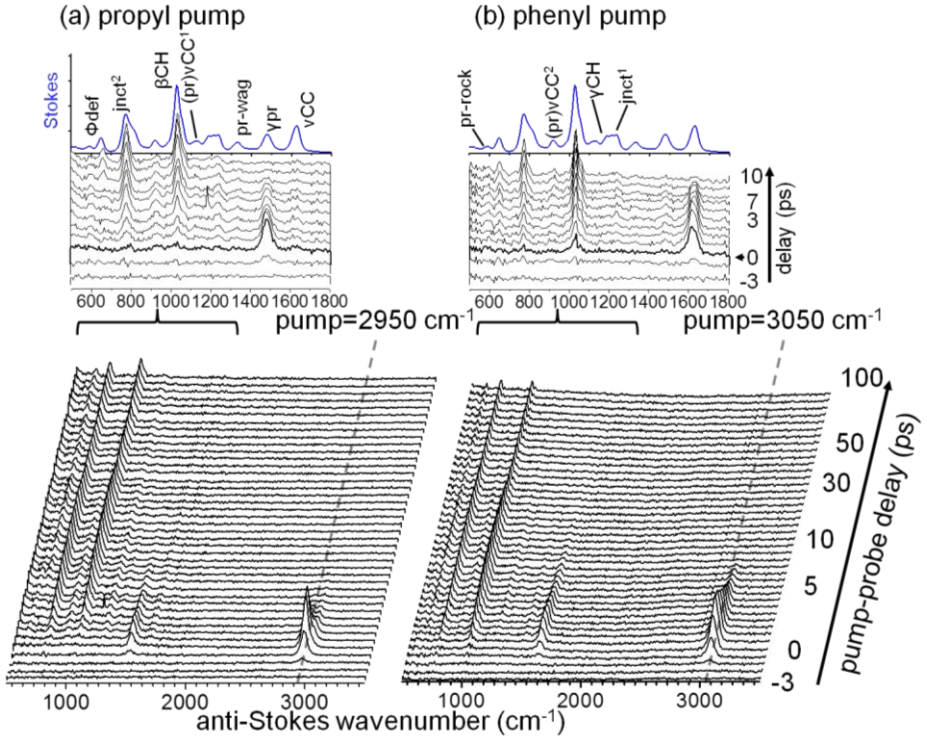

Figure 8.5. IR-Raman spectra of isopropylbenzene. Results using the (a) propyl pump and (b) phenyl pump are shown.

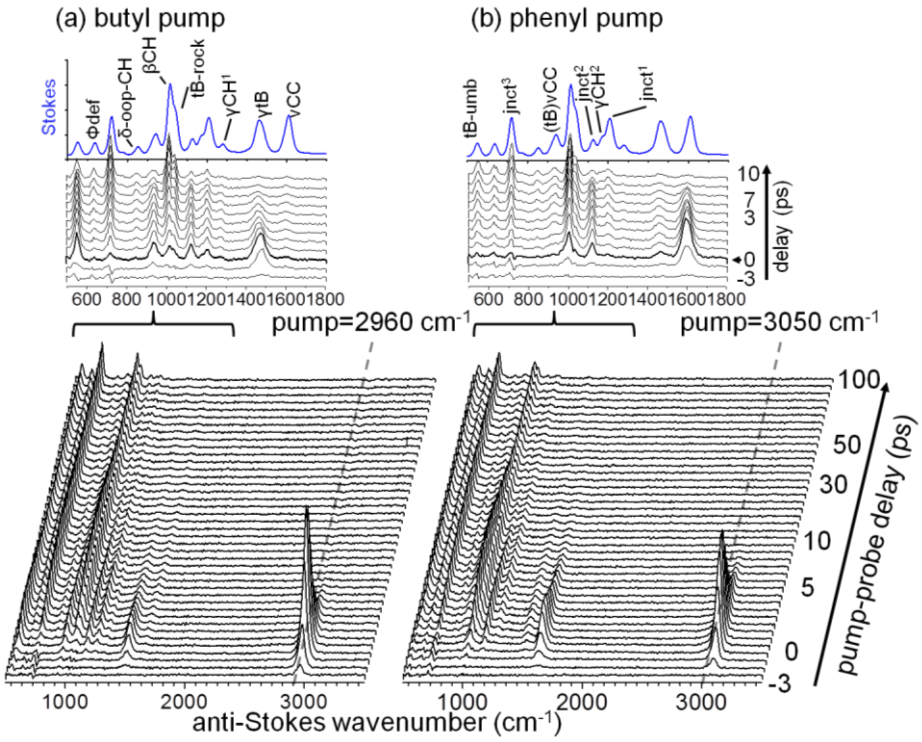

Figure 8.6. IR-Raman spectra of t-butylbenzene. Results using the (a) butyl pump and (b) phenyl pump are shown. The signal at the pump wavenumber in Figures 8.4-8.6 arises from the parent excitation and a nonlinear light scattering artifact which mostly disappeared at times > 1 ps. The *insets* show the rise of daughter excitations during the first 10 ps. Stokes Raman spectra are displayed to help gauge relative Raman cross-sections of each mode.

Vibrational Energy Densities

The anti-Stokes intensity data in Figures 8.4-8.6, can be combined with Stokes intensity data and converted into vibrational energy densities. The results are shown in Figures 8.7a-c, where each bar was color-coded to represent phenyl, substituent or global modes.

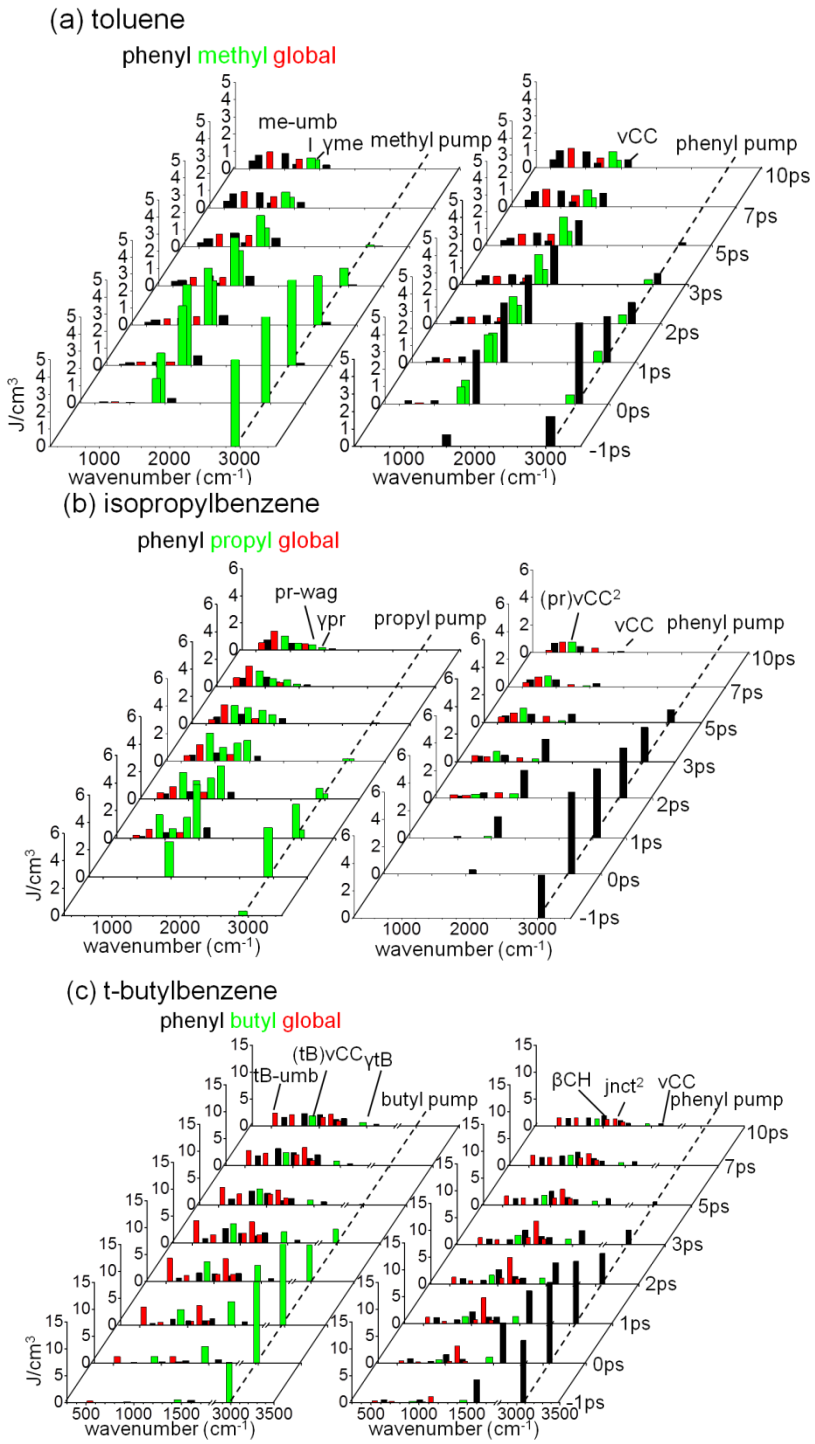

Figure 8.7. Alkylbenzene transient energy densities. The results are shown for (a) toluene (b) isopropylbenzene (IPB) (c) tertbutylbenzene (TBB) with substituent (left) and phenyl (right) pumping. The dashed lines indicate the parent excitation wavenumber.

Spatially-Resolved Energy Densities

The individual mode energies in Figure 8.7 were summed to indicate the time-dependent aggregate observed energies in the Φ, S or G modes, as shown in Figure 8.8. Keep in mind that as discussed above, Φ or S pumping was not always completely selective. In order to assess S→Φ or Φ→S transfer efficiencies, the shorter-time data, say 0-3 ps, that represents IVR between phenyl and substituent needs to be concentrated on. Energy whose rise is correlated with the fall of the parent excitation, the initially localized excitation, should be the primary focus here.

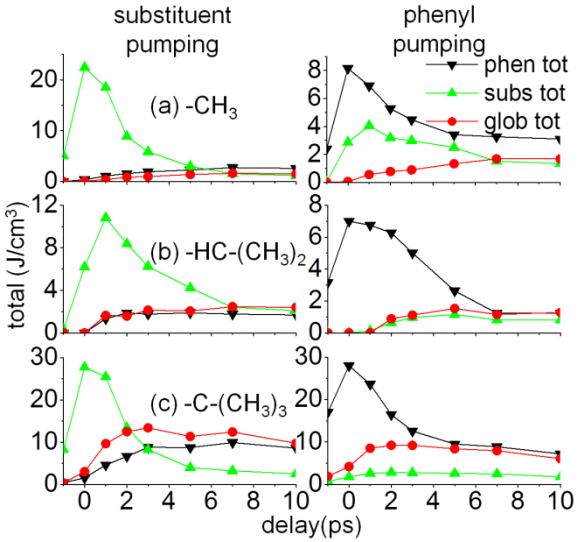

Figure 8.8. Alkylbenzene aggregate transient energy densities. With phenyl pumping (right), the efficiencies of phenyl to substituent (Φ→S) transfer were low and approximately the same for toluene, isopropylbenzene and *t*-butylbenzene. (With phenyl pumping in toluene, most of the substituent energy was produced by direct IR absorption into nearby methyl transitions rather than phenyl-to-methyl energy transfer). With substituent pumping (left), the efficiency of substituent-to-phenyl (S→Φ) energy transfer increased with substituent size.

With toluene (Figure 8.8a), with S pumping there was very little S→Φ (or S→G) energy transfer. With Φ pumping a significant amount of S is seen, but much of it was generated by the pump pulses rather than an IVR process. Thus there was little Φ→S transfer in toluene. It's believed that Φ→S transfer was not entirely absent, based on the way the S energy peaks at a

slightly later time than the Φ energy in the right hand side of Figure 8.8a. The Φ→G transfer is also low efficiency.

With IPB (Figure 8.8b) the assessment was simplified, since both Φ and S pumping processes were highly selective. The S→Φ transfer, while still not particularly efficient, was several times greater than what was seen in toluene, and about the same as S→G. The Φ→S and Φ→G processes were comparable in efficiency to S→Φ transfer, and about the same efficiency as in toluene.

With TBB (Figure 8.8c), the S→Φ and S→G processes were quite a bit more efficient than what was seen in toluene or TBB. The Φ→S process was similar in efficiency to IPB and probably more efficient than in toluene. The S→G and Φ→G processes were quite a bit more efficient than in either toluene or IPB.

Thus for the S→Φ transfer, the efficiency increased as the substituent grew larger. The Φ→S process efficiency was generally low, and about the same in toluene, IPB and TBB. Transfer to the G modes, from either S or Φ, grew in efficiency with increasing substituent size.

8.3 Discussion

IVR between phenyl and substituent must compete with other VR processes. In IR-Raman studies of methyl groups, for instance in ACN, as shown in Chapter 6 and in previous works,[14] the predominant methyl CH-stretch relaxation was to the CH-bending vibrations, then into global modes such as C-C stretching, and finally out into the bath. In IR-Raman studies of benzene,[8] the predominant phenyl CH-stretch relaxation was to ring modes in the 1000-1600 cm^{-1} range, then to deformation modes in the 500-1000 cm^{-1} range and then out into the bath.

With toluene, little vibrational energy transfer from methyl to phenyl or vice versa is seen during the first few picoseconds. Instead the vibrational energy tended to stay on the methyl or

phenyl groups until it was dissipated into the solvent bath presumably at longer times. In fact with toluene, IPB and TBB, only a small fraction of the phenyl energy was transferred to the substituent, regardless of the substituent size.

However the opposite is not true. The efficiency of substituent to phenyl transfer increases with substituent size, and in the case of TBB, S→Φ transfer was noticeably more efficient than the reverse Φ→S process. This is a dramatic observation as it is exactly opposite what would be predicted on the basis of Smalley's n-alkylbenzene work[1-3] that correlated accelerated Φ relaxation with an increased DOS. This result is not necessarily unexpected. Aside from the structural differences in IPB and TBB, whose intramolecular interactions may not be compared to their n-alkyl counterparts, the dispersed fluorescence technique observed dynamics in excited electronic states, indicated by spectral broadening, that are not necessarily comparable to the ground state studied here. Furthermore, the origin of the broadening may not have entirely originated from IVR as indicated through simulations by Brumer.[15,16] Thus the anharmonic couplings between the modes need to be looked at in order to understand the way S→Φ energy transfer increases with increasing substituent size and mass. The simplest explanation one can off without such information is that when a heavier substituent such as *t*-butyl vibrates, it will more effectively couple to phenyl atomic displacements than a lighter substituent such as methyl.

More insights into the S→Φ and Φ→S processes in TBB can be obtained by noticing that global mode excitations were much more prominent in TBB than in IPB and toluene. As shown in the TBB results of Figure 8.7c, when phenyl was pumped the result was a significant amount of jnct^2 excitations. When the substituent was pumped, both jnct^2 and tB-umb excitations were produced. As shown in Figure 8.9, jnct^2 is a butyl-phenyl bending mode and tB-umb is an umbrella mode of the three methyl groups bonded to the central carbon atom. In both cases,

substituent motion is accompanied by phenyl group deformation. As these normal modes illustrate, motions of the heavier *t*-butyl group induce more amplitude onto the phenyl group than with the lighter substituents. Thus it is suggested that molecules with efficient S→Φ transfer could be recognized as those where global mode excitations created during the initial stages of parent relaxation.

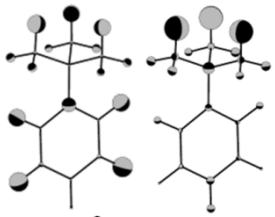

Figure 8.9. Global modes of *t*-butylbenzene excited by substituent. Normal mode vector illustrations of two global modes substantially excited when pumping the substituent of *t*-butylbenzene. The sphere sizes indicate the magnitude of the displacement and the colors represent the direction.

8.4 Conclusions

Here the materials science approach to VR is used to understand S→Φ and Φ→S vibrational energy flow in liquid-state alkylbenzenes. In the three systems studied here, toluene, IPB and TBB, there was a small amount of Φ→S transfer, and the efficiency of Φ→S transfer was about the same regardless of the substituent. However the efficiency of S→Φ transfer increased substantially as the substituent size increased. The S→Φ transfer was reasonably efficient in TBB, which was opposite to what would be predicted on the basis of the DOS in the phenyl and subsituent CH-stretch regions. When the larger substituents vibrate, the larger aggregate masses make it easier to induce vibrational motions of the phenyl group.

It is very interesting to understand how to arrange molecular structures that promote unidirectional vibrational energy flow such as in the case of nitrobenzene. In the present studies of alkylbenzenes, it is observed that the Φ→S process is inefficient and is not affected much by

substituent, whereas the S→Φ process can be tuned and made more efficient by increasing the substituent mass. In other words this is a method to increase the ratio of forward to backward vibrational energy transfer.

8.5 Normal Mode Assignments

toluene vibrational frequencies

mode	MP2	experimental	PED(%)	classification
v39	3059.16		phenyl(97)	phenyl
vCH-phen (v38)	3047.70	3055	phenyl(96)	phenyl
v37	3039.88		phenyl(96)	phenyl
v36	3026.63		phenyl(91)	phenyl
v35	3025.26		phenyl(97)	phenyl
v34	3011.92		subs.(98)	subs.
v33	2996.39		subs.(97)	subs.
vCH-me (v32)	2920.94	2920	subs.(97)	subs.
vCC (v31)	1588.04	1600	phenyl(96)	phenyl
v30	1567.12		phenyl(83) global(8) subs.(4)	phenyl
v29	1470.11		subs.(89)	subs.
v28	1469.46		phenyl(80) global(20)	phenyl
γme (v27)	1459.92	1440	subs.(99)	subs.
v26	1419.57		phenyl(83) subs.(7)	phenyl
me-umb (v25)	1384.31	1380	subs.(94)	subs.
v24	1379.60		phenyl(92) subs.(4)	phenyl
v23	1290.49		phenyl(92)	phenyl
jnct[1] (v22)	1192.21	1205	global(66) phenyl(26) subs.(4)	global
γCH (v21)	1164.36	1175	phenyl(97)	phenyl
v20	1145.28		phenyl(96)	phenyl
v19	1073.25		phenyl(81) subs.(11)	phenyl
v18	1021.20		subs.(94)	subs.
v17	1009.19		phenyl(93)	phenyl
v16	970.10		subs.(77) phenyl(21)	global
βCH(v15)	965.68	1005	phenyl(81) global(19)	phenyl
v14	836.85		phenyl(91) global(6)	phenyl
v13	833.41		phenyl(95)	phenyl
v12	810.75		phenyl(94)	phenyl
v11	787.48		phenyl(99)	phenyl
jnct[2] (v10)	763.72	795	global(65) phenyl(26)	global
v9	682.18		phenyl(92)	phenyl
φdef (v8)	599.74	608	phenyl(92)	phenyl
v7	498.57		phenyl(82) global(18)	phenyl
me-rock (v6)	474.95	510	phenyl(82) global(13)	phenyl
v5	425.74		global(82) phenyl(15)	global
v4	375.75		phenyl(90) global(7)	phenyl
v3	324.79		global(88) phenyl(4)	global
v2	195.11		global(75) phenyl(16)	global
v1	56.6		subs.(99)	subs.

Table 8.1. Alkylbenzene normal mode assignments.

isopropylbenzene (IPB) vibrational frequencies

mode	MP2	experimental	PED(%)	classification
v57	3071.97		phenyl(95)	phenyl
vCH-phen (v56)	3060.52	3060	phenyl(100)	phenyl
v55	3053.25		phenyl(100)	phenyl
v54	3042.81		phenyl(99)	phenyl
v53	3037.59		phenyl(100)	phenyl
v52	3025.02		subs.(96)	subs.
v51	3023.93		subs.(99)	subs.
vCH-pr[1] (v50)	3016.39	3000	subs.(99)	subs.
v49	3013.09		subs.(99)	subs.
vCH-pr[2] (v48)	2933.1	2930	subs.(99)	subs.
v47	2931.38		subs.(99)	subs.
v46	2919.41		subs.(99)	subs.
vCC (v45)	1590.16	1620	phenyl(83) global(9)	phenyl
v44	1570.78		phenyl(87) global(9)	phenyl
v43	1487.58		subs.(82) global(11)	subs.
v42	1482.32		subs.(87) global(4)	subs.
v41	1471.86		subs.(91) global(4)	subs.
v40	1470.66		global(76) phenyl(19)	global
γpr (v39)	1466.01	1480	subs.(92) global(2)	subs.
v38	1431.36		global(47) phenyl(44)	global
v37	1395.51		phenyl(80) global(8) subs.(2)	phenyl
v36	1393.75		subs.(95)	subs.
v35	1374.92		subs.(93) global(2)	subs.
v34	1333.27		global(75) phenyl(14) subs.(4)	global
pr-wag (v33)	1316.56	1330	subs.(90)	subs.
v32	1282.84		phenyl(70) global(21) subs.(2)	global
jnct[1] (v31)	1205.33	1225	global(64) subs.(15) phenyl(13)	global
γCH (v30)	1170.37	1170	phenyl(95)	phenyl
v29	1150.91		phenyl(87) global(3)	phenyl

Table 8.1 (cont.). Alkylbenzene normal mode assignments.

isopropylbenzene (IPB) vibrational frequencies (cont.)

mode	MP2	experimental	PED(%)	classification
v28	1145.42		global(71) phenyl(12) subs.(7)	global
(pr)vCC[1] (v27)	1109.95	1110	subs.(81) global(10)	subs.
v26	1074.92		global(58) phenyl(30) subs.(3)	global
v25	1039.03		global(69) phenyl(19) subs.(5)	global
v24	1010.31		phenyl(64) global(26) subs.(4)	global
βCH (v23)	968.73	1025	phenyl(85) global(10)	phenyl
v22	947.37		subs.(95)	subs.
v21	905.97		subs.(83) global(9)	subs.
(pr)vCC[2] (v20)	884.82	920	subs.(81) global(19)	subs.
v19	843.45		phenyl(93)	phenyl
v18	838.16		phenyl(97)	phenyl
v17	821.61		phenyl(94)	phenyl
v16	790.69		phenyl(95)	phenyl
jnct[2] (v15)	725.07	776	global(78) phenyl(14)	global
v14	703.22		phenyl(88) global(3)	phenyl
φdef (v13)	600.48	660	phenyl(92)	phenyl
v12	569.73		phenyl(51) global(33) subs.(7)	global
pr-rock(v11)	541.63	590	global(84) phenyl(7)	global
v10	459.57		global(94)	global
v9	447.16		global(86) subs.(5)	global
v8	377.42		phenyl(97)	phenyl
v7	299.09		global(45) phenyl(43) subs.(4)	global
v6	294.62		global(85) phenyl(2)	global
v5	264.1		subs.(94)	subs.
v4	237.91		global(96)	subs.
v3	207.22		global(89) phenyl(5)	global
v2	120.51		global(93)	global
v1	41.33		global(93)	global

Table 8.1 (cont.). Alkylbenzene normal mode assignments.

tertbutylbenzene (TBB) vibrational frequencies

mode	MP2	experimental	PED(%)	classification
v66	3081.08		phenyl(98)	phenyl
v65	3067.96		phenyl(99)	phenyl
vCH-phen(v64)	3057.83	3080	phenyl(99)	phenyl
v63	3048.49		phenyl(99)	phenyl
v62	3041.67		phenyl(99)	phenyl
v61	3021.31		subs.(96)	subs.
v60	3020.41		subs.(100)	subs.
v59	3015.63		subs.(100)	subs.
vCH-tB(v58)	3011.91	2980	subs.(100)	subs.
v57	3006.06		subs.(100)	subs.
v56	3005.94		subs.(100)	subs.
v55	2928.45		subs.(100)	subs.
v54	2924.12		subs.(100)	subs.
v53	2924.06		subs.(100)	subs.
vCC(v52)	1586.48	1602	phenyl(96)	phenyl
v51	1565.31		phenyl(92) subs.(2)	phenyl
v50	1495.93		subs.(100)	subs.
γtB(v49)	1483.84	1465	subs.(96)	subs.
v48	1482.44		subs. (76) phenyl(12) global(6)	global
v47	1473.14		subs.(52) phenyl(43) global(2)	global
v46	1464.36		subs.(72) phenyl(24) global(1)	global
v45	1463.18		subs.(90)	subs.
v44	1460.2		subs.(97)	subs.
v43	1422.99		phenyl(93) subs.(7)	phenyl
v42	1400.88		subs.(98)	subs.
v41	1386.46		phenyl(93) subs.(6)	phenyl
v40	1371.13		subs.(91) phenyl(7)	subs.
v39	1370.85		subs.(99)	subs.
γCH^{1} (v38)	1298.53	1274	phenyl(90) subs.(8)	phenyl
$jnct^{1}$ (v37)	1269.2	1204	subs.(69) global(22) phenyl(7)	global
v36	1214.78		subs.(77) phenyl(19) global(1)	global
v35	1213.4		subs.(95) phenyl(3)	subs.
γCH^{2} (v34)	1179.57	1180	phenyl(96)	phenyl

Table 8.1 (cont.). Alkylbenzene normal mode assignments.

tertbutylbenzene (TBB) vibrational frequencies (cont.)

mode	MP2	experimental	PED(%)	classification
v33	1150.75		phenyl(99)	phenyl
jnct^{2} (v32)	1099.55	1122	phenyl(45) subs.(44) global(14)	global
v31	1073.92		phenyl(88) subs.(9)	phenyl
v30	1023.28		subs.(98)	subs.
v29	1016.09		subs.(78) phenyl(21)	global
tB-rock(v28)	1013.17	1040	phenyl(78) subs.(17) global(4)	global
βCH(v27)	966.72	1010	phenyl(95)	phenyl
v26	935.2		subs.(93)	subs.
(tB)vCC (v25)	928.31	935	subs.(93)	subs.
v24	918.98		subs.(98)	subs.
v23	842.5		phenyl(95)	phenyl
δ-oop-CH (v22)	841.13	850	phenyl(97)	phenyl
v21	828.67		subs.(62) phenyl(24) global(8)	global
v20	825.69		phenyl(96) global(2)	phenyl
v19	789.98		phenyl(96)	phenyl
v18	705.43		phenyl(91)	phenyl
jnct^{3} (v17)	685.41	720	phenyl(43) subs.(31) global(21)	global
Φdef(v16)	599.85	630	phenyl(94) subs.(3)	phenyl
v15	578.75		subs.(52) phenyl(32) global(13)	global
tB-umb(v14)	514.77	546	subs.(74) phenyl(16) global(7)	global
v13	461.06		phenyl(54) subs.(26) global(17)	global
v12	445.54		subs.(94) phenyl(3)	subs.
v11	379.27		subs.(48) phenyl(45)	global
v10	374.91		subs.(77) phenyl(14)	global
v9	339.53		phenyl(35) subs.(53) global(8)	global
v8	334.09		subs.(53) phenyl(43)	global
v7	306.66		phenyl(46) subs.(46) global(3)	global
v6	306.51		phenyl(71) subs.(26) global(1)	global
v5	274.5		subs.(92) phenyl(5) global(4)	subs.
v4	235.56		subs.(77) phenyl(22) global(1)	global
v3	222.58		subs.(78) phenyl(21)	global
v2	119.93		global(57) subs.(32) phenyl(6)	global
v1	50.17		global(96)	global

Table 8.1 (cont.). Alkylbenzene normal mode assignments. Vibrational frequencies and mode classifications of toluene, isopropylbenzene (IPB) and *t*-butylbenzene (TBB). The named modes are those that are visible in the experiment while others are only numbered. The MP2 frequencies are in wavenumbers (cm^{-1}). The potential energy distribution percentages (PED(%)) are indicated in the parentheses. If a mode had ≥80% of its energy distributed to the phenyl or substituent, it was classified as phenyl or substituent respectively. Otherwise, it was classified as global.

8.6 Normal Mode Vector Illustrations

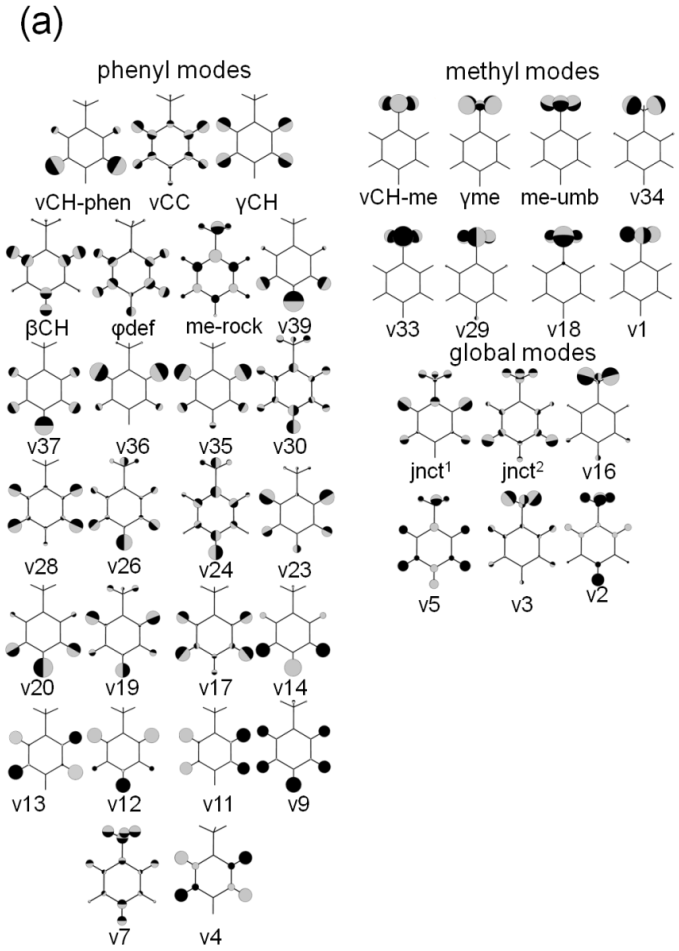

Figure 8.10. Alkylbenzene normal mode vector illustrations.

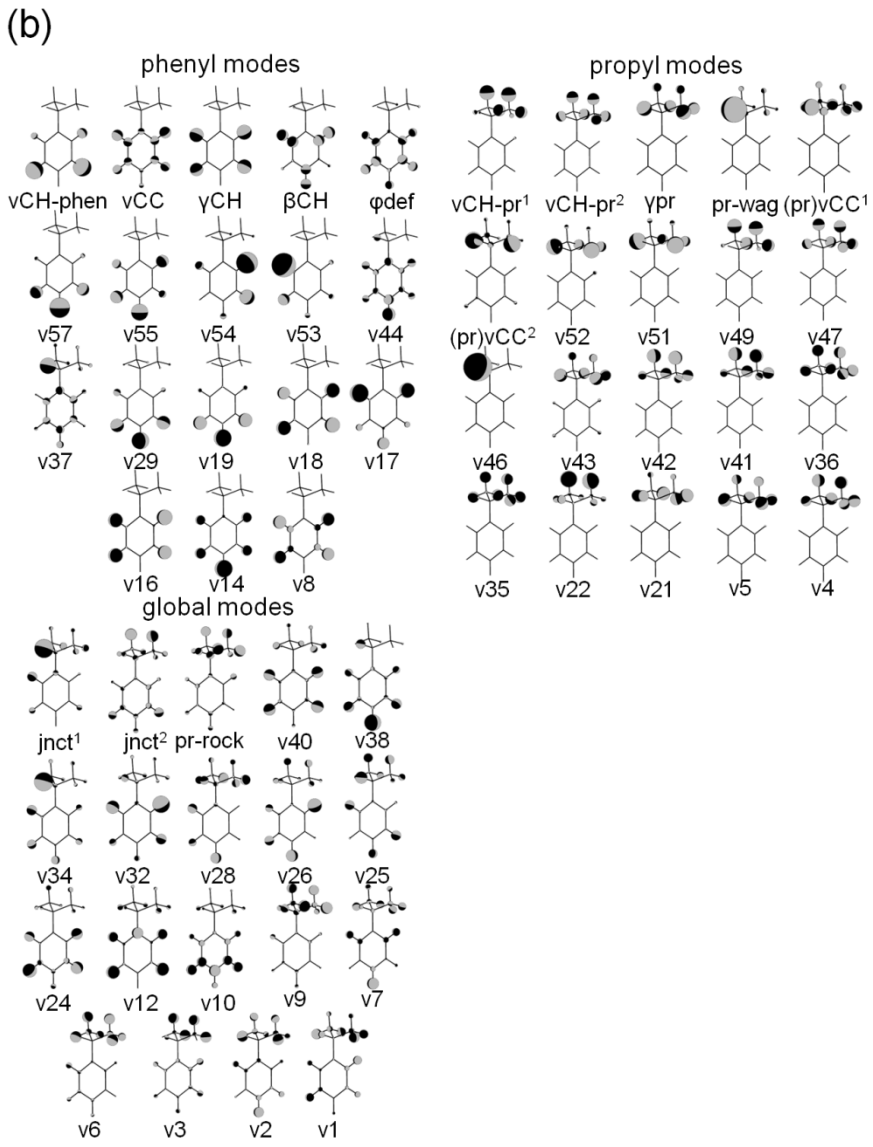

Figure 8.10 (cont.). Alkylbenzene normal mode vector illustrations.

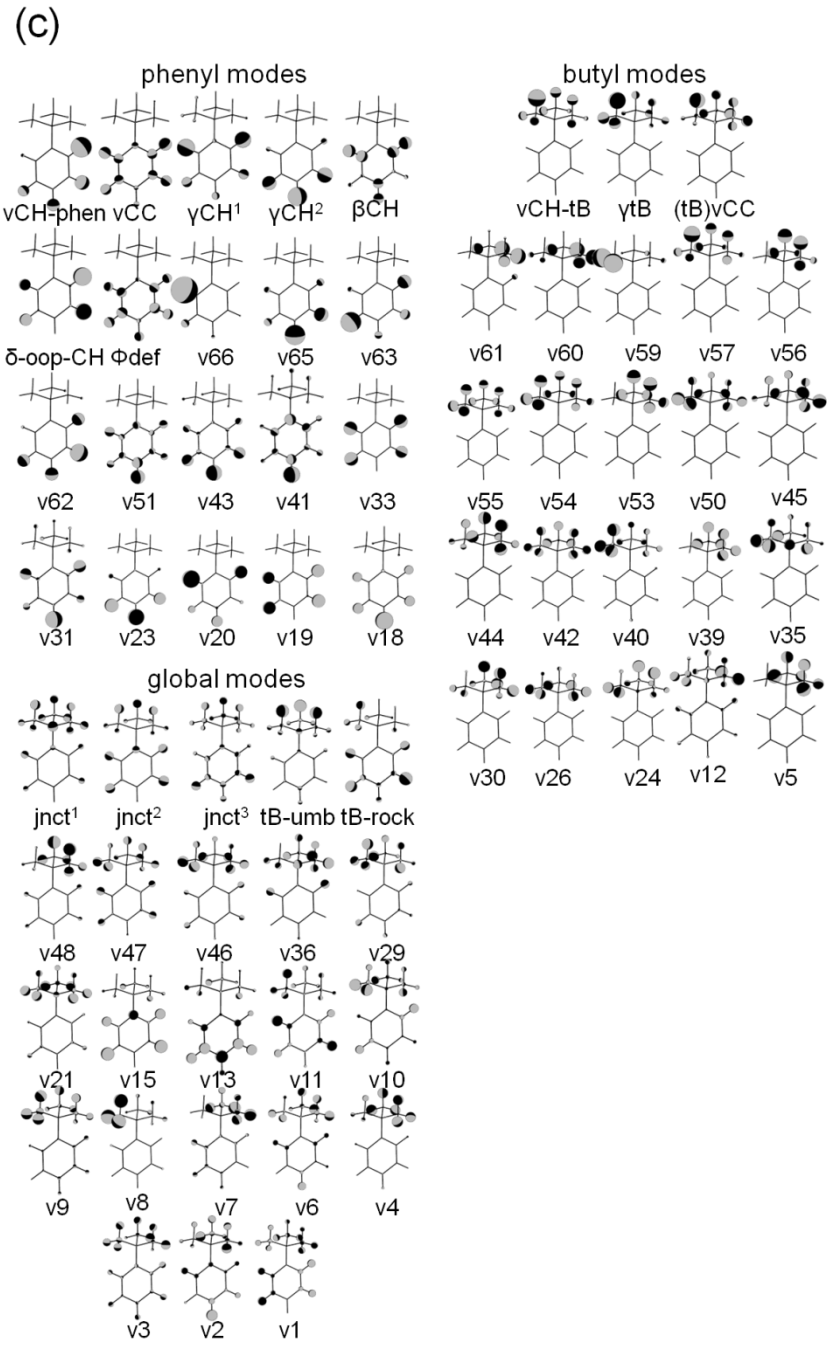

Figure 8.10 (cont.). Alkylbenzene normal mode vector illustrations. Classified normal modes of (a) toluene, (b) isopropylbenzene (IPB) and (c) tertbutylbenzene (TBB) computed using MP2 perturbation theory with the 6-31G basis set. Relative sphere size indicates relative displacement while the grey and white fill represents the displacement direction.

8.7 References

1. Hopkins, J. B.; Powers, D. E.; Smalley, R. E., Vibrational-Relaxation in Jet-Cooled Alkylbenzenes .1. Absorption-Spectra. *Journal of Chemical Physics* **1980,** *72* (9), 5039-5048.

2. Hopkins, J. B.; Powers, D. E.; Mukamel, S.; Smalley, R. E., Vibrational-Relaxation in Jet-Cooled Alkylbenzenes .2. Fluorescence-Spectra. *Journal of Chemical Physics* **1980,** *72* (9), 5049-5061.

3. Hopkins, J. B.; Powers, D. E.; Smalley, R. E., Vibrational-Relaxation in Jet-Cooled Alkyl Benzenes .3. Nanosecond Time Evolution. *Journal of Chemical Physics* **1980,** *73* (2), 683-687.

4. Fishman, A. I.; Noskov, A. I.; Remizov, A. B.; Chachkov, D. V., Vibrational Spectra and Structure of Isopropylbenzene. *Spectrochimica Acta Part a-Molecular and Biomolecular Spectroscopy* **2008,** *71* (3), 1128-1133.

5. Yamakita, Y.; Isogai, Y.; Ohno, K., Large Raman-Scattering Activities for the Low-Frequency Modes of Substituted Benzenes: Induced Polarizability and Stereo-Specific Ring-Substituent Interactions. *Journal of Chemical Physics* **2006,** *124* (10).

6. Morrison, V. J.; Laposa, J. D., Luminescence of Toluene and Deuterium-Substituted Toluenes at 77degreesk in Polycrystalline Methylcyclohexane. *Spectrochimica Acta Part a-Molecular and Biomolecular Spectroscopy* **1976,** *32* (3), 443-454.

7. Varsányi, G. r.; Láng, L., *Assignments for Vibrational Spectra of Seven Hundred Benzene Derivatives*. Wiley: New York,, 1974.

8. Seong, N.-H.; Fang, Y.; Dlott, D. D., Vibrational Energy Dynamics of Normal and Deuterated Liquid Benzene. *The Journal of Physical Chemistry A* **2009,** *113* (8), 1445-1452.

9. Pein, B. C.; Seong, N. H.; Dlott, D. D., Vibrational Energy Relaxation of Liquid Aryl-Halides X-C6h5 (X = F, Cl, Br, I). *Journal of Physical Chemistry A* **2010,** *114* (39), 10500-10507.

10. Heckscher, M. M.; Sheps, L.; Bingemann, D.; Crim, F. F., Relaxation of the C-H Stretching Fundamental Vibrations of Chi3, Ch2i2, and Ch3i in Solution. *Journal of Chemical Physics* **2002,** *117* (19), 8917-8925.

11. Jamroz, M. H., Vibrational Energy Distribution Analysis (Veda): Scopes and Limitations. *Spectrochimica Acta Part a-Molecular and Biomolecular Spectroscopy* **2013,** *114*, 220-230.

12. Pakoulev, A.; Wang, Z. H.; Dlott, D. D., Vibrational Relaxation and Spectral Evolution Following Ultrafast Oh Stretch Excitation of Water. *Chemical Physics Letters* **2003,** *371* (5-6), 594-600.

13. Pakoulev, A.; Wang, Z. H.; Pang, Y. S.; Dlott, D. D., Vibrational Energy Relaxation Pathways of Water. *Chemical Physics Letters* **2003,** *380* (3-4), 404-410.

14. Deàk, J. C.; Iwaki, L. K.; Dlott, D. D., Vibrational Energy Redistribution in Polyatomic Liquids: Ultrafast Ir−Raman Spectroscopy of Acetonitrile. *The Journal of Physical Chemistry A* **1998,** *102* (42), 8193-8201.

15. Gruner, D.; Brumer, P., Intramolecular Vibrational Redistribution in Alkylbenzenes .1. Normal-Modes and Their Energy-Distribution. *Journal of Chemical Physics* **1991,** *94* (4), 2848-2861.

16. Gruner, D.; Brumer, P., Intramolecular Vibrational Redistribution in Alkylbenzenes .2. Spectroscopy and Dynamics. *Journal of Chemical Physics* **1991,** *94* (4), 2862-2872.

Chapter 9: Modifying Vibrational Energy Flow: The Effects of Ortho Substitution on Nitrobenzene†

9.1 Introduction

This chapter explores how energy flow between a phenyl group and a nitro substituent[1] can be affected by additional substituents, specifically ortho substituents –F and $–CH_3$ adjacent to the nitro group. Once again, this process will be analyzed using the materials science approach to studying energy flow where vibrational energy will be initially localized to one end of the molecule, either to the phenyl or a substituent, and monitored transferring to the other. Like the previous chapters the role of the liquid environment will be minimized in the interpretations here by concentrating only on shorter times, where intramolecular vibrational relaxation (IVR) processes are dominant. This chapter will demonstrate that, the previously observed unidirectional energy flow of nitrobenzene can be drastically altered by the addition of an ortho substituent. Tuning the diode-like behaviors of molecules like nitrobenzene would be another desirable ability for a "molecular toolbox" to control energy flow in molecular scale devices.

As a reminder, for monitoring energy flow from one end of a molecule, the protocol devised and used in the previous chapters works as follows. First quantum chemistry calculations are used to categorize the selected molecule's vibrations as being predominantly phenyl, substituent, or global. Excitation spectroscopy[1,2] is used to find one IR pump wavenumber to selectively generate substituent excitations, and one IR pump wavenumber to selectively generate phenyl excitations. This is accomplished by scanning the IR pump pulses

†Parts of this chapter are recreated from work recently accepted as: Pein, B. C.; Dlott, D. D., Modifying Vibratoinal Energy Flow in Aromatic Molecules: Effects of Ortho Substitution. *Journal of Physical Chemistry A* **2014** DOI:10.1021/jp4120546.

while monitoring the prompt appearance at t = 1 ps of phenyl or substituent excitations. Then the time evolution of vibrational energy is measured, with phenyl or substituent pumping, by summing the energy densities of many transitions, to create aggregate time-dependent phenyl, substituent or global energy densities.

When reading this chapter, a few prior results relevant here need to be kept in mind. Chapter 7 studied nitrobenzene (NB), and made a remarkable observation. When the phenyl group was pumped, via the ring CH-stretch (ν_{CH} at ~3100 cm^{-1}), there was some phenyl-to-nitro and phenyl-to-global transfer, but when the nitro group was pumped, via the νNO_1 + νNO_2 combination band near 2900 cm^{-1}, there was no detectable nitro-to-phenyl or nitro-to-global transfer. This finding, that *energy transfer between phenyl and a nitro substituent is unidirectional*, was the motivation for this chapter, which aims to understand how vibrational energy flow in nitrobenzenes could be modified by additional substituents. Chapter 8 also investigated a few alkyl benzenes.[3] When phenyl-to-alkyl energy transfer was measured, it was found that phenyl-to methyl transfer in toluene was significantly more efficient than transfer from phenyl to other alkyl groups such as isopropyl or *t*-butyl.

Unfortunately, due to the difficulty of IR-Raman measurements, this chapter couldn't explore as many substituted nitrobenzenes that were desired. This work was limited to those that are liquids at ambient temperature, that produce minimal optical emission when irradiated by intense IR and visible picosecond pulses, and that have relatively large Raman cross-sections.[4] Two commercially available liquids that worked well were found, o-nitrotoluene and o-fluoronitrobenzene, where the ortho substituents were $-CH_3$ and -F. Going forward the following abbreviations will be used: nitrobenzene (NB), o-nitrotoluene (ONT) and o-fluoronitrobenzene (OFNB).

There are a few ways that adding an ortho substituent could affect phenyl-to-nitro energy flow. Ortho substitution would lower the symmetry from C_{2v} to C_s which would effectively relax selection rules for mode-mode anharmonic couplings and potentially accelerate and open up new channels for energy flow.[5] There will be steric interactions between the two adjacent substituents. Steric interactions could affect vibrational energy flow in two ways, by altering the NB geometry, and by opening up pathways for energy transfer between the substituents. Gas phase[6] and solid phase experiments,[7] and theoretical[6,8] studies have shown that steric interactions frequently cause the nitro group to rotate out of the phenyl plane. Additionally, the increased mass[9] and number of atoms (in the case of ONT) would be expected to increase the DOS relative to NB which could accelerate energy flow.

9.2 Results

IR and Raman Spectra and Assignments

The Stokes-Raman and IR spectra of ONT and OFNB are shown in Figure 9.1. The lower frequency regions of the IR spectra <600 cm^{-1} were noisy and thusly removed. Using the Gaussian 09 computational package, the normal modes of OFNB and ONT were calculated with MP2 perturbation theory utilizing the 6-31G basis. The resulting normal mode vectors and frequencies were used in conjunction with literature assignments[8,10-12] of the vibrational spectra. The full list of vibrational assignments and mode vector illustrations are shown in Section 9.5 and Section 9.6 respectively. The modes were classified as substituent, phenyl or global based on their potential energy distributions (PED), as explained in chapter 8. According to these assignments, OFNB had 19 phenyl, 15 global and 2 nitro modes, while ONT had 14 phenyl, 24 global, 2 nitro and 5 methyl modes. With OFNB, 21% of the phenyl, 33% of the global, and all the nitro modes, with the exception of the ~60 cm^{-1} hindered rotation,[13] which was regard as a

bath mode[14] rather than a nitrobenzene mode, were monitored. With ONT, 28% of the phenyl, 21% of the global, 33% of the methyl, and all the nitro modes were monitored, again with the exception of the hindered rotation.

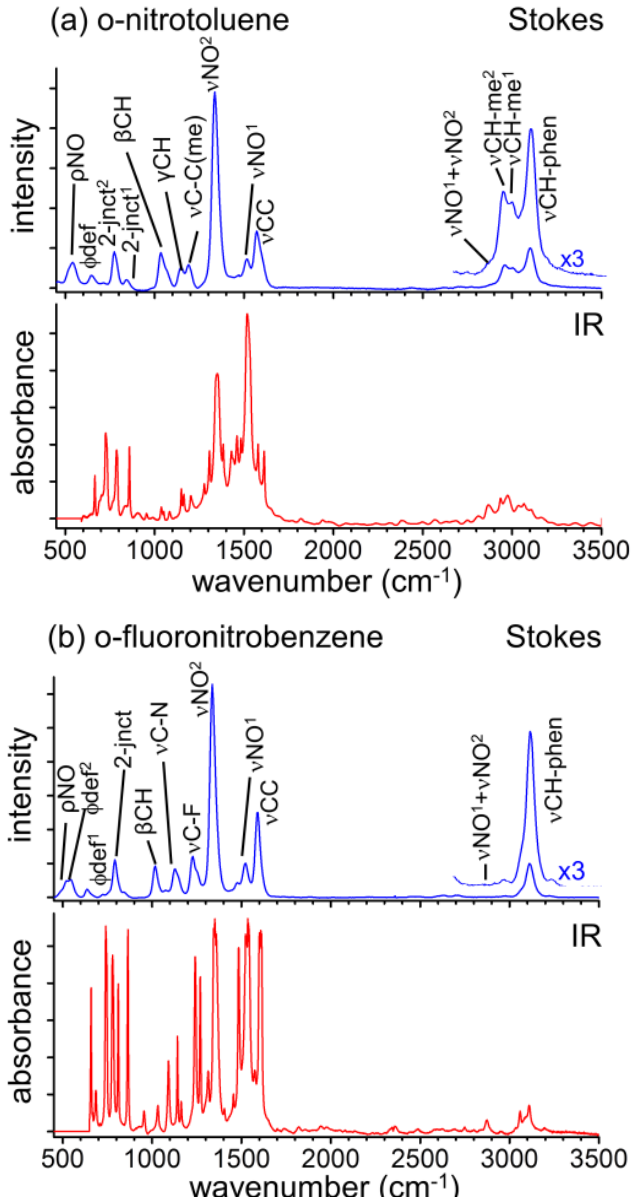

Figure 9.1. Infrared and Raman spectra of o-nitrotoluene and o-fluoronitrobenzene. The Raman spectra of (a) o-nitrotoluene and (b) o-fluoronitrobenzene were acquired using the picosecond probe pulses, which gave 25 cm^{-1} resolution. IR spectra were acquired using an FTIR spectrometer with 4 cm^{-1} resolution.

The assignments of the transitions with large enough Raman cross-sections to be monitored in this study are indicated in Figure 9.1.

The assignment labeling scheme is explained as follows: νCH-phen (~3100 cm^{-1}) is the phenyl C-H stretch, νCC modes (~1600 cm^{-1}) are phenyl C-C stretches with some in-plane phenyl C-H bend character, νC-N (~1100 cm^{-1}) or νC-C(Me) (~1200 cm^{-1}) are global modes involving displacement of the substituent-to-phenyl bonds, as well as in-plane C-H bending, double junction (2-jnct) modes (~900 and 800 cm^{-1}) are global modes involving the displacement of both substituents away from the ring, γCH (~1170 cm^{-1}) are phenyl in-plane C-H bends, βCH (~1000 cm^{-1}) are phenyl breathing modes, φdef (~670 cm^{-1}) are phenyl C-C-C deformations with some nitro scissoring, and νC-F (~1200 cm^{-1}) is a phenyl mode involving displacement of the fluorine atom. The methyl C-H stretches (~2950 cm^{-1}) are labeled νCH-Me. The νNO modes (~1540 and 1350 cm^{-1}) are nitro modes with N-O stretching, the nitro and methyl rocking modes ρNO (~500-600 cm^{-1}) are global modes involving in-plane tilt of the substituent, as well as ring C-C-C deformation and out-of-plane C-H bending.

Excitation Spectroscopy

Excitation spectra for ONT and OFNB are shown in Figure 9.2. As a reminder the waterfall plots are anti-Stokes spectra at 1 ps pump-probe delay, with the ambient temperature background signals (at -3 ps) subtracted away. The excitation spectra indicate how the initial energy distribution at t = 1 ps depends on pump wavenumber.[1-3] The peaks on the diagonal result from a combination of parent vibrational populations plus a sum-frequency generation (SFG) artifact,[15,16] so the 1 ps diagonal peak heights are not an accurate measure of the parent populations.[17] However the artifact decays with the apparatus temporal response (~1 ps), while the population contribution decays more slowly, with the excited state lifetime T_1.

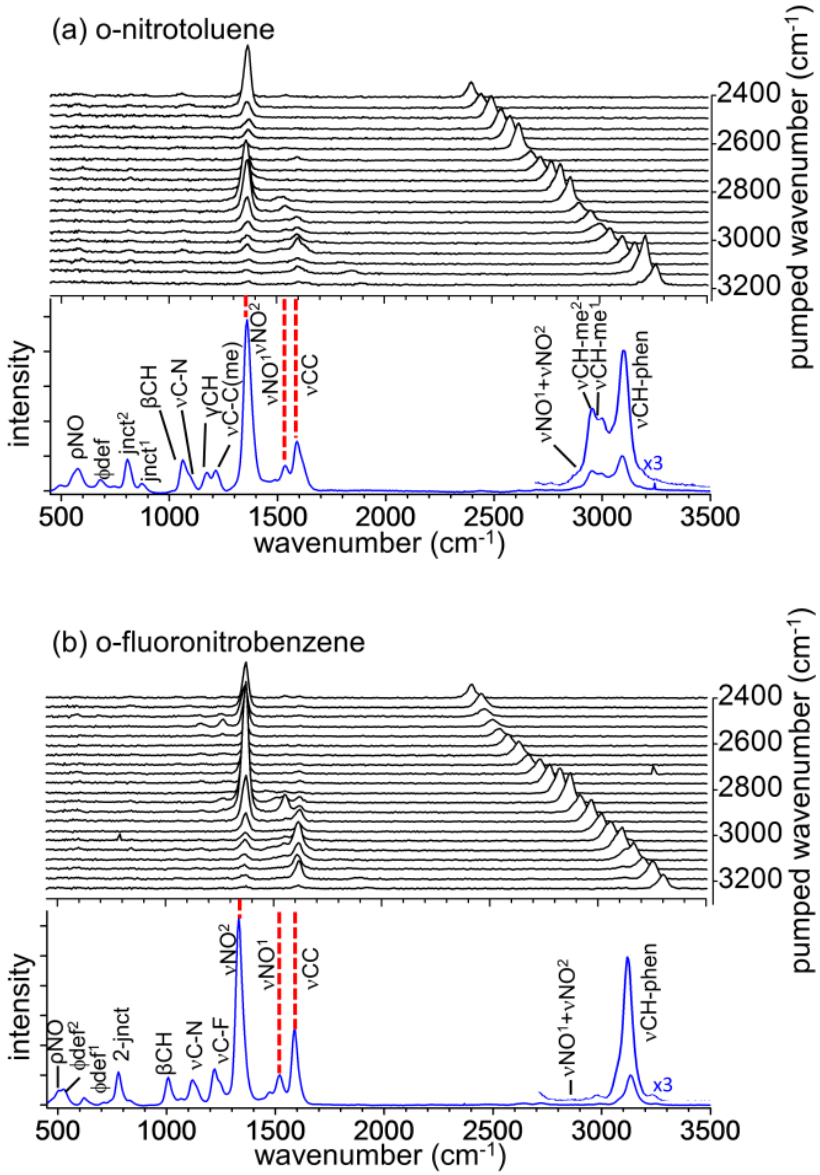

Figure 9.2. Excitation spectra of o-nitrotoluene and o-fluoronitrobenzene. The waterfall plots are the anti-Stokes intensities of (a) o-nitrotoluene and (b) o-fluoronitrobenzene at 1 ps following the IR pump pulses. Below each waterfall plot is a reference Stokes Raman spectrum with mode assignments. Transitions indicated by red dashed lines were nitro or phenyl modes used to determine the best IR pump wavenumbers for nitro or phenyl pumping.

Provided T_1 > 1 ps, one can track the parent populations after ~1 ps, but the parent populations at t = 0 are uncertain. The off-diagonal peaks in Figure 9.2 represent daughter transitions, which grow in as the parent excitations decay. The instantaneous population, or occupation number, change of each mode is proportional to the fraction $I_\omega^{AS}/I_\omega^{ST}$. As a guide to the Stokes intensities of each mode, the Stokes spectra are plotted below each waterfall plot. In addition the mode assignments on each Stokes spectrum are noted. The anti-Stokes and Stokes intensities were used to determine vibrational energy densities. The pump wavenumber dependence of the largest energy densities at 1 ps delay, being nitro stretches and the phenyl νCC stretch, were plotted below in Figure 9.3. In Figure 9.3, the IR absorption spectrum was also plotted as a reference, showing how the IR absorption coefficients varied with pump wavenumber for ONT and OFNB.

Like the nitrobenzene study, to assess the degree of initial phenyl excitation, the phenyl C-C stretch, νCC at ~1600 cm^{-1}, was focused on as a proxy for the phenyl energy. To assess the degree of initial nitro excitation, the combined excitations of νNO^1 at ~1545 cm^{-1} and νNO^2 at ~1366 cm^{-1} were monitored. These phenyl and nitro transitions are denoted by dashed vertical lines in Figure 9.2. In Chapter 8, to assess the degree of methyl excitation in toluene, the methyl bends in the 1400-1500 cm^{-1} region were probed. Unfortunately in ONT, there was too much overlap between the methyl bends and the intense νNO^1 transition, so reliable methyl excitation levels could not be extracted. However this overlap did not hinder the ability to determine the energy of the νNO^1 transition. Due to the inability to accurately determine the vibrational energy of the ortho methyl group, in what follows, understanding how phenyl-to-nitro and nitro-to-phenyl transfers were perturbed by the ortho methyl and fluoro substituents will be the primary focus.

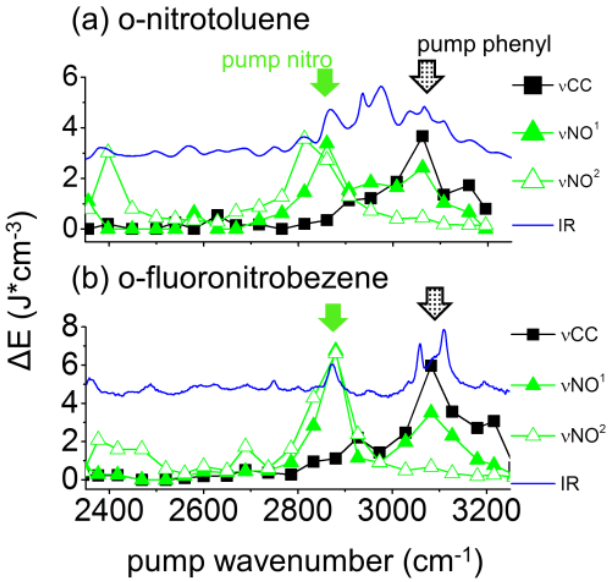

Figure 9.3. Energy density changes ΔE of o-nitrotoluene and o-fluoronitrobenzene at 1 ps delay. As the IR pump pulses were scanned through the indicated pump wavenumber range nitro (green) and phenyl (black) vibrations were excited. The IR absorption spectrum was included as a reference. The arrows denote the pump wavenumbers that were selected for nitro or phenyl pumping.

To generate initial phenyl excitations, it was found, based on Figure 9.3, that both OFNB and ONT exhibited maximal levels of νCC excitation with the IR pump tuned to ~3100 cm^{-1}, near the maximum of the νCH-phen transition. To generate initial nitro excitations, maximum levels of νNO^1 and νNO^2 excitations occurred with the IR pump tuned to ~2900 cm^{-1}. This nitro pump transition was the νNO^1 + νNO^2 combination band used in the Chapter 7 NB studies.[1] Recall that in these experiments, due to the Δv = ±1 selection rule for Raman scattering, excitations of combination and overtone bands are generally observed as fundamental excitations.[18,19] Pumping this 2900 cm^{-1} combination band results in an instantaneous rise in the anti-Stokes spectrum of the νNO^1 and νNO^2 fundamentals, at ~1350 cm^{-1} and ~1550 cm^{-1} respectively.

Henceforth, "phenyl pumping" will refer to 3100 cm^{-1} excitation and "nitro pumping" to 2900 cm^{-1} excitation. Looking closely at Figure 9.3, with both ONT and OFNB, it is shown that phenyl pumping was only partially selective, as indicated by the degree of nitro excitation. However nitro pumping was quite a bit more selective. With ONT, nitro pumping produced minimal phenyl excitation. With OFNB, nitro pumping was not quite as selective as with ONT. Nitro pumping of OFNB produced a small, but detectable, quantity of phenyl excitation.

The issue of nonselective pumping is clarified by looking at the time dependence of the population transients. Recall that populations created by the IR pulses, due to coherent coupling to the parent, rise instantaneously and are limited only by the apparatus temporal response. For instance the parent vibrational populations always rise instantaneously. However vibrational populations created by phenyl-to-substituent or substituent-to-phenyl transfer rise slower than instantaneous. For instance, with nonselective phenyl pumping in a molecule with phenyl-to-nitro transfer, the nitro population will have a two-part rise. The faster (instantaneous) part denotes nitro excitations produced by the (non-selective) pump pulses, and the slower part, with a finite risetime, denotes the population created by phenyl-to-nitro transfer. The time constant for the rise of this slower part is the phenyl-to-nitro time constant.

Anti-Stokes Transients

Figures 9.4a,b show the IR-Raman spectra for ONT and OFNB during the first 10 ps, following nitro or phenyl pumping. Note that frequencies between 1700 cm^{-1} and 2800 cm^{-1} have been removed. Above each waterfall the Stokes spectra and assignments as references are plotted. Near t = 0 ps, the parent transitions contain a contribution from the SFG artifact mentioned above. Nitro pumping of the parent ~2900 cm^{-1} $\nu NO^1 + \nu NO^2$ combination band produced instantaneously-rising signals in both νNO^1 and νNO^2.

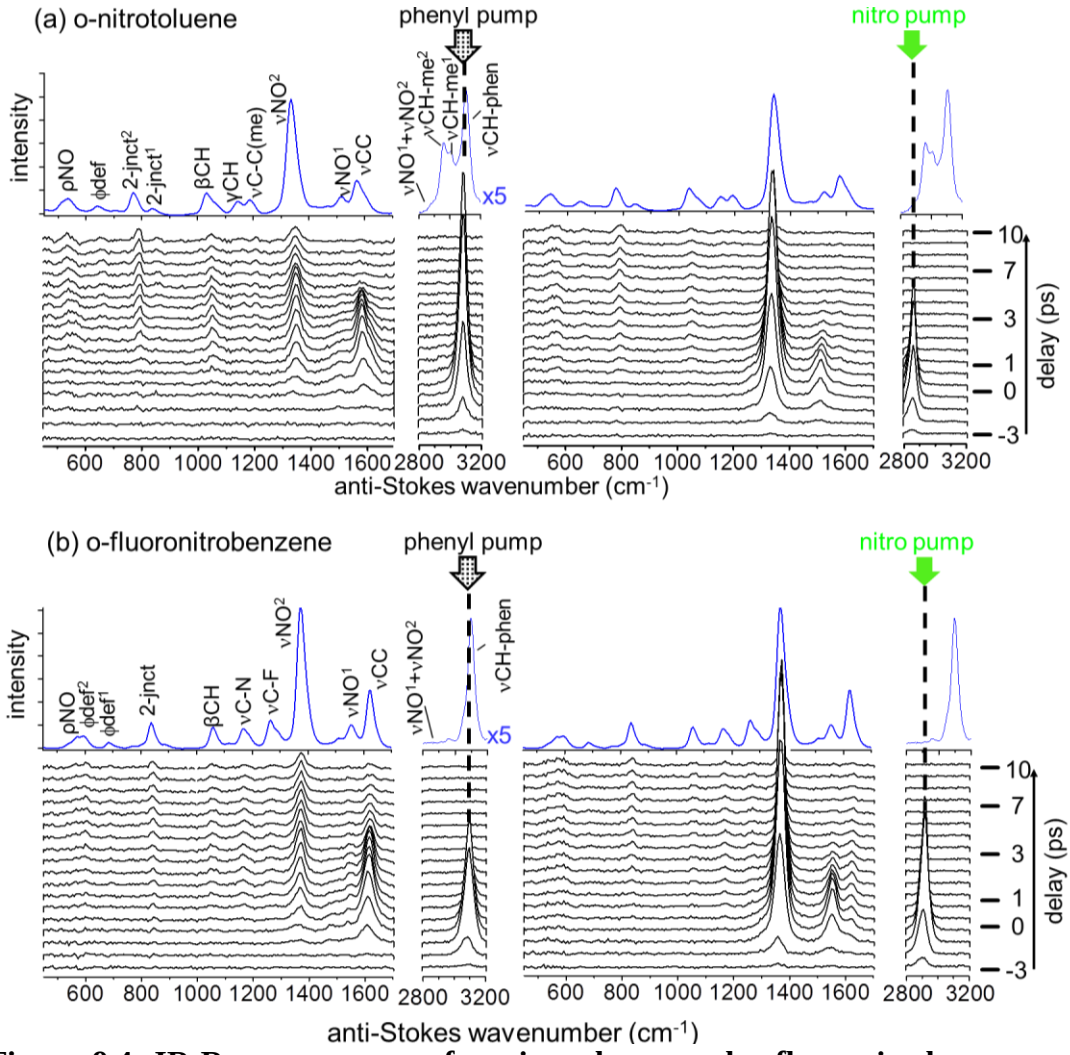

Figure 9.4. IR-Raman spectra of o–nitrotoluene and o-fluoronitrobenzene. The results of phenyl pumping (left) and nitro pumping (right) are shown for (a) o-nitrotoluene and (b) o-fluoronitrobenzene. The signals at the pump wavenumber arise from both vibrational populations and coherent artifacts. The artifacts have mostly disappeared by t = 1 ps. Reference Stokes Raman spectra are displayed above each IR-Raman spectrum. The Stokes Raman intensities are approximately proportional to the Raman cross-sections.

Vibrational Energy Densities

Using the IR-Raman spectra in Figure 9.4, the vibrational energy density change of each detected transition over a 10 ps time range was computed.[1,20] Figure 9.5 shows these mode-specific energy densities for ONT and OFNB. Each bar was color-coded to represent nitro,

phenyl or global modes. Because one cannot accurately measure populations in the parent modes near $t = 0$, the amplitudes of the parent signals in Figure 9.6 were scaled arbitrarily.

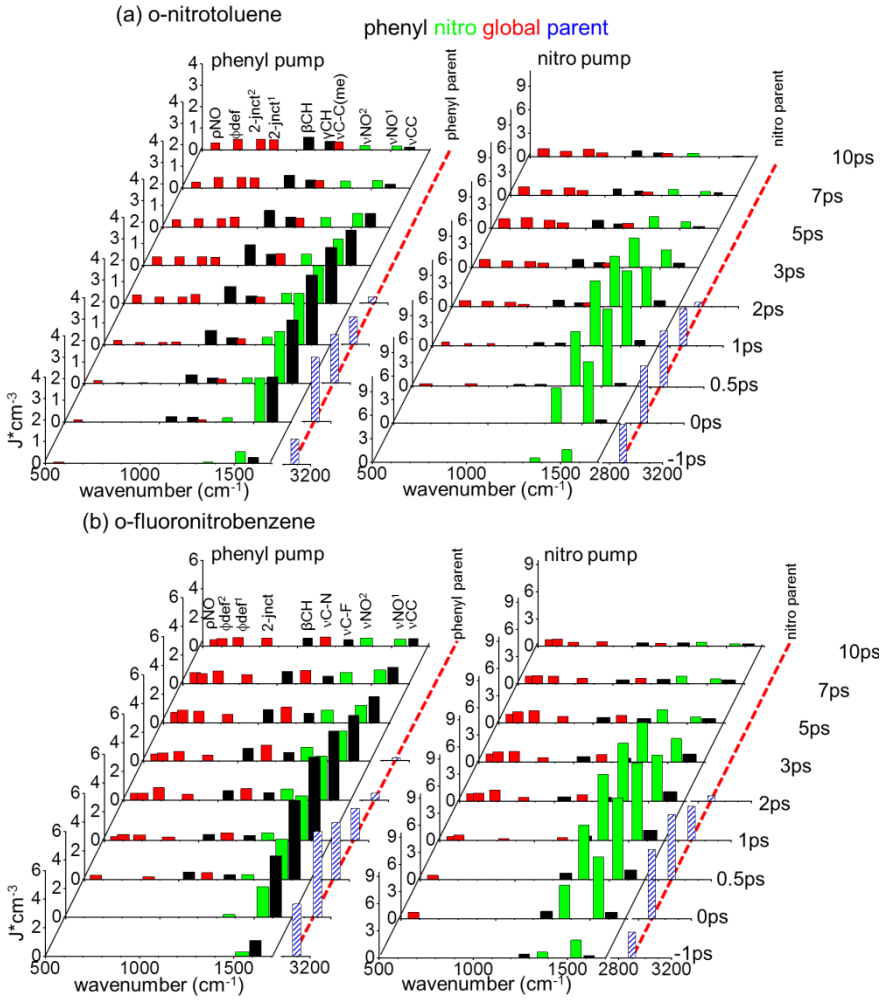

Figure 9.5. o-nitrotoluene and o-fluoronitrobenzene transient energy densities. Results for (a) o-nitrotoluene (b) o-fluoronitrobenzene after phenyl (left) and nitro (right) pumping are shown. The dashed lines indicate the parent excitation wavenumber. The parent energy densities, indicated by diagonal-striped bars, were arbitrarily scaled, since the presence of a coherent artifact at shorter time delays distorts the intensity.

Spatially Resolved Energy Densities

The daughter energy densities from Figure 9.5 were summed to determine the time-dependent aggregate energy densities in the phenyl, nitro, or global modes, as shown in Figure 9.6. These aggregate densities are the observed energies, and, based on ultrafast calorimetry

studies of benzene,[20] the time dependence and relative amplitudes are representative of the total energies, which would include the vibrational modes that were not observed directly. The dashed curves are the signals from the IR-pumped parent vibrations, whose amplitudes, because of the SFG artifact, were arbitrarily scaled. This is a notably different approach compared to the alkylbenzenes and NB studies in the previous chapters that is believed to be more accurate since the artifact can over- or underestimate the energy content in the parent near t = ~0 ps.

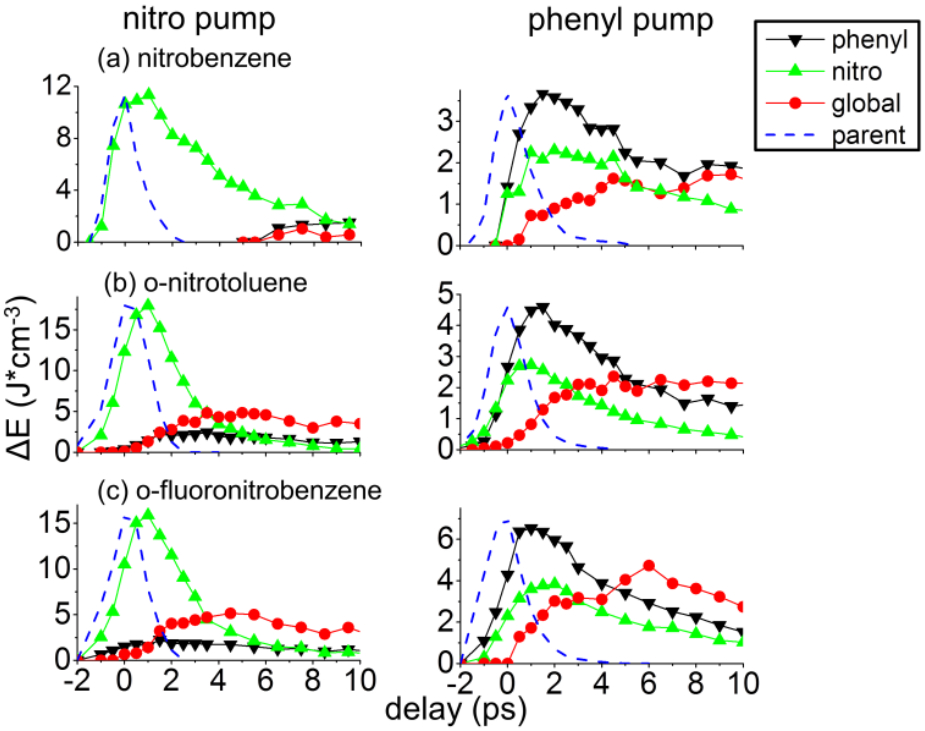

Figure 9.6. o-nitrotoluene and o-fluoronitrobenzene aggregate transient energy densities. The results from the nitrobenzene study are included here. The dashed curves denoted "parent" represent the time-dependence of vibrational energies of the parent phenyl or nitro modes, but the parent amplitudes were normalized to put them on scale, so the parent energy densities are not as indicated. Nitro pumping initially produced primarily nitro excitations, but phenyl pumping was less selective, so phenyl pumping also generated some nitro excitations. With phenyl pumping the nitro populations generated by IR pumping rose instantaneously. The nitro populations created by phenyl-to-nitro transfer rose more gradually over the first ~2 ps.

9.3 Discussion

The most significant results obtained here are summarized by Figure 9.6, where the time-dependent aggregate energies of phenyl, nitro or global vibrations of NB, ONT and OFNB, are plotted following either nitro or phenyl pumping. The NB data was replotted from the chapter 7 data.[1] To better explain this analysis, the interpretation of the NB data from Chapter 7 is recapitulated. With NB, as with ONT and OFNB, phenyl pumping was only partially selective, but nitro pumping was highly selective. In NB, with nitro pumping there were absolutely no phenyl or global excitations until about 6 ps. In the interpretation of the NB data, the small amount of phenyl and global excitations appearing at times >5 ps were not produced by intramolecular phenyl-to-nitro transfer. Instead these were secondary excitations associated with intermolecular processes. As the pumped NB molecules lost their excess energy to the bath, ultimately leading to a bulk temperature jump (T-jump) of ~30K,[1] other molecules could uptake some of this energy, which increased the excitation levels of the lower-energy phenyl and global modes. In other words, the longer-time phenyl and global excitations that appeared after nitro pumping of NB resulted from an indirect (nitro vibration $\rightarrow$ bath $\rightarrow$ phenyl vibrations on other molecules) process, rather than the direct nitro-to-phenyl process. In addition, the longer-time decay of the nitro population of NB was caused by energy dissipation to the bath rather than to the phenyl group. Thus, based on the $t < 5$ ps data, in NB nitro-to-phenyl and nitro-to-global processes were essentially absent.

With phenyl pumping of NB, the fact that some nitro excitations were also generated by the pump pulses must be taken into account. Looking at the phenyl pumping transients in Figure 9.6a, the IR-pumped nitro excitations were those that appeared instantaneously, resulting in a population that tracked the rising edge of the phenyl excitation. After this instantaneous rise of

nitro population there appears a second rise clearly slower than the first. The amplitudes of both rise components were about equal. This second, slower rise of nitro population after phenyl pumping occurs over ~2 ps, and it represents nitro excitations created by intramolecular phenyl-to-nitro energy transfer. With phenyl pumping, no instantaneous rise of the global excitations was observed, indicating the IR pump pulses did not directly produce global excitations. The global population rose gradually over the first 5 ps or so. This rise was interpreted as representing phenyl-to-global transfer. So, in summary for NB, it was concluded there was no nitro-to-phenyl or nitro-to-global transfer, but there was clear evidence for 2 ps phenyl-to-nitro transfer and 5 ps phenyl-to-global transfer. In this analysis, one should not attribute too much significance to the relative values of the phenyl, nitro and global aggregate energy densities in Figure 9.6, since there will be some systematic error in these relative amplitudes due to selection bias.

In the ONT data in Figure 9.6b, with nitro pumping there was more nitro-to-phenyl and nitro-to-global transfer than with NB, so in ONT vibrational energy no longer remains entirely localized on the nitro group, as with NB. The methyl substituent adjacent to the nitro group has clearly opened up new channels for nitro-to-phenyl and nitro-to-global processes. With phenyl pumping of ONT, the entire nitro population seen in Figure 9.6b has an instantaneous rise, so it was all generated by the IR pump pulses. There was no delayed rise in the nitro population, and therefore in ONT with phenyl pumping there is practically no phenyl-to-nitro transfer. There is phenyl-to-global transfer in ONT, at about the same level as with NB.

In the OFNB data in Figure 9.6c, it can again be seen from the nitro pumping data, that the ortho substituent -F allows energy to flow from the nitro groups into the phenyl and global modes, with about the same efficiency as with ONT. With phenyl pumping, instantaneously-

generated nitro excitations were observed and a small amount of delayed nitro excitation, which caused the nitro population in Figure 9.6c to rise slightly slower than the phenyl population. Thus there was significantly less phenyl-to-nitro transfer in either ONT or OFNB compared to NB.

From Figure 9.6, it is concluded that ortho substituents activate the nitro-to-phenyl and nitro-to-global pathways that were absent in NB. Additionally, ortho substituents suppressed phenyl-to-nitro transfer, compared to NB. This suppression was more efficient with the ortho methyl substituent than with the ortho fluoro substituent.

At the present time, it is not possible to present compelling and conclusive quantitative explanations for these effects, but reasonable qualitative interpretations are possible. A nitro-group excitation on NB is isolated from the phenyl and global modes. But in the ortho-substituted species, there are steric interactions between nitro and the ortho-substituents, allowing the nitro excitations to transfer energy to modes involving ortho substituent displacements. These interactions activate nitro-to-phenyl and nitro-to-global transfer. The ortho substituents also tend to suppress phenyl-to-nitro transfer, with suppression by the ortho methyl substituent being more effective. Presumably the suppression of nitro-to-phenyl transfer results from a competition between the nitro group and the ortho substituent modes or the global modes created by adding the ortho substituents. The methyl group seems to be more effective in the competition with the nitro group for the phenyl energy, and that is consistent with the Chapter 8 study of toluene,[3] where it was found that phenyl-to-methyl transfer could be efficient.

9.4 Conclusions

A number of useful observations have been made. In particular, in Chapter 7, NB was found to exhibit unidirectional energy transfer, where there was some phenyl-to-nitro transfer but

no nitro-to-phenyl transfer. This chapter investigated how additional substituents might affect this unidirectional energy transfer. It was found that substituents ortho to the nitro groups, which were known to have significant steric interactions with the nitro groups, destroyed the unidirectional property of NB by opening up nitro-to-phenyl and nitro-to-global channels. It was also found that adding a methyl substituent could shut down the phenyl-to-nitro process. Since Chapter 8 demonstrated that phenyl-to-methyl transfer was facile in toluene, it is likely the methyl group successfully competes against the nitro group for the phenyl energy. A diode is an electronic component where current flows only in one direction. The efficiencies of the vibrational energy transfer processes observed are nothing like what is seen with today's highly-developed electronic devices, but according to these findings, NB is a vibrational energy diode where energy flows only in the phenyl-to-nitro direction, whereas ONT is a vibrational energy diode where energy flows only in the nitro-to-phenyl direction.

9.5 Normal Mode Assignments

o-fluoronitrobenzene (OFNB) vibrational frequencies

mode	MP2	Raman int.	experimental	PED(%)	classification
v36	3149	1		phenyl(100)	phenyl
v35	3144	0.64		phenyl(100)	phenyl
vCH-phen (v34)	3135	0.63	3100	phenyl(100)	phenyl
v33	3122	0.41		phenyl(100)	phenyl
vNO^1(v32)	1733	0.45	1545	subs(100)	subs
v31	1621	0.11		subs(1) phenyl(99)	phenyl
vCC (v30)	1614	0.21	1614	global(3) phenyl(97)	phenyl
v29	1497	0.06		global(4) phenyl(96)	phenyl
v28	1457	0.02		global(4) phenyl(96)	phenyl
v27	1422	0.03		subs(1) global(2) phenyl(97)	phenyl
vNO^2 (v26)	1362	0.54	1366	global(4) phenyl (5) subs(81)	subs
vC-F(v25)	1270	0.07	1270	phenyl(100)	phenyl
v24	1247	0.04		subs(2) global(4) phenyl(94)	phenyl
v23	1170	0.04		subs(2) global(3) phenyl(95)	phenyl
vC-N (v22)	1145	0.05	1150	subs(7) global(16) phenyl(77)	global
v21	1090	0.01		subs(7) global(15) phenyl(78)	global
βCH (v20)	1033	0.12	1054	global(1) phenyl(99)	phenyl
v19	866	0		phenyl(100)	phenyl
v18	862	0.01		global(1) phenyl(99)	phenyl
v17	840	0.01		global(13) subs(31) phenyl(56)	global
v16	800	0.04		subs(5) phenyl(95)	phenyl
2-jnct. (v15)	790	0.11	839	global(9) subs(30) phenyl(61)	global
v14	744	0		global(22) phenyl(78)	global
v13	700	0.02		phenyl(28) global(72)	global
Φdef (v12)	650	0.02	686	global(11) subs(27) phenyl(62)	global
ρNO (v11)	571	0.03	600	subs(2) global(43) ring(55)	global
βCCC (v10)	529	0.03	565	subs(6) global(15) phenyl(79)	global
v9	487	0.01		subs(5) global(9) phenyl(86)	phenyl
v8	454	0		global(4) phenyl(96)	phenyl
v7	423	0.01		subs(5) global(19) phenyl(76)	global
v6	371	0.01		subs(8) global(25) phenyl(67)	global
v5	338	0.01		subs(6)global(33) phenyl(62)	global
v4	233	0.03		subs(2) global(11) phenyl(87)	phenyl
v3	213	0		subs(5) phenyl(16) global(79)	global
v2	129	0.04		subs(4) phenyl(16) global(80)	global
v1	59	0.02		phenyl(5) global(95)	global

Table 9.1.o-nitrotoluene and o-fluoronitrobenzene normal mode assignments.

o-nitrotoluene (ONT) vibrational frequencies

mode	MP2	Raman int.	experimental	PED(%)	classification
v45	3180	0.69		phenyl(100)	phenyl
vCH-phen (v44)	3162	1	3100	phenyl(100)	phenyl
v43	3149	0.6		phenyl(100)	phenyl
v42	3135	0.43		phenyl(100)	phenyl
vCH-me^{1} (v41)	3121	0.44		subs(100)	subs
v40	3118	0.32		subs(100)	subs
vCH-me^{2} (v39)	3030	0.81	2950	subs(100)	subs
vNO^{1} (v38)	1737	0.37	1532	subs(100)	subs
v37	1639	0.14		subs(5) phenyl(95)	phenyl
vCC (v36)	1610	0.22	1610	subs(1) phenyl(99)	phenyl
v35	1511	0.08		phenyl(23) subs(73)	global
v34	1504	0.07		global(1) phenyl(29) subs(68)	global
v33	1501	0.08		global(5) subs(47) phenyl(48)	global
v32	1462	0.02		subs(4) global(7) phenyl(89)	phenyl
v31	1435	0.12		global(2) phenyl(13) subs(84)	subs
v30	1429	0.04		global(2) subs(11) phenyl(87)	phenyl
vNO^{2} (v29)	1379	0.65	1362	phenyl(5) global(14) subs(81)	subs
v28	1295	0.02		global(5) subs(11) phenyl(85)	phenyl
vC-C(me) (v27)	1224	0.08	1225	subs(1) global(38) phenyl(61)	global
γCH (v26)	1187	0.04	1178	phenyl(100)	phenyl
v25	1166	0.04		subs(9) global(10) phenyl(81)	phenyl
v24	1098	0.02		subs(11) global(17) phenyl(62)	global
βCH (v23)	1063	0.12	1065	global(3) subs(7) phenyl(90)	phenyl
v22	1050	0.01		phenyl(7) subs(93)	subs
v21	1012	0.02		phenyl(33) subs(62)	global
v20	870	0		global(10) phenyl(90)	phenyl
v19	867	0.01		global(38) phenyl(62)	global
2-jnct^{1} (v18)	842	0.02	881	global(22) phenyl(28) subs(50)	global
v17	816	0.03		phenyl(14) global(86)	global
2-jnct^{2} (v16)	784	0.1	811	global(21) subs(23) phenyl(56)	global

Table 9.1 (cont.).o-nitrotoluene and o-fluoronitrobenzene normal mode assignments.

o-nitrotoluene (ONT) vibrational frequencies (cont.)

mode	MP2	Raman int.	experimental	PED(%)	classification
v15	752	0		subs(28) phenyl(31) global(41)	global
v14	704	0.02		phenyl(21) global(26) subs(53)	global
Φdef (v13)	665	0.03	689	global(8) subs(22) phenyl(68)	global
v12	572	0.04	570	subs(2) phenyl(42) global(56)	global
ρNO (v11)	536	0.04	570	subs(5) global(33) phenyl(62)	global
v10	468	0		global(3) subs(4) phenyl(93)	phenyl
v9	446	0.01		subs(3) phenyl(32) global(65)	global
v8	411	0		subs(10) phenyl(39) global(51)	global
v7	375	0.01		global(13) subs(27) phenyl(60)	global
v6	346	0.01		global(17) phenyl(38) subs(45)	global
v5	245	0		global(4) phenyl(9) subs(87)	global
v4	219	0.02		subs(8) phenyl(35) global(57)	global
v3	198	0.01		subs(4) phenyl(10) global(86)	global
v2	131	0.03		subs(6) phenyl(15) global(79)	global
v1	63	0.02		subs(2) phenyl(4) global(94)	global

Table 9.1 (cont.).o-nitrotoluene and o-fluoronitrobenzene normal mode assignments. Vibrational frequencies and mode classifications of o-nitrotoluene and o-fluoronitrobenzene. The named modes are those that are visible in the experiment while others are only numbered. The included computed Raman intensities are normalized. The potential energy distribution percentages (PED(%)) are indicated in the parentheses. If a mode had ≥80% of its energy distributed to the phenyl or substituent, it was classified as phenyl or substituent respectively. Otherwise, it was classified as global.

9.6 Normal Mode Vector Illustrations

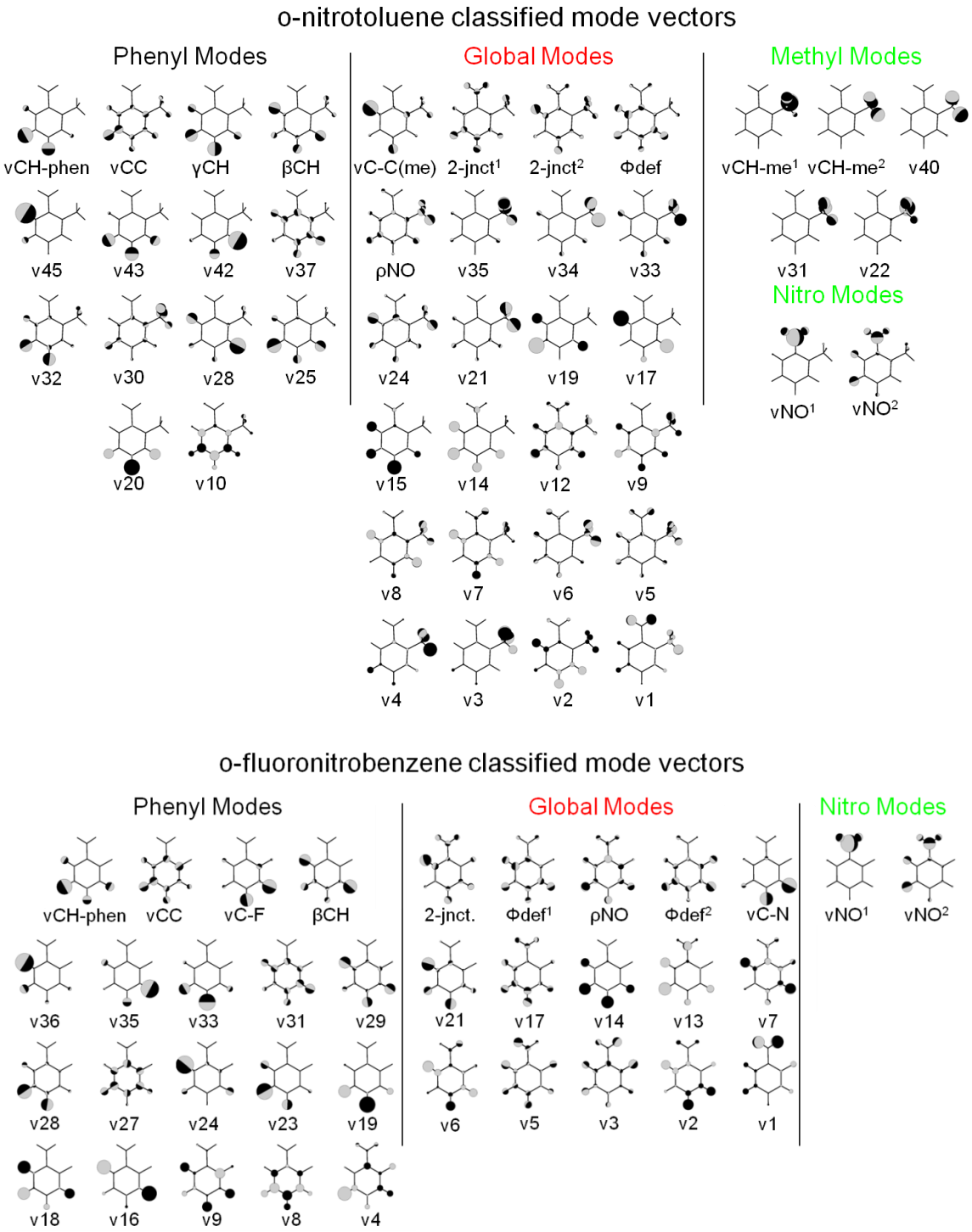

Figure 9.7. o-nitrotoluene and o-fluoronitrobenzene normal mode vector illustrations. Classified normal modes of o-nitrotoluene and o-fluoronitrobenzene computed using MP2 perturbation theory with the 6-31G basis set. Relative sphere sizes indicate relative displacement while the grey and white filling represents the displacement direction.

9.7 References

1. Pein, B. C.; Sun, Y.; Dlott, D. D., Unidirectional Vibrational Energy Flow in Nitrobenzene. *Journal of Physical Chemistry A* **2013,** *117* (29), 6066-72.

2. Sun, Y.; Pein, B. C.; Dlott, D. D., Three-Dimensional Spectroscopy of Vibrational Energy in Liquids: Nitromethane and Acetonitrile. *Journal of Physical Chemistry B* **2013,** *117* (49), 15444-51.

3. Pein, B. C.; Sun, Y.; Dlott, D. D., Controlling Vibrational Energy Flow in Liquid Alkylbenzenes. *The Journal of Physical Chemistry B* **2013,** *117* (37), 10898-10904.

4. Deak, J. C.; Iwaki, L. K.; Rhea, S. T.; Dlott, D. D., Ultrafast Infrared-Raman Studies of Vibrational Energy Redistribution in Polyatomic Liquids. *Journal of Raman Spectroscopy* **2000,** *31* (4), 263-274.

5. von Benten, R. S.; Liu, Y. X.; Abel, B., Dynamical Consequences of Symmetry Breaking in Benzene and Difluorobenzene. *Journal of Chemical Physics* **2010,** *133* (13).

6. Shishkov, I. F.; Khristenko, L. V.; Vilkov, L. V.; Samdal, S.; Gundersen, S., Molecular Structure of Ortho-Fluoronitrobenzene Studied by Gas Electron Diffraction and Ab Initio Mo Calculations. *Structural Chemistry* **2003,** *14* (2), 151-157.

7. Yakovenko, A. A.; Antipin, M. Y.; Timofeeva, T. V., Molecular and Crystal Structure of Low Melting Nitrotoluene Isomers. *Crystal Growth & Design* **2009,** *9* (1), 57-65.

8. Arjunan, V.; Govindaraja, S. T.; Sakiladevi, S.; Kalaivani, M.; Mohan, S., Spectroscopic, Electronic Structure and Natural Bond Orbital Analysis of O-Fluoronitrobenzene and P-Fluoronitrobenzene: A Comparative Study. *Spectrochimica Acta Part a-Molecular and Biomolecular Spectroscopy* **2011,** *84* (1), 196-209.

9. Pein, B. C.; Seong, N. H.; Dlott, D. D., Vibrational Energy Relaxation of Liquid Aryl-Halides X-C6h5 (X = F, Cl, Br, I). *Journal of Physical Chemistry A* **2010,** *114* (39), 10500-10507.

10. Rao, P. M.; Rao, G. R., Vibrational-Spectra and Normal Coordinate Analysis of Monohalogenated Nitrobenzenes. *Journal of Raman Spectroscopy* **1989,** *20* (8), 529-540.

11. Qayyum, M.; Reddy, B. V.; Rao, G. R., Vibrational Analysis of Mononitro Substituted Benzamides, Benzaldehydes and Toluenes - Part I. Vibrational Spectra, Normal Coordinate Analysis and Transferability of Force Constants of Nitrobenzamides, Nitrobenzaldehydes and Nitrotoluenes. *Spectrochimica Acta Part a-Molecular and Biomolecular Spectroscopy* **2004,** *60* (1-2), 279-290.

12. Varsányi, G. r.; Láng, L., *Assignments for Vibrational Spectra of Seven Hundred Benzene Derivatives*. Wiley: New York,, 1974.

13. Rice, B. M.; Trevino, S. F., An Intermolecular H-O Potential for Methyl Rotations in Solid Nitromethane. *Journal of Chemical Physics* **1991,** *94* (11), 7478-7485.

14. Deak, J. C.; Iwaki, L. K.; Diott, D. D., Vibrational Energy Redistribution in Polyatomic Liquids: Ultrafast Ir-Raman Spectroscopy of Nitromethane. *Journal of Physical Chemistry A* **1999,** *103* (8), 971-979.

15. Chen, H. L.; Bian, H. T.; Li, J. B.; Wen, X. W.; Zheng, J. R., Ultrafast Multiple-Mode Multiple-Dimensional Vibrational Spectroscopy. *International Reviews in Physical Chemistry* **2012,** *31* (4), 469-565.

16. Iwaki, L. K.; Deak, J. C.; Rhea, S. T.; Dlott, D. D., Vibrational Energy Redistribution in Liquid Benzene. *Chemical Physics Letters* **1999,** *303* (1-2), 176-182.

17. Pakoulev, A.; Wang, Z. H.; Dlott, D. D., Vibrational Relaxation and Spectral Evolution Following Ultrafast Oh Stretch Excitation of Water. *Chemical Physics Letters* **2003,** *371* (5-6), 594-600.

18. Graener, H.; Laubereau, A., Ultrafast Overtone Excitation for the Study of Vibrational Population Decay in Liquids. *Chemical Physics Letters* **1983,** *102* (1), 100-104.

19. Deak, J. C.; Iwaki, L. K.; Dlott, D. D., When Vibrations Interact: Ultrafast Energy Relaxation of Vibrational Pairs in Polyatomic Liquids. *Chemical Physics Letters* **1998,** *293* (5-6), 405-411.

20. Seong, N. H.; Fang, Y.; Dlott, D. D., Vibrational Energy Dynamics of Normal and Deuterated Liquid Benzene. *Journal of Physical Chemistry A* **2009,** *113* (8), 1445-1452.

Chapter 10: Appendix

This chapter contains and describes the programs written to compute the vibrational Density of States (DOS) described in Chapter 4. Each of the scripts was written to be compiled with a standard FORTRAN 95 compiler.

Total Densities of States (DOS) Program

This program computes the total vibrational DOS. It utilizes an input array of vibrational frequencies and an average anharmonicity percentage. The output array, which is the DOS as a function of the transition energy, is binned according to a desired bin size. The Beyer-Swinehart counting algorithm is used to enumerate the list.

```
Program Total Densities of States (DOS)
  Implicit NONE
  Real :: anharmonicity
  Real, Dimension (0:50,0:50) :: fundamental
  Integer, Dimension (0:10000) :: p, r, A
  Integer :: Modes, I, J, MaxEX, E, MaxEn, q, k, L, h
  Integer :: bin, s
!Here the anharmonicity percentage is entered as fraction value. 5% is entered
!here.
  anharmonicity=0.05
!Here the number of modes are entered.
  Modes=30
!Here the maximum number of quanta to be considered in any individual mode is
!entered.
  MaxEx=20
!Here the bin size, in wavenumbers is entered. 100 cm-1 is entered here
  bin=100
!Here the maximum range of the energy E in the DOS p(E) is entered in units of
!wavenumbers. 4000 cm-1 is entered here.
  MaxEn=4000
!Here the energy of each fundamental vibrational transition is read in units of
!wavenumbers. fundamental (I,J) represents the Jth energy level of the Ith vibration.
!The ground state energy, fundamental (I,0), is defined as 0.
  Read(4,*) (fundamental(I,1), I=1,Modes)
  Do I = 1, Modes
    fundamental(I,0) = 0
  End Do
```

```
!Here the transition energy from the ground state to the J^th level in the I^th vibration
!is computed.
  Do I = 1, Modes
   Do J = 2, MaxEx
    fundamental(I,J) = fundamental(I,J-1)*(2.0-anharmonicity) &
                      -fundamental(I,J-2)*(1.0-anharmonicity)
   End Do
  End Do
!Here the Beyer-Swinehart counting algorithm is used to compute the DOS p(E).
  Do q = 1, Modes
   Do h = 1, MaxEn
    r(h) = 0
   End Do
   Do J = 1, MaxEx
    Do L = int(fundamental(q,J)), MaxEn
     r(L) = r(L) + p(L - int(fundamental(q,J)))
    End Do
   End Do
   Do k = 1, MaxEn
    p(k) = p(k) + r(k)
   End Do
 End Do
!Here the DOS is binned and written to an output array.
 Do S = 0, Modes
  Do E = (1 + S*bin), (S+1)*bin
     A(E) = A(E-1) + (p(E))
  End Do
   Write(7,*) A((S+1)*bin)
   Do E = 1, MaxEn
    A(E) = 0
   End Do
 End Do
 End Program Total Densities of States (DOS)
```

Tiered Densities of States (DOS) programs

These programs compute the DOS sorted according to the number of quanta in each state. For example, the N=1 tier are the collection of fundamental transitions which just looks like the spectrum of the molecule, the N=2 tier is the DOS with two quanta in each state, the N=3 has 3 quanta in each state and so on. Since the N=1 tier is trivial to compute, no program was written for it. An admittedly "brute-force" algorithm is used here.

N=2 tier

```
Program N=2 tiered DOS
  Implicit NONE
  Integer :: E, MaxEn, x, y, Modes, I, J, bin
  Integer, Dimension (0:4000) :: NN, NN2, A
  Real :: anharmonicity
  Real, Dimension (0:50,0:50) :: fundamental
!Here the anharmonicity percentage is entered as fraction value. 5% is entered
!here.
  anharmonicity=0.05
!Here the number of modes are entered.
  Modes=30
!Here the maximum number of quanta to be considered in any individual mode is
!entered.
  MaxEx=20
!Here the bin size, in wavenumbers is entered. 100 cm-1 is entered here
  bin=100
!Here the maximum range of the energy E in the DOS p(E) is entered in units of
!wavenumbers. 4000 cm-1 is entered here.
  MaxEn=4000
!Here the energy of each fundamental vibrational transition is read in units of
!wavenumbers. fundamental (I,J) represents the Jth energy level of the Ith vibration.
!The ground state energy, fundamental (I,0), is defined as 0.
  Read(4,*) (fundamental(I,1), I=1,Modes)
  Do I = 1, Modes
    fundamental(I,0) = 0
  End Do
```

```
!Here the transition energy from the ground state to the J^th level in the I^th vibration
!is computed.
 Do I = 1, Modes
  Do J = 2, MaxEx
   fundamental(I,J) = fundamental(I,J-1)*(2.0-anharmonicity) &
                      -fundamental(I,J-2)*(1.0-anharmonicity)
  End Do
 End Do
!Here the states composed of an N=2 overtone are enumerated as NN(E).
 Do E = 1, MaxEn
  Do x = 1, Modes
    If (E == int(fundamental(x,2))) Then
        NN(E) = NN(E) + 1
    End If
   End Do
 End Do
!Here the states composed of a combination of two N=1 fundamentals are
!enumerated as NN2(E)
 Do E = 1, MaxEn
  Do x = 1, Modes
   Do y = 1, Modes
    If (x/=y .AND. E == (int(fundamental(x,1)) + int(fundamental(y,1)))) Then
        NN2(E) = NN2(E) + 1
    End If
   End Do
  End Do
 End Do
!Here the N=2 excitations are summed and binned to give the total N=2
!tier. Note the factor of 2 used to account for overcounting in the NN2(E) array.
 Do S = 0, 39
  Do E = (1 + S*bin), (S+1)*bin
      A(E) = A(E-1) + (NN(E) + (NN2(E)/2))
  End Do
  Write(7,*) A((S+1)*bin)
  Do E = 1, MaxEn
   A(E) = 0
  End Do
End Do
End Program N=2 tiered DOS
```

N=3 tier

```
Program N=3 tiered DOS
  Implicit NONE
  Integer :: E, MaxEn, x, y, z, Modes, I, J, w, v, s, bin
  Integer, Dimension (0:4000) :: NNN, NNN2, NNN3, A
  Real :: anharmonicity
  Real, Dimension (0:50,0:50) :: fundamental
 !Here the anharmonicity percentage is entered as fraction value. 5% is entered
 !here.
  anharmonicity=0.05
 !Here the number of modes are entered.
  Modes=30
!Here the maximum number of quanta to be considered in any individual mode is
!entered.
 MaxEx=20
!Here the bin size, in wavenumbers is entered. 100 cm-1 is entered here
  bin=100
!Here the maximum range of the energy E in the DOS p(E) is entered in units of
!wavenumbers. 4000 cm-1 is entered here.
  MaxEn=4000
!Here the energy of each fundamental vibrational transition is read in units of
!wavenumbers. fundamental (I,J) represents the Jth energy level of the Ith vibration.
!The ground state energy, fundamental (I,0), is defined as 0.
 Read(4,*) (fundamental(I,1), I=1,Modes)
 Do I = 1, Modes
  fundamental(I,0) = 0
 End Do
!Here the transition energy from the ground state to the Jth level in the Ith vibration
!is computed.
 Do I = 1, Modes
  Do J = 2, MaxEx
       fundamental(I,J) = fundamental(I,J-1)*(2.0-anharmonicity) &
                        -fundamental(I,J-2)*(1.0-anharmonicity)
  End Do
 End Do
!Here the states composed of an N=3 overtone are enumerated as NNN(E).
 Do E = 1, MaxEn
  Do x = 1, Modes
   If (E == int(fundamental(x,3))) Then
        NNN(E) = NNN(E) + 1
   End If
  End Do
 End Do
```

```
!Here the states composed of a combination of one N=1 fundamental and one N=2
!overtone  are enumerated as NNN12(E).
Do E = 1, MaxEn
 Do x = 1, Modes
  Do y = 1, Modes
   If (x/=y .AND. E == (int(fundamental(x,1)) + int(fundamental(y,2)))) Then
        NNN12(E) = NNN12(E) + 1
    End If
  End Do
 End Do
End Do
!Here the states composed of a combination of three N=1 fundamentals are
!enumerated as NNN3(E).
 Do E = 1, MaxEn
  Do x = 1, Modes
   Do y = 1, Modes
    Do z = 1, Modes
        If (x/=y .AND. x/=z .AND. y/=z .AND. E == (int(fundamental(x,1)) &
              + int(fundamental(y,1)) + int(fundamental(z,1)))) Then
         NNN3(E) = NNN3(E) + 1
        End If
     End Do
    End Do
   End Do
  End Do
!Here the N=3 excitations are summed and binned to give the total N=3 tier. Note
!the factor of 6 used to account for overcounting in the NNN3(E) array.
  Do S = 0, 39
   Do E = (1 + S*bin), (S+1)*bin
      A(E) = A(E-1) + (NNN(E) + NNN12(E) + (NNN3(E)/6))
   End Do
   Write(7,*) A((S+1)*bin)
   Do E = 1, MaxEn
    A(E) = 0
   End Do
  End Do
End Program N=3 tiered DOS
```

N=4 tier

```
 Program N=4 tiered DOS
  Implicit NONE
  Integer :: E, MaxEn, x, y, z, Modes, I, J, w, v, s, bin
  Integer, Dimension (0:4000) :: NNNN, NNNN22, NNNN13
  Integer, Dimension (0:4000) :: NNNN112, NNNN4, A
  Real :: anharmonicity
  Real, Dimension (0:50,0:50) :: fundamental
!Here the anharmonicity percentage is entered as fraction value. 5% is entered
!here.
  anharmonicity=0.05
!Here the number of modes are entered.
  Modes=30
!Here the maximum number of quanta to be considered in any individual mode is
!entered.
  MaxEx=20
!Here the bin size, in wavenumbers is entered. 100 cm-1 is entered here
  bin=100
!Here the maximum range of the energy E in the DOS p(E) is entered in units of
!wavenumbers. 4000 cm-1 is entered here.
  MaxEn=4000
!Here the energy of each fundamental vibrational transition is read in units of
!wavenumbers. fundamental (I,J) represents the Jth energy level of the Ith vibration.
!The ground state energy, fundamental (I,0), is defined as 0.
  Read(4,*) (fundamental(I,1), I=1,Modes)
  Do I = 1, Modes
   fundamental(I,0) = 0
  End Do
!Here the transition energy from the ground state to the Jth level in the Ith vibration
!is computed.
  Do I = 1, Modes
   Do J = 2, MaxEx
        fundamental(I,J) = fundamental(I,J-1)*(2.0-anharmonicity) &
                          -fundamental(I,J-2)*(1.0-anharmonicity)
   End Do
   End Do
!Here the states composed of an N=4 overtone are enumerated as NNNN(E).
    Do E = 1, MaxEn
     Do x = 1, Modes
      If (E == int(fundamental(x,4))) Then
          NNNN(E) = NNNN(E) + 1
      End If
     End Do
    End Do
```

```
!Here the states composed of a combination of two N=2 overtones are enumerated
!as NNNN22(E).
  Do E = 1, MaxEn
   Do x = 1, Modes
    Do y = 1, Modes
      If (x/=y .AND. E == (int(fundamental(x,2)) + int(fundamental(y,2)))) Then
          NNNN22(E) = NNNN22(E) + 1
      End If
    End Do
   End Do
  End Do
!Here the states composed of a combination of one N=1 fundamental and one N=3
!overtone are enumerated as NNNN13(E).
  Do E = 1, MaxEn
   Do x = 1, Modes
    Do y = 1, Modes
      If (x/=y .AND. E == (int(fundamental(x,1)) + int(fundamental(y,3)))) Then
          NNNN13(E) = NNNN13(E) + 1
      End If
    End Do
   End Do
  End Do
!Here the states composed of a combination of two N=1 fundamentals and one N=2
!overtone are enumerated as NNNN112(E)
  Do E = 1, MaxEn
   Do x = 1, Modes
    Do y = 1, Modes
     Do z = 1, Modes
          If (x/=y .AND. x/=z .AND. y/=z .AND. E == (int(fundamental(x,1)) &
                + int(fundamental(y,1)) + int(fundamental(z,2)))) Then
           NNNN112(E) = NNNN112(E) + 1
          End If
     End Do
    End Do
   End Do
  End Do
```

```
!Here the states composed of four N=1 fundamentals are enumerated as
!NNNN4(E).
 Do E = 1, MaxEn
  Do x = 1, Modes
   Do y = 1, Modes
    Do z = 1, Modes
     Do w = 1, Modes
         If ( x/=y .And. x/=z .And. x/=w .And. y/=z .And. y/=w .And. &
            z/=w .And. E == (int(fundamental(x,1)) + int(fundamental(y,1)) &
             + int(fundamental(z,1)) + int(fundamental(w,1)))) Then
          NNNN4(E) = NNNN4(E) + 1
         End If
     End Do
    End Do
   End Do
  End Do
 End Do
!Here the N=4 excitations are summed and binned to give the total N=4 tier. Note
!the factor of 2 used to account for overcounting in the NNNN22(E) and
!NNNN112(E) arrays and the factor of 24 in the NNNN4(E) array.
  Do S = 0, 39
   Do E = (1 + S*bin), (S+1)*bin
       A(E) = A(E-1) + NNNN(E) + (NNNN22(E)/2) + NNNN13(E) &
                  + (NNNN112(E)/2) + (NNNN4(E)/24)
   End Do
   Write(7,*) A((S+1)*bin)
   Do E = 1, MaxEn
    A(E) = 0
   End Do
  End Do
End Program N=4 tiered DOS
```